

Coherent Disaggregation and Uncertainty Quantification for Spatially Misaligned Data

Man Ho Suen¹, Mark Naylor², and Finn Lindgren³

¹*Department of Epidemiology & Biostatistics, School of Public Health, Imperial College London, London, UK*

²*School of GeoSciences, University of Edinburgh, Edinburgh, UK*

³*School of Mathematics and Maxwell Institute for Mathematical Sciences, University of Edinburgh, Edinburgh, UK*

¹*email address: m.suen19@imperial.ac.uk*

Abstract

Spatial misalignment arises when datasets are aggregated or collected at different spatial scales, leading to information loss. We develop a Bayesian disaggregation framework that links misaligned data to a continuous-domain model through an iteratively linearised integration scheme implemented with the Integrated Nested Laplace Approximation (INLA). The framework accommodates different ways of handling observations depending on the application, resulting in four variants: (i) *Raster at Full Resolution*, (ii) *Raster Aggregation*, (iii) *Polygon Aggregation* (PolyAgg), and (iv) *Point Values* (PointVal). The first three represent increasing levels of spatial averaging, while the last two address situations with incomplete covariate information. For PolyAgg and PointVal, we reconstruct the covariate field using three strategies — *Value Plugin*, *Joint Uncertainty*, and *Uncertainty Plugin* — with the latter two propagating uncertainty.

We illustrate the framework with an example motivated by landslide modelling, focusing on methodology rather than interpreting landslide processes. Simulations show that uncertainty-propagating approaches outperform *Value Plugin* method and remain robust under model misspecification. Point-pattern observations and full-resolution covariates are therefore preferable, and when covariate fields are incomplete, uncertainty-aware methods are most reliable. The

framework is well suited to landslide susceptibility modelling and other spatial mapping tasks, and integrates seamlessly with INLA-based tools.

Keywords: integrated nested Laplace approximation, inlabru, landslides, spatial misalignment, approximate Bayesian computation, uncertainty quantification

1 Introduction

Information may exist everywhere, but data are rarely available at all locations in space and time. Depending on collection methods, data are measured at individual point locations and various spatial scales, such as partitioning the domain of interest. This leads to spatial misalignment, and when inference is needed at a different scale, it results in a change-of-support problem (COSP; Gelfand et al. (2001)). Traditionally, misaligned data are aligned to a chosen spatial partition, with each element termed a “block”, which often requires aggregation or disaggregation, and modelled using block-kriging (Gotway and Young, 2002).

Early work includes Fuentes and Raftery (2005), who proposed a Bayesian hierarchical framework for fusing areal and point-referenced data, extended by Berrocal et al. (2010) through hierarchical downscaling for multi-resolution data, and by Wilkie et al. (2019) to spatio-temporal supports using nonparametric methods. However, these approaches requires spatially varying coefficients, resulting in high computational burden due to the large number of hyperparameters estimated via Markov Chain Monte Carlo. Recent applications across diverse domains increasingly rely on approximate Bayesian inference through Integrated Nested Laplace Approximation (INLA) (Rue et al., 2009), implemented in packages such as `R-INLA` and `inlabru` (Lindgren et al., 2024), for continuous-domain models (Moraga et al., 2017; Cameletti et al., 2019; Forlani et al., 2020; Villejo et al., 2023; Zhong and Moraga, 2024). These models yield a continuous intensity field, which characterises the spatial (or spatio-temporal) variation in the expected density of events across a domain.

When it comes to spatial point process and continuous domain model, inference at block resolution require averaging misaligned data within each block which leads to the issues of aggregation

and specification biases raised by Konrad and Morgenstern (1982). The main problem with these methods is that averaging over blocks results in loss of point-level information, making the underlying signal less accessible. Moreover, both modelling and inference are constrained by the chosen block structure, often defined by grid cells, which limits flexibility. At fine resolutions, spatial misalignment can render computations intractable and obscure the interpretation of results. Additionally, these methods are not easily transferable to unseen study regions.

A key motivation for this study is its relevance to landslide susceptibility modelling, where landslide polygons are often reduced to centroids and both point locations and covariates are subsequently aggregated into areal counts and averages (Lombardo et al., 2018, 2019; Loche et al., 2022; Opitz et al., 2022). A major challenge in this setting is the spatial misalignment between point-pattern observations and covariates measured at varying spatial resolutions. A common strategy is to aggregate landslide centroids into counts within predefined blocks, such as “slope units” (Alvioli et al., 2016, 2020), which are a series of finite width polygons bounded by topographic ridges at the top and rivers at the bottom such that they define regions within which landslides are typically geometrically constrained. This type of model could, for example, consider the counts and sizes of landslides aggregated within each slope unit. However, this aggregation inherits the limitations noted above: specification bias arises because aggregated count models rely on proxy covariates confounded with slope units, while aggregation bias arises from discarding landslide location information, adding uncertainty. Retaining point locations is fundamental in point pattern analysis. Although landslides are not inherently point events and their manually registered locations carry potential errors, avoiding aggregation prevents further uncertainty when constructing continuous susceptibility maps. Moreover, aggregation renders uncertainty propagation intractable, as exact event locations are lost within counts, and individual event uncertainties and covariate resolution effects are blended into summary statistics, e.g. means or medians.

In practice, only a limited subset of the covariate field is often observed, requiring either joint reconstruction with the intensity field (one-stage) or sequential estimation (two-stage). The one-stage approach is less common in the literature due to the undesirable feedback in joint estimation

for spatial models. Examples include autoregressive disturbances with spatial autoregressive models (Kelejian and Prucha, 1998), spatial disaggregation with environmental feedback on land-use transport models (Spiekermann and Wegener, 2008), and two-stage approach on incorporating spatial lag autocorrelation (Lambert et al., 2010). However, it remains unclear in what situation and how the one-stage and two-stage approach would affect the model performance in the more flexible INLA-SPDE setting since the neighbouring structure is much finer in scale that depends on the mesh (Rue et al., 2018).

In this paper, we address how to (i) strike a balance between computation and model accuracy in aligning the point patterns with areal data, i.e. data misalignment, via linearisation; (ii) model aggregated count and covariate data, incomplete covariate fields (e.g. missing data and downscaling) and incorporate the uncertainty of these fields into the model; and, (iii) handle model misspecification for nonlinear transformations of incomplete covariate fields.

2 Definition of Poisson Point and Count Processes

In this paper, we consider unmarked point process and a bounded domain $\Omega \subset \mathbb{R}^d$, $d \in \mathbb{N}$. However, our framework for aggregated data is extendable to marked point process, as well as space and time $\Omega \times T$ settings.

Definition 2.1 (Poisson Point Process). *Let $Y \subset \Omega$ be a countable random subset of points. We define a Poisson point process for Y with an intensity function $\lambda : \Omega \rightarrow [0, \infty)$ via the counts of points for every Borel measurable set $A \subseteq \Omega$, $N_Y(A) = \text{card}(Y \cap A)$, where $\text{card}(\cdot)$ denotes the cardinality of a set. The counts are Poisson distributed with mean $\Lambda(A)$, which is assumed to be non-negative and finite,*

$$N_Y(A) \sim \text{Pois}[\Lambda(A)], \text{ and } \Lambda(A) = \int_{s \in A} \lambda(s) ds, \quad (1)$$

where $\lambda(\cdot)$ is the intensity function.

If the log intensity function of a spatial point process is a Gaussian random field, this point process is called log-Gaussian Cox process (LGCP) (Møller et al., 1998; Diggle, 2013). In the case of aggregated count observations, we extend the Poisson point process to a Poisson count process.

Definition 2.2 (Poisson Count Process). *Let $\{A_p\}_{p=1}^{n_A}$ be disjoint and bounded aggregation sets (regions/volumes) and N_p be the count of points in $A_p \subset \Omega$,*

$$N_p := N_Y(A_p) \sim \text{Pois} \left(\int_{A_p} \lambda(\mathbf{s}) d\mathbf{s} \right). \quad (2)$$

We define a Poisson count process $\mathcal{N} := \{N_p\}$ with intensity function $\lambda : \Omega \rightarrow [0, \infty)$.

Suppose that we have a point pattern observation $\mathcal{Y} = \{y_1, \dots, y_N\}$, where N is a random variable, the density of \mathcal{Y} for $N = n$ given the intensity function λ is (see Appendix A.1 for derivation),

$$p_Y(\mathcal{Y}, N = n | \lambda) = \frac{e^{-\Lambda(\Omega)}}{n!} \prod_{i=1}^n \lambda(y_i).$$

Definition 2.3 (Log-likelihood of Poisson Point Process). *The likelihood can be defined as a ratio with respect to a homogeneous Poisson point process, i.e. $\lambda \equiv 1$,*

$$\mathcal{L}(\lambda | \mathcal{Y}) := \frac{p_Y(\mathcal{Y}, N = n | \lambda)}{p_Y(\mathcal{Y}, N = n | \lambda \equiv 1)} = e^{|\Omega| - \Lambda(\Omega)} \prod_{i=1}^n \lambda(y_i). \quad (3)$$

The log-likelihood of a Poisson Point Process is

$$\ell(\lambda | \mathcal{Y}) = \log \mathcal{L}(\lambda | \mathcal{Y}) = \underbrace{|\Omega|}_{\text{domain volume}} - \underbrace{\int_{\Omega} \lambda(\mathbf{s}) d\mathbf{s}}_{\text{domain contribution}} + \underbrace{\sum_{i=1}^n \log \lambda(y_i)}_{\text{observed point contribution}}. \quad (4)$$

Definition 2.4 (Log-likelihood of Poisson Count Process). *We define the log-likelihood of a Pois-*

son count process (See Appendix A.1 for derivation)

$$\ell(\lambda|\mathcal{Y}, \{A_p\}) = \underbrace{|\Omega|}_{\text{domain volume}} - \underbrace{\int_{\Omega} \lambda(\mathbf{s}) d\mathbf{s}}_{\text{domain contribution}} + \underbrace{\sum_{p=1}^{n_A} \log \lambda(A_p)}_{\text{observed count contribution}} . \quad (5)$$

It is straightforward to compute the observed contribution once we define a log-intensity function as a linear model and extendable to a monotonic increasing nonlinear model. The domain contribution is analytically intractable and would be ideally approximated in a computationally efficient manner (Simpson et al., 2016). Having a triangulation over the domain, we can approximate the spatial random effect in a latent field $\mathbf{s} \in \mathbb{R}^d$ with K vertices via a basis expansion,

$$u(\mathbf{s}) = \sum_{k=1}^K \psi_k(\mathbf{s}) u_k, \text{ and } \mathbf{u} = (u_1, \dots, u_k) \sim \mathbf{N}(\mathbf{0}, \mathbf{Q}^{-1}), \quad (6)$$

where $\{\psi_k\}$ is a set of piecewise linear basis function and \mathbf{u} are Gaussian distributed weights with a sparse covariance matrix \mathbf{Q}^{-1} . For illustration, we define the linear predictor in a purely spatial setting that is extendable to space-time setting,

$$\log \lambda(\mathbf{s}) \approx \eta(\mathbf{s}) := \mathbf{1}\beta_0 + \beta_x x(\mathbf{s}) + u(\mathbf{s}), \text{ and} \quad (7)$$

$$[\log \lambda(s_i) \approx \eta(s_i), i = 1, \dots, n]^T := \mathbf{A}\mathbf{v}, \quad (8)$$

where β_0 is an intercept, β_x is the coefficient of the linear fixed effect covariate, $x(\mathbf{s})$ is the covariate field; \mathbf{A} is a projector matrix, and $\mathbf{v} = [\beta_0, \beta_x, \mathbf{u}^T]^T$. The product $\mathbf{A}\mathbf{v}$ represents the evaluation of the field defined by the mesh at any given finite set of locations. Given the data, the model can be fitted via the Integrated nested Laplace approximations (INLA) (Rue et al., 2018). Here the predictor $\eta(\mathbf{s})$ approximates $\log \lambda(\mathbf{s})$ and this will be explained in Section 3.3.

For theory, $u(\cdot)$ is defined as a stationary Gaussian Random Field (GRF) with zero mean and

Matérn covariance function or kernel,

$$\varrho(\mathbf{s}, \mathbf{s}') = \frac{\sigma^2}{\Gamma(\nu)2^{\nu-1}} (\kappa \|\mathbf{s} - \mathbf{s}'\|)^\nu K_\nu(\kappa \|\mathbf{s} - \mathbf{s}'\|), \quad (9)$$

where $\sigma^2 > 0$ is the marginal variance, $\nu > 0$ is the smoothness parameter, $\kappa > 0$ is the range parameter and K_ν is the modified Bessel function of second kind. We evaluate the field $u(\cdot)$ via mapping to the stochastic partial differential equation (SPDE) (Whittle, 1954, 1963; Lindgren et al., 2011). We follow the re-parametrisation of the Penalised Complexity (PC) prior in Fuglstad et al. (2015) by setting $\nu = \alpha - \frac{d}{2} > 0$ and $\kappa = \frac{\sqrt{8\nu}}{\rho}$, with ρ as the spatial range, i.e.

$$(\kappa^2 - \Delta)^{\frac{\alpha}{2}} [\sqrt{\tau}u(\mathbf{s})] = \mathcal{W}(\mathbf{s}), \quad (10)$$

where $\Delta = \sum_{i=1}^d \partial^2 / \partial s_i^2$ is the Laplacian operator, $\tau = \Gamma(\nu) \left[(4\pi)^{\frac{d}{2}} \Gamma(\nu + \frac{d}{2}) \sigma^2 \kappa^{2\nu} \right]^{-1} > 0$ is the scaling parameter of $u(\cdot)$ with d denoting the dimension of the space and $\mathcal{W}(\mathbf{s})$ as spatial white noise. In this formulation, the covariance function in equation (9) can be rewritten as

$$\varrho(d_s := \|\mathbf{s} - \mathbf{s}'\|) = \frac{\sigma^2}{\Gamma(\nu)2^{\nu-1}} \left(\frac{\sqrt{8\nu}d_s}{\rho} \right)^\nu K_\nu \left(\frac{\sqrt{8\nu}d_s}{\rho} \right). \quad (11)$$

3 Computation

We construct a Taylor approximation of the intensity contribution, to address spatial misalignment through disaggregation (Section 3.1), then consider disaggregation from a domain partitioning perspective (Section 3.2), and finally assess the effects of linearisation (Section 3.3).

3.1 Taylor Approximation for Intensity Contribution

We partition the sample space Ω (Section 2) into disjoint subsets Ω_j , such that $\Omega_j \cap \Omega_{j'} = \emptyset$ for $j \neq j'$, $\Omega = \bigcup_{j=1}^J \Omega_j$, with further specifications discussed in Section 3.2. We consider aggregated count data over regions defined by sets A_p in equation (2), for each Ω_j , $\Omega_j \subseteq A_p$. Let

$M_j(\mathbf{u}) = \log \left\{ \int_{\Omega_j} \exp[\eta(\mathbf{s})] d\mathbf{s} \right\}$ in the j -th subset, we approximate the logarithmic integral of the intensity function for each subset Ω_j with the first-order Taylor series,

$$M_j(\mathbf{u}) \approx M_j(\mathbf{u}_*) + \mathbf{J}^{(j)}(\mathbf{u}_*)^\top (\mathbf{u} - \mathbf{u}_*) := \overline{M}_j(\mathbf{u}), \quad (12)$$

where \mathbf{u}_* are the linearisation points of the Taylor approximation, and $\mathbf{J}^{(j)}(\cdot)$ is the Jacobian matrix, i.e. first-order derivative matrix for M_j with respect to \mathbf{u} . Although we ignore the remaining higher-order terms here, we can assess the approximation by checking the leading error term.

Given a stable integration scheme (see Appendix B.9), we discretise the integrals for each Ω_j with weights $w_{jk} > 0$ at the k -th knot. Similarly, let $m_j(\mathbf{u}) = \log \left\{ \sum_{k=1}^{n_j} w_{jk} \exp[\eta(\mathbf{s}_{jk})] \right\}$, with the first-order Taylor series,

$$m_j(\mathbf{u}) \approx m_j(\mathbf{u}_*) + \mathbf{J}^{(j)}(\mathbf{u}_*)^\top (\mathbf{u} - \mathbf{u}_*) =: \overline{m}_j(\mathbf{u}). \quad (13)$$

Derivations of $\overline{M}_j(\mathbf{u})$ and $\overline{m}_j(\mathbf{u})$ in equations (12) and (13) can be found in Appendix B.1.

Theorem 3.1 (Taylor approximation for the continuous and discretised linearisation). *Assume both $M_j(\mathbf{u})$ and $m_j(\mathbf{u})$ are twice differentiable at some points $\mathbf{u}_* \in \mathbb{R}$; and the linear predictor $\eta(\cdot)$ is an affine function of \mathbf{u} . For the continuous linearisation, we have*

$$M_j(\mathbf{u}) - \overline{M}_j(\mathbf{u}) = \frac{1}{2}(\mathbf{u} - \mathbf{u}_*)^\top \mathbf{H}_M^{(j)}(\mathbf{u} - \mathbf{u}_*) + \mathcal{O}(\|\mathbf{u} - \mathbf{u}_*\|^3), \quad (14)$$

where $\mathbf{H}_M^{(j)}$ is the Hessian of $M_j(\mathbf{u})$ and $\mathcal{O}(\cdot)$ is the higher-order terms with respect to (\cdot) . For the discretised linearisation, we have

$$m_j(\mathbf{u}) - \overline{m}_j(\mathbf{u}) = \frac{1}{2}(\mathbf{u} - \mathbf{u}_*)^\top \mathbf{H}^{(j)}(\mathbf{u} - \mathbf{u}_*) + \mathcal{O}(\|\mathbf{u} - \mathbf{u}_*\|^3), \quad (15)$$

where $\mathbf{H}^{(j)}$ is the Hessian of $m_j(\mathbf{u})$. Derivations for (14) and (15) can be found in Appendices B.2 and B.3.

Hence, the domain contribution can be approximated as

$$-\int_{\Omega} \lambda(\mathbf{s}) d\mathbf{s} \approx \begin{cases} -\sum_{j=1}^J \exp [\overline{M}_j(\mathbf{u})] \\ -\sum_{j=1}^J \exp [\overline{m}_j(\mathbf{u})]. \end{cases} \quad (16)$$

We will compare the accuracy between $\overline{M}_j(\cdot)$ and $\overline{m}_j(\cdot)$ approximations in equation (16) in Section 3.3. See Appendix B.4 for the implementation of the logarithmic sum, i.e. $\overline{m}_j(\cdot)$ approximation.

3.1.1 Taylor Approximation for Discretised Linearisation

In the `inlabru` package, the linearisation approach in equation (16) requires a sequence of runs of the INLA method, each followed by a line search to locate the optimal linearisation point. If the approximation of the domain contribution is not large enough to counter the observed point contributions in equation (4), the approximation of the likelihood can go to infinity and cause numerical instability (see Appendix B.10). To avoid the observed contribution overpowering the likelihood, we need to bound the domain contribution. Hence, Theorem 3.1 shows that the Jacobian $\mathbf{J}^{(j)}$ and Hessian $\mathbf{H}^{(j)}$ terms of $m_j(\mathbf{u})$ converge in equation (15). The line search continues until the given tolerance is met and refer to Lindgren et al. (2024) with regard to setting the initial linearisation point and the stopping rule to optimise the fit.

3.2 Domain Partition

The subsets $\{\Omega_j\}$ from Section 3.1 define the resolution of the intensity field in the outcome prediction. Their volumes have to be smaller than the corresponding $|A_p|$ (see Definition 2.2). There is no benefit in using subsets smaller than the finest data resolution. Here, we define the subsets using the user-specified mesh, which serves as a computational tool for solving the SPDE in equation (10) via the Finite Element Method (FEM) (Lindgren et al., 2011, 2022). The Matérn field term $u(\mathbf{s})$ in equation (7) has to be bounded by the covariate field in the resolution scale since

there may be no observation in the mesh element and the Gaussian prior is not informative enough without any data input. Essentially, the degrees of freedom in the field should be respected (see Section 7.1). Nonetheless, users may downscale the resolution of the covariate data and refine the mesh size accordingly. Under these constraints, the flexibility to define the subsets then takes into account the observed point locations, the data quality, the integration scheme and the computation costs.

3.2.1 Shape of Mesh Elements

In light of the tessellation of mesh elements over the domain, we want the subsets to be regularly shaped, i.e. triangles, squares and hexagons. We do not consider mesh-free methods which treat the data points as nodes. Mesh-free methods can handle particle-like finite element analysis, which can be useful for animal tracking since animals interact with one another (Liu, 2009). However, due to these interactions and dynamical nodes, more computation time is required. Additionally, further handling is needed for a stable integration scheme with the current construction of the likelihood. Mixed-shaped meshes are not considered because their construction can be too flexible and thus more complicated to implement.

Discretisation and orientation effects are undesirable. In this regard, circles do not suffer from orientation bias. However, circles do not tessellate. Hexagon meshes suffer less from orientation effects since they are almost circular, and each hexagon has six neighbours and smooths out the discrepancy between nearby hexagons. In general, hexagonal meshes fit curved boundary domains well, and have good accuracy and solving time. We take advantage of this by constructing equilateral triangles joining the centres of neighbouring hexagons. These are then joined with irregular triangular elements between the hexagon centres and the domain boundary. To avoid spatial misalignment with raster data, square elements can alternatively be used to match the raster grid (e.g. satellite imagery) and can be constructed from triangular mesh elements.

3.2.2 Data resolution and mesh element size

To define the mesh element size, we take the data resolution and spatial correlation length as baselines. In order to accurately represent the correlation structure, the mesh elements have diameter smaller than the correlation length. As an anecdotal rule of thumb, diameters a factor 5–10 smaller than the correlation length gives highly accurate approximations, but in practice, larger elements can be sufficient. Given that constraint, further refining the elements finer than the data does not improve the accuracy of point estimates, but can improve posterior uncertainty estimates on fine scales. Choosing the mesh resolution is a compromise between computation time and approximation error. Finer elements may increase accuracy but also computational cost and time. In real applications, we do not know the exact spatial range and anisotropy of the data a priori, and we often only observe a limited set of data. Hence, we may not know the optimal balance between mesh resolution and computation time. In addition, any adjustments on maximum element edge in the meshing construction criteria changes the structure of the mesh. Since there are multiple factors, we do not know exactly how the mesh refinements affect accuracy. As a general rule, we need to make sure that the resolution of the mesh is sufficiently fine within the domain of interest to represent the between-observation location variability.

We can consider uniform and non-uniform meshes. A uniform mesh places uniformly sized elements across and is easy to implement. However, in order to avoid boundary effects from the SPDE construction (Lindgren et al., 2011), we need to extend the mesh beyond the domain of interest. A uniform extension is computationally wasteful, so it is normally preferable to use an extension with non-uniform elements of increasing size. This minimises the computational cost, while keeping a high accuracy inside the domain of interest. A non-uniform mesh, i.e. with varying element shapes and sizes, can also be used to adapt the mesh resolution to geographical features of the desired domain space. In landslides, we mostly care about regions with human activities. For instance, we would like to know the landslides susceptibility for planning road construction. Adaptivity can be achieved through mesh refinement (Rue et al., 2018), with the target mesh quality varying across space. In some cases, we have higher resolution data i.e. less uncertainty and

more information, at observation sites, such as hospital data in urban areas compared to rural areas, and animal tracking in ecology. To reflect this need, we can place finer elements at these locations without creating nonconforming meshes during refinement. As discussed by Lindgren et al. (2011), the mesh quality controls how closely the discretised spatial field representation lies to the continuous domain model, which can in principle be used to give error bounds. There is further discussion on computing on fine lattices in Sections 2 and 7.3 of Simpson et al. (2016), as well as a detailed error analysis. As seen in Table 1, the computational mesh resolution is here chosen to be coarser than the finest covariate raster resolution, but finer than the aggregate data resolution.

For integration, the k -th knot and weight (w_{jk} from Section 3.1) in the j -th subset is defined through an integration scheme that is aligned with the mesh triangle, but can have a denser resolution than the mesh itself. As the total number of knots goes to infinity, the accuracy eventually does not continue to improve given the data and modelling mesh resolutions. Hence, we choose the integration scheme resolution so that the likelihood approximation is stable, accurate and computationally efficient.

3.3 Assessment of Effects of Linearisation

If η is a nonlinear expression, i.e. non-linear predictor, say $f(x) = x^{-2}$, there would be further expansion of \mathbf{A} from $\mathbf{b} + \mathbf{A}\mathbf{u}$ which can be grouped into higher-order terms of $\|\mathbf{u} - \mathbf{u}_*\|$ after differentiation (see Appendix B.5). Hence, the first-order Taylor expansion remains adequate.

Before we proceed to the assessment of nonlinearity, we take a detour to introduce the structure of hierarchical models in INLA. We denote \mathbf{y} as the realisations of \mathcal{Y} which are conditionally independent given η and θ in the INLA setting. The INLA implementation requires incorporating the covariance parameters θ into equation (6) such that $\theta \sim p(\theta)$; $\mathbf{u}|\theta \sim N(\mu_u, \mathbf{Q}_\theta^{-1})$, and $\mathbf{y}|\mathbf{u}, \theta \sim p(\mathbf{y}|\eta(\mathbf{u}), \theta)$.

We aim to assess how well the linearisation of the predictor works. To this end, we expand the second-order Taylor polynomial terms and compute the bias. We define $\log \tilde{\mathbb{P}}(\mathbf{u}|\mathbf{y}, \theta)$ as the

log-density of the true model expressed in the second-order Taylor expansion and higher-order terms $\mathcal{O}(\|\mathbf{u} - \mathbf{u}_*\|^3)$, and $\log \bar{\mathbb{P}}(\mathbf{u}|\mathbf{y}, \boldsymbol{\theta})$ as the log-density of the linearised model yielded from our proposed method. We assess the Kullback-Leibler (KL) divergence between the $\tilde{\mathbb{P}}(\mathbf{u}|\mathbf{y}, \boldsymbol{\theta})$ and $\bar{\mathbb{P}}(\mathbf{u}|\mathbf{y}, \boldsymbol{\theta})$. Indeed, the KL divergence serves as posterior non-linearity evaluation since it is not easy to come up with a distance metric. With Bayes' theorem, we have $\mathbb{P}(\mathbf{u}|\mathbf{y}, \boldsymbol{\theta}) = \frac{\mathbb{P}(\mathbf{u}, \mathbf{y}|\boldsymbol{\theta})}{\mathbb{P}(\mathbf{y}|\boldsymbol{\theta})} = \frac{\mathbb{P}(\mathbf{y}|\mathbf{u}, \boldsymbol{\theta})\mathbb{P}(\mathbf{u}|\boldsymbol{\theta})}{\mathbb{P}(\mathbf{y}|\boldsymbol{\theta})}$. Since $(\mathbf{u}|\boldsymbol{\theta})$ is Gaussian and $\mathbb{P}(\mathbf{y}|\boldsymbol{\theta})$ is the normalising factor, we focus on the likelihood factor $\log \mathbb{P}(\mathbf{y}|\mathbf{u}, \boldsymbol{\theta})$.

Theorem 3.2 (Expectation on the difference of the linearisation on the observation log-density).

Using the notations from Theorem 3.1,

$$\log \frac{\tilde{\mathbb{P}}(\mathbf{y}|\mathbf{u}, \boldsymbol{\theta})}{\bar{\mathbb{P}}(\mathbf{y}|\mathbf{u}, \boldsymbol{\theta})} = - \sum_j e^{\bar{m}_j(\mathbf{u}_*)} \left[\frac{1}{2} (\mathbf{u} - \mathbf{u}_*)^\top \mathbf{H}^{(j)} (\mathbf{u} - \mathbf{u}_*) + \mathcal{O}(\|\mathbf{u} - \mathbf{u}_*\|^3) \right]. \quad (17)$$

The derivation of equation (17) can be found in Appendix B.6. Then taking expectation, we have

$$\begin{aligned} \mathbb{E}_{\mathbf{u} \sim \mathcal{N}(\boldsymbol{\mu}_\theta, \mathbf{Q}_\theta^{-1})} \left(\log \frac{\tilde{\mathbb{P}}(\mathbf{y}|\mathbf{u}, \boldsymbol{\theta})}{\bar{\mathbb{P}}(\mathbf{y}|\mathbf{u}, \boldsymbol{\theta})} \right) &= -\frac{1}{2} \sum_j e^{\bar{m}_j(\mathbf{u}_*)} \left[\text{tr}(\mathbf{H}^{(j)} \mathbf{Q}_\theta^{-1}) + (\boldsymbol{\mu}_\theta - \mathbf{u}_*)^\top \mathbf{H}^{(j)} (\boldsymbol{\mu}_\theta - \mathbf{u}_*) \right] \\ &+ \mathcal{O} \left[\mathbb{E}(\|\mathbf{u} - \mathbf{u}_*\|^3) \right]. \end{aligned} \quad (18)$$

The derivation of equation (18) can be found in Appendix B.7.

The expectation in equation (18) depends on the $\mathbf{H}^{(j)}$ yielded from the true likelihood, which in turns relates to both the estimated intensity function $\hat{\lambda}$, and the partial derivative of the nonlinear predictor with respect to the linearisation point \mathbf{u}_* . Both $\hat{\lambda}$ and \mathbf{u}_* can be evaluated in INLA. In other words, $\mathbf{H}^{(j)}$ depends on the nonlinearity in the predictor in l and l' dimensions. When \mathbf{H} is large, the nonlinear terms deviate more from the estimated mode computed from INLA. We can view $\mathbf{H}^{(j)} \mathbf{Q}_\theta^{-1}$ in equation (18) as a correction term, which is composed of the Hessian term and the covariance structure of the Gaussian components \mathbf{u} . In the case of $\boldsymbol{\mu}_\theta - \mathbf{u}_* = 0$, it serves as a sanity check as this would minimise the second term.

Now we have all the ingredients to compute the KL divergence. Since the KL divergence is

asymmetric, we will compute both $\text{KL} \left[\tilde{\mathbb{P}}(\mathbf{u}|\mathbf{y}, \boldsymbol{\theta}) \parallel \bar{\mathbb{P}}(\mathbf{u}|\mathbf{y}, \boldsymbol{\theta}) \right]$ and $\text{KL} \left[\bar{\mathbb{P}}(\mathbf{u}|\mathbf{y}, \boldsymbol{\theta}) \parallel \tilde{\mathbb{P}}(\mathbf{u}|\mathbf{y}, \boldsymbol{\theta}) \right]$. We follow the proof from Lindgren et al. (2024).

Theorem 3.3 (Kullback-Leibler (KL) divergence for the first and second Taylor expansion). *Denote $\mathbf{G} = -\sum_j e^{\bar{m}_j} \mathbf{H}^{(j)}$ and the linearised and approximate nonlinearised posterior distribution as $N(\bar{\boldsymbol{\mu}}_\theta, \bar{\mathbf{Q}}_\theta)$ and $N(\tilde{\boldsymbol{\mu}}_\theta, \tilde{\mathbf{Q}}_\theta)$ respectively, we have*

$$\begin{aligned} \text{KL} \left[\tilde{\mathbb{P}}(\mathbf{u}|\mathbf{y}, \boldsymbol{\theta}) \parallel \bar{\mathbb{P}}(\mathbf{u}|\mathbf{y}, \boldsymbol{\theta}) \right] &= \frac{1}{2} \{ \log \det(\bar{\mathbf{Q}}_\theta - \mathbf{G}) - \log \det(\bar{\mathbf{Q}}_\theta) + \text{tr} [\bar{\mathbf{Q}}_\theta(\bar{\mathbf{Q}}_\theta - \mathbf{G})^{-1}] \\ &\quad - d + (\bar{\boldsymbol{\mu}}_\theta - \tilde{\boldsymbol{\mu}}_\theta)^\top \bar{\mathbf{Q}}_\theta(\bar{\boldsymbol{\mu}}_\theta - \tilde{\boldsymbol{\mu}}_\theta) \} + \mathcal{O} [\mathbb{E}(\|\mathbf{u} - \mathbf{u}_*\|^3)], \text{ and} \end{aligned} \quad (19)$$

$$\begin{aligned} \text{KL} \left[\bar{\mathbb{P}}(\mathbf{u}|\mathbf{y}, \boldsymbol{\theta}) \parallel \tilde{\mathbb{P}}(\mathbf{u}|\mathbf{y}, \boldsymbol{\theta}) \right] &= \frac{1}{2} \{ \log \det(\bar{\mathbf{Q}}_\theta) - \log \det(\bar{\mathbf{Q}}_\theta - \mathbf{G}) + \text{tr} [(\bar{\mathbf{Q}}_\theta - \mathbf{G})\bar{\mathbf{Q}}_\theta^{-1}] \\ &\quad - d + (\bar{\boldsymbol{\mu}}_\theta - \tilde{\boldsymbol{\mu}}_\theta)^\top (\bar{\mathbf{Q}}_\theta - \mathbf{G})(\bar{\boldsymbol{\mu}}_\theta - \tilde{\boldsymbol{\mu}}_\theta) \} + \mathcal{O} [\mathbb{E}(\|\mathbf{u} - \mathbf{u}_*\|^3)], \end{aligned} \quad (20)$$

where d is the dimension of the vector \mathbf{u} . The derivation can be found in Appendix B.8.

We can see the KL divergences have similar structure as in equation (18). We wish to minimise the difference between the linearised and nonlinearised means $(\bar{\boldsymbol{\mu}}_\theta - \tilde{\boldsymbol{\mu}}_\theta)$, which minimises the both divergences. The term $(\bar{\mathbf{Q}}_\theta - \mathbf{G})$ is the sum of the linearised precision matrix and the Hessian term, and can therefore be viewed as an approximation of $\tilde{\mathbf{Q}}_\theta$.

Indeed, these divergences provide insights for the bias. Once we can compute them in the `inlabru` package, we consider different integration schemes based on different mesh construction for the intensity field λ . Although we do not have control over the precision matrix of the Gaussian components \mathbf{u} , a more linear predictor would imply a smaller $\|\mathbf{G}\|$. The implications of nonlinearity is two-fold. Nonlinearity can be induced by the aggregation and/or in the predictor expression. The former can be alleviated by the mesh construction with respect to the aggregation structure. For the latter, mesh resolution can be increased adaptively in regions where the predictor exhibits greater nonlinearity. Despite the greater number of elements, we aim to minimise $\|\mathbf{G}\|$ using smaller $\mathbf{H}^{(j)}$, with respect to the effect of the aggregation.

4 Model and Method

We introduce the models in a general setting, illustrate them in the simulation study (Section 5), and assess their performance (Section 6). The true underlying model follows the linear predictor in equation (7), with observations as either point patterns \mathcal{Y} or aggregated counts \mathcal{N} over domain partitions defined in Definitions 2.1 and 2.2, respectively.

4.1 Models with covariate Observation Plugin (OP)

We formulate the models using Observation Plugin (OP) with the linear predictor

$$\eta(\mathbf{s}) = \beta_0 + \beta_x z(\mathbf{s}) + u(\mathbf{s}), \quad (21)$$

where $z(\mathbf{s})$ is the observed covariate at location \mathbf{s} , and $u(\mathbf{s})$ is defined in equation (6) with a mesh. The resolution of $z(\mathbf{s})$ depends on data availability; for example, it may be an aggregated raster covariate field (RastAgg) or an aggregated field over polygons (PolyAgg), both forming partitions of the domain.

4.2 Covariate Field Estimation from Incompletely Observed Data

When $z(\mathbf{s})$ in equation (21) is an aggregated covariate field over a partition of the domain, it is only partially observed. Beyond OP, the continuous covariate field can be estimated and incorporated into the linear predictor $\eta(\cdot)$ via Joint Uncertainty (JU), i.e. a one-stage approach (Section 4.3), or via two-stage approaches: Value Plugin (VP) and Uncertainty Plugin (UP) (Section 4.4). Specifically, we assume the continuous covariate field $x(\cdot)$ is aggregated in an unbiased manner such that the observed averages z_p over the aggregation sets A_p (see Definition 2.2),

$$z_p = \frac{1}{|A_p|} \int_{A_p} x(\mathbf{s}) + \epsilon(\mathbf{s}) d\mathbf{s} = \frac{1}{|A_p|} \int_{A_p} x(\mathbf{s}) d\mathbf{s} + \underbrace{\frac{1}{|A_p|} \int_{A_p} \epsilon(\mathbf{s}) d\mathbf{s}}_{=:\epsilon_p}, \quad (22)$$

where $\epsilon(\cdot)$ is a Gaussian field such that ϵ_p are independent $\mathbf{N}(0, \sigma_{z_p|x(\cdot)}^2)$ distributions. For simplicity, we assume all $\sigma_{z_p|x(\cdot)}^2$ share a common value σ_z^2 , though this can be extended to allow variances scaled by functions of $|A_p|$. We treat the covariate field $x(\cdot)$ as a random variable $X(\cdot)$, modelled with the prior $X(\cdot) \sim \text{GRF}(\mu_x(\cdot), \varrho_x(\cdot, \cdot))$, yielding the posterior $X(\cdot)|\{z_p\} \sim \text{GRF}(\mu_{x|\{z_p\}}(\cdot), \varrho_{x|\{z_p\}}(\cdot, \cdot))$. We use the posterior mean $\hat{x} = \mu_{x|\{z_p\}}$ as the continuous estimate of the field.

When $z(s)$ in equation (21) are Point Values (PointVal) scattered across the domain (e.g. station data), $\{z(s_i)\}_{i=1}^{n_z}$, the estimation is the same as that for aggregated covariate field, except replacing $\{z_p\}$ with $\{z(s_i)\}$.

4.3 Joint Uncertainty (JU) Method

The Joint Uncertainty (JU) approach models the covariate field and parameters simultaneously,

$$\begin{cases} z(\cdot) &= \hat{x}(\cdot) + \epsilon(\cdot), \quad \epsilon \sim \mathbf{N}(\mathbf{0}, \mathbf{Q}_\epsilon^{-1}), \\ \eta(\cdot) &= \beta_0 + \tilde{\beta}_x \hat{x}(\cdot) + u(\cdot), \quad \tilde{\beta}_x \sim \text{Exp}(\cdot), \end{cases} \quad (23)$$

where ϵ uses the same construction of \mathbf{u} in equation (6). This may bring identifiability or multimodal concerns between $\hat{x}(\cdot)$ and $u(\cdot)$. Another concern is convergence, which largely depends on whether the coefficient of $\hat{x}(\cdot)$ can attain an opposite sign, resulting in a bimodal distribution. Nonetheless, as soon as it picks a "side" for β_x , the linearisation makes it unimodal. But different INLA runs, or with different initial values, might pick the opposite sign. However, with some direct observations of the field $x(\cdot)$ (i.e. $\{z_p\}$ or $\{z(s_i)\}$), it is unlikely to happen. In practice, we often have prior information on whether positive or negative effect, this allows us to introduce an exponential prior distribution over the covariate coefficient. This avoids non-identifiability of the product $\beta_x \hat{x}(\cdot)$, which would arise if β_x were given a Gaussian prior.

4.4 Value Plugin (VP) and Uncertainty Plugin (UP) Methods

To simplify notation, we denote \mathcal{Z} as $\{z_p\}$ for the aggregated covariate field case and $\{z(s_i)\}$ for the PointVal case from Section 4.2. For both cases, the aggregated counts and point patterns follow $N_p | \mathcal{Z} \sim \text{Pois} \left(\int_{A_p} \exp[\eta(\mathbf{s})] d\mathbf{s} \right)$, and $\mathcal{Y} | \mathcal{Z} \sim \text{PoPr}(\exp[\eta(\cdot)])$ respectively, where PoPr denotes a Poisson process. When aggregated values of $\hat{x}(\cdot)$ are needed, with $X_j = |\Omega_j|^{-1} \int_{\Omega_j} X(\mathbf{s}) d\mathbf{s}$, we estimate the covariate field via $\mathbb{E}(X_j | \mathcal{Z}) = |\Omega_j|^{-1} \int_{\Omega_j} \hat{x}(\mathbf{s}) d\mathbf{s}$ on a mesh. The smoothness of the estimated field depends on the mesh resolution, i.e. the volume $|\Omega_j|$.

In the estimation step, we compute $\hat{x}(\cdot)$ from Section 4.2. The Value Plugin (VP) method inputs the prediction into the full model as in equation (23), i.e. $\eta(\cdot) = \beta_0 + \tilde{\beta}_x \hat{x}(\cdot) + \epsilon_y(\cdot)$. The Uncertainty Plugin (UP) method incorporates $\hat{x}(\cdot)$ and a spatial uncertainty term $\epsilon_x(\cdot)$ in the second step,

$$\begin{cases} \eta(\cdot) = \beta_0 + \tilde{\beta}_x [\hat{x}(\cdot) + \epsilon_x(\cdot)] + \epsilon_y(\cdot), \\ \tilde{\beta}_x \sim \text{Exp}(\cdot), \epsilon_x \sim \mathbf{N}(\mathbf{0}, \hat{\mathbf{Q}}_{\epsilon_x}^{-1}), \text{ and } \epsilon_y \sim \mathbf{N}(\mathbf{0}, \mathbf{Q}_{\epsilon_y}^{-1}), \end{cases} \quad (24)$$

where ϵ_x and ϵ_y uses the same construction of \mathbf{u} in equation (6). From a modelling perspective, treating the noise ϵ_x as independent and identically distributed with a diagonal covariance matrix leads to identifiability issues. To address this, we explicitly provide the estimated precision matrix $\hat{\mathbf{Q}}_{\epsilon_x}$ (see Appendix C.7). For computational efficiency, separate meshes can be used for ϵ_x and ϵ_y (Section 5).

The estimation step smooths the covariate field, even when observational noise is present. Unless there are discontinuities in the field or model mismatches (e.g. omitted nonlinear effects), this first step typically produces a reasonable covariate model for the second step. Moreover, the estimated covariate field can always be checked before proceeding further.

The VP method shifts the uncertainty ϵ_x to the Matérn field noise ϵ_y , allowing estimation of only one noise term and thus significantly speeding up computation. In contrast, ϵ_x and ϵ_y in the UP method are inevitably confounded, requiring a sufficiently fine mesh to minimise nonlinearity within mesh elements and reduce computational strain from linearisation. For uncertainty quantifi-

cation, we aim to infer and incorporate ϵ_x in the second step, as in equation (24). This uncertainty can be propagated by incorporating the precision matrix from the first step (see Appendix C.7).

4.5 Model Mismatch under Nonlinear (NL) Misspecification

The nonlinear misspecification is introduced by replacing the linear predictor $\eta(s)$ in equation (21) with a nonlinear function $f(\cdot)$, i.e. $\check{\eta}(\cdot) = \beta_0 + \beta_x f(z(\cdot)) + u(\cdot)$. The nonlinear function $f(\cdot)$ can be any nonlinear function, such as exponential or logarithmic. The nonlinear misspecification can be viewed as a model mismatch, where the true model is not linear in the covariate field. We reuse the model frameworks, i.e. JU, UP and VP methods, specified in Sections 4.3 and 4.4, to adapt the nonlinear (NL) misspecification in the simulation study in Section 5.2.3. We aim to check the robustness of these frameworks for the mismatched nonlinear predictor.

5 Simulation Study

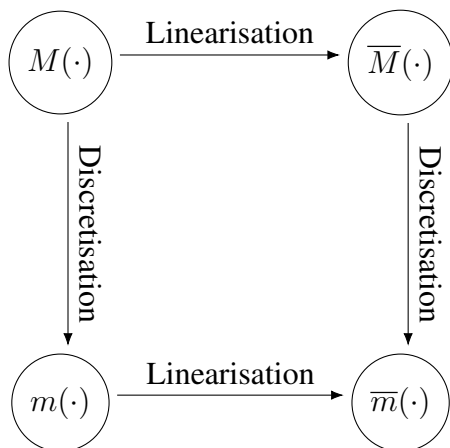


Figure 1: Conceptual diagram of the linearisation and discretisation process. The workflow in the `inlabru` package: $M(\cdot) \rightarrow m(\cdot) \rightarrow \bar{m}(\cdot)$. The diagram is not communicative because $\bar{M}(\cdot) \rightarrow \bar{m}(\cdot)$ depends on the data.

We aim to investigate how mesh design, data resolution, and model formulation influence computational cost and model accuracy, using the linearisation approach. Here we simulate data to illustrate the workflow $M(\cdot) \rightarrow \bar{M}(\cdot) \rightarrow \bar{m}(\cdot)$ (see Figure 1). More precisely, we cannot evaluate

the discretisation workflow $\overline{M}(\cdot) \rightarrow \overline{m}(\cdot)$ analytically as this depends on the data. This is the reason why we assess this workflow through the simulation study.

5.1 Data

For a fair model comparison, we construct two meshes: *mesh (i)* — a hexagonal mesh composed of equilateral sub-triangles (edge length 3.958 km), offset inward from the smoothed, buffered inner boundary by two triangle edge lengths, covering the entire study area; and *mesh (ii)* — with 1.961 times edge lengths to that of *mesh (i)*. See Table 1 for a comparison of the mesh triangles and covariate raster cells, and Appendix C.6 for code.

The elements along the boundary are constructed according to the standard `fmesher` meshing algorithm (Lindgren, 2025). As discussed in Section 3.2.2, hexagonal meshes are optimal in the stationary isotropic random field setting since it minimises the discretisation effect. Both the inner and outer boundaries are buffered to smooth the mesh construction (see Appendix C.1).

The integration scheme takes account of the integration points of the triangular meshes whose density matches that of the `RastFull` raster and excludes points falling outside the boundary of each A_p (interior boundary) by removing their weights from the integration (see Appendix B.9). A more accurate result could be achieved by constructing the mesh to conform to the interior sub-boundary of each A_p . This would ensure that none of the integration points fall outside the interior boundary. However, this approach (available in experimental via `fmesher::fm_intersect()` from version 0.6.1) is not used here because the high-resolution interior boundary complicates mesh construction, making the computation expensive.

This simulation study is inspired by a simplified landslide occurrence model in which landslide polygons are represented by their centroids, as centroids provide a consistent and well-defined point-based approximation of polygonal features. The covariate field reflects ground shaking from multiple seismic sources over a time window, while the Matérn field captures underlying geomorphological structures. We simulate point pattern observations over Nepal as a test of method as in

equation (1) with the linear predictor

$$\eta(\mathbf{s}) = \beta_0 + \beta_x x(\mathbf{s}) + u(\mathbf{s}), \quad (25)$$

where $x(\mathbf{s})$ is a continuous covariate field formulated as $(s_1^2 - s_2^2) \exp[-\frac{1}{2}(s_1^2 + s_2^2)]$; $s_1 \in [-4, 4]$, $s_2 \in [-2, 2]$ projected to Nepal, and $u(\mathbf{s})$ is defined in equation (6). We set $\beta_0 = -7$, $\beta_x = -6$ and $u(\mathbf{s})$ with $\rho = 50$ and $\sigma = 0.5$. Both β_0 and β_x are chosen to keep coefficient estimation computationally manageable in this toy example, ensuring that the covariate signals are distinguishable from the Matérn noise component. We also aggregate count observations $N_y(A_p)$ where A_p is the p -th administrative region in Nepal for $p = 1, \dots, 777$. This results in 139 simulated observed points. The Coordinate Reference System (CRS) of the data is converted into Universal Transverse Mercator (UTM) zone 44N and are converted into kilometre (km) units. We simulate point pattern observations based on the intensity field evaluated pointwise at the *mesh* (i) nodes (see code and plots in Appendices C.2 and C.3 respectively).

5.2 Simulation Scenarios

We consider both point pattern or aggregated count observations with the following scenarios for the observed covariate field: (1) Perfect detection of every covariate raster at full resolution (RastFull) of $0.858\text{km} \times 0.859\text{km}$ (Section 5.2.1); (2) Covariate raster aggregation (RastAgg) by taking the mean of the RastFull, at a resolution of $8.584\text{km} \times 8.592\text{km}$ (Section 5.2.1); (3) Polygon aggregation (PolyAgg) by taking the mean of the RastFull across administrative regions in Nepal, i.e. $n_A = 777$ piecewise-constant polygons (Section 5.2.1); (4) Incomplete covariate field of PolyAgg and Point Values (PointVal) (Section 5.2.2); and (5) nonlinear model misspecification of PolyAgg and PointVal. We refer to Scenarios (1)–(3) as aggregation scenarios, and Scenario (4) as the incomplete covariate field scenario. Under the aggregation scenarios, the covariate input methods in RastFull, RastAgg, and PolyAgg are termed Observation Plugin (OP), yielding six models for point pattern and aggregated count observations. The RastFull model with point pattern observa-

tions serves as a benchmark, with u defined on $mesh(i)$ (Section 4.1). For the incomplete covariate field scenario, we consider three methods - Joint Uncertainty (JU) and the two-stage approaches, Value Plugin (VP) and Uncertainty Plugin (UP) - for both PointVal and PolyAgg, giving twelve models in total, with the estimated covariate field $\hat{x}(\cdot)$ with the rasterised mesh elements (1.616 km \times 1.616 km; see Appendix C.7.1 for code), ϵ_x on $mesh(i)$ and ϵ_y on $mesh(ii)$ (see Sections 4.3 and 4.4). We then extend Scenarios (3) and (4) to Scenario (5), which introduces nonlinear (NL) misspecification. Specifically, this involves model mismatch where linear models are used to fit observations generated from a nonlinearly transformed covariate field under the incomplete covariate setting (Section 5.2.3). This again results in twelve models in total. The components u , ϵ , ϵ_x , and ϵ_y are all assigned PC priors (see Appendix C.5; Fuglstad et al. (2019)). We summarise above in a flowchart in Figure 2.

The function on the mesh is defined to be piecewise linear, hence the resolution of the mesh should be similar to that of the data in the optimal case; otherwise we do not fully utilise the data information. Having said that, the $mesh(i)$ resolution in the simulation is roughly 4 times larger than the covariate raster data at full resolution in Scenario (1). Here we compromise the information from the data to make the computation more efficient. Therefore, it provides insight into the case when we slightly relax the rule of thumb mentioned in Section 3.2.2.

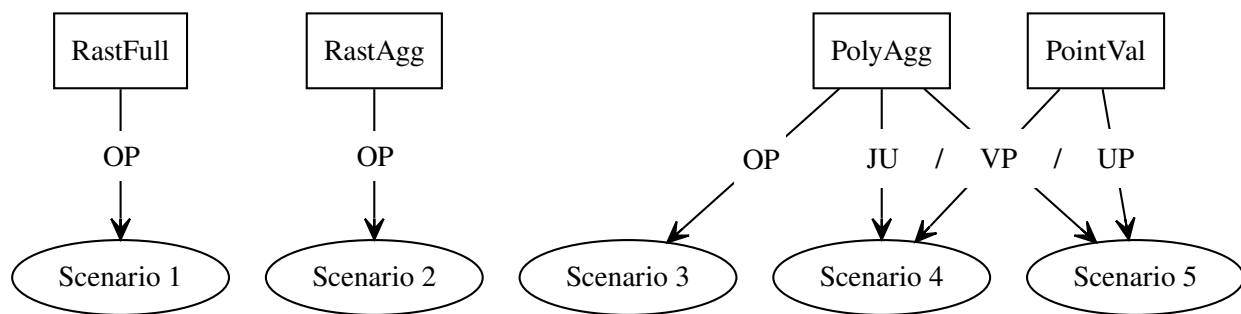


Figure 2: Flowchart of the simulation scenarios. The aggregation scenarios consist of: Raster at Full Resolution (RastFull), Raster Aggregation (RastAgg) and Polygon Aggregation (PolyAgg). The incomplete covariate field scenario is divided into two cases: Point Values (PointVal) and PolyAgg. OP: Observation Plugin, JU: Joint Uncertainty, VP: Value Plugin, UP: Uncertainty Plugin.

5.2.1 Rasterisation and Polygon Aggregation (PolyAgg) of Covariate Field

We compare the effect of the scales of raster aggregations in the covariate field. In Scenario (1), the covariate field is evaluated at the centre of each raster cell. This corresponds to satellite data that can be obtained everywhere and is treated as constant within each cell. For Scenario (2), we aggregate covariate raster in Scenario (1) into super-cells by a factor of 10. In this case, reconstruction of the continuous covariate field can be easily done in the same spirit as in Section 4.2. Under Scenario (3), we aggregate the covariate by averaging the rasters from Scenario (1) over administrative regional polygons. Rasterisation and polygon aggregation can be viewed as a limited set of observed field as the field is not fully observed, and we wish to quantify the accuracy and uncertainty from the resulting estimation procedures.

5.2.2 Incomplete Covariate Field for Point Values (PointVal)

For PointVal, we observe a limited set of measured values of the continuous covariate field $x(\mathbf{s})$ at a finite set of locations, $\{s_i\}$. We assume Gaussian additive noise for the observed covariate values and thus construct an extra layer in the Bayesian hierarchy to model the covariate field. Let z_i denote the observation of $x(s_i)$ with Gaussian additive noise term ϵ_{x_i} so that,

$$z_i = x(s_i) + \epsilon_{x_i}, \epsilon_{x_i} \sim \mathbf{N}(0, \sigma_{\epsilon_x}^2), i = 1, \dots, n_z. \quad (26)$$

We randomly sample $n_z = 777$ observed covariate points, with spatially uniform sampling density within each polygon, and then add noises $\sigma_{\epsilon_x}^2 = 0.1$ to these stratified samples (see Appendix C.4). This contrasts with the PolyAgg case where only the means of each polygon are used.

5.2.3 Nonlinear (NL) Misspecification

We extend the framework to examine model robustness under nonlinear (NL) misspecification and mismatch conditions. For the data generating mechanism, we transform covariate field via a nonlinear transformation $f(\cdot)$, i.e. $\log \check{\lambda}(\cdot) = \check{\eta}(\cdot) = \beta_0 + \beta_x f[x(\cdot)] + u(\cdot)$, where $f[x(\cdot)] =$

$b^{-1} \exp [ax(\cdot)] - c$, and we set $a = 3$, $b = 9$ and $c = 3$. We then simulate point patterns $\check{\mathcal{Y}}$ and aggregated count observations $\check{\mathcal{N}}$ accordingly. This formulation results in $\check{n} = 149$ simulated point observations. The resulting shift in the covariate and intensity field compared to the original simulation is shown in Figure 3.

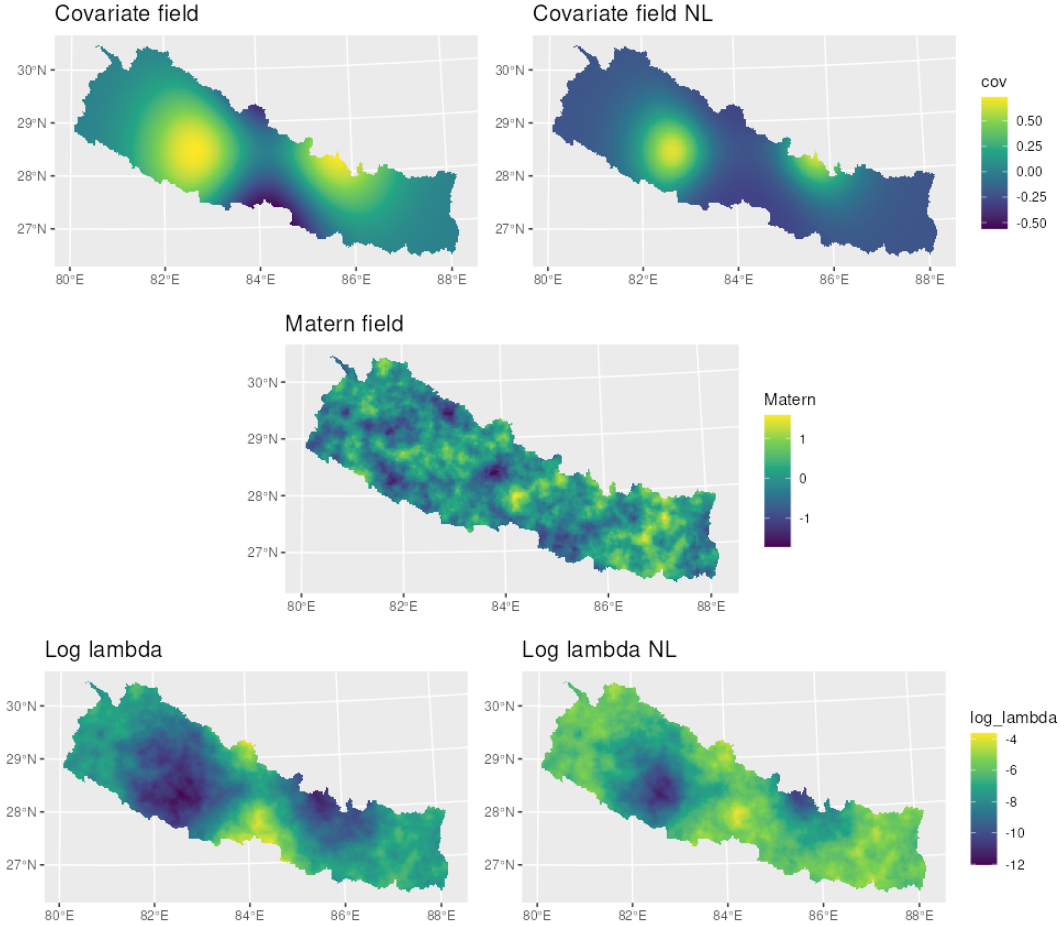


Figure 3: Covariate fields $x(\cdot)$ and $f(x(\cdot))$ (top row), Gaussian Matérn field $u(\mathbf{s})$ (middle) and the intensity fields $\log(\lambda)$ and $\log(\check{\lambda})$ (bottom row); where top two and bottom two share the same legend respectively. NL: Nonlinear misspecification.

5.3 Profile Likelihood for Uncertainty Propagation

Before presenting the results for the full two-dimensional cases in Sections 5.1 and 5.2, we first assess the robustness of the JU, VP, and UP methods using a one-dimensional toy example with the profile likelihood, noting that JU and UP incorporate uncertainty propagation. Specifically,

we estimate the optimal values of β_0 , β_x , and ϵ_{x_i} from the log-posterior density. We consider the extreme case where $\{X(s_i)\}_{i=1}^{n_z}$ are independent of each other, so that the estimation of $X(s_i)$ cannot borrow strength from another location, $s_i \neq s_{i'}$. We formulate the observed covariate field as $z(s_i) = X(s_i) + \epsilon_{x_i}$, $X(s_i) \sim \mathbf{N}(0, \sigma_x^2)$, $\epsilon_{x_i} \sim \mathbf{N}(0, \sigma_{\epsilon_x}^2)$. Assuming no missing observations,

$$\begin{cases} X(s_i)|z(s_i) & \sim \mathbf{N}(\hat{x}_i, \sigma_{x_i|z(s_i)}^2), \\ \mathcal{Y}|\hat{x}_i : \eta(s_i) & = \beta_0 + \beta_x(\hat{x}_i + \epsilon_{x_i}) + \epsilon_{y_i}, \epsilon_{x_i} \sim \mathbf{N}(0, \sigma_{x_i|z(s_i)}^2). \end{cases}$$

We aim to check the asymptotic behaviour when $n_z \rightarrow \infty$,

$$\begin{aligned} \mathbf{p} &:= \log \mathbb{P}[(\beta_0, \beta_x, \epsilon_{x_i})|\{X(s_i)\}] \\ &= \sum_i (-e^{\eta_i} + \eta_i y_i) - \frac{1}{2} \left[\left(\frac{\beta_0^2}{\sigma_{\beta_0}} \right)^2 + \left(\frac{\beta_x}{\sigma_{\beta_x}} \right)^2 + \sum_{i=1}^{n_z} \left(\frac{\epsilon_{x_i}}{\sigma_{x_i|z(s_i)}} \right)^2 \right]. \end{aligned} \quad (27)$$

We have not found a closed form expression for the optimal value of the derivative from equation (27) (see Section C.8.1 in Appendix C.8). For this reason, we instead use numerical optimisation to find the optimal $(\beta_0, \beta_x, \epsilon_{x_i})$. Since our focus is on β_x , we use the profile likelihood to optimise β_x with $n_z \in \{2, 4, 8, 16, 32, 64, 128, 256\}$, $\arg \max_{\beta_x} (\arg \max_{(\beta_0, \epsilon_x)}(\mathbf{p}))$.

The plots of the log-posterior density against β_x in Appendix C.8.2 show that all the profile posterior modes converge to the true value of β_x as n_z increases. Although, in the plots for UP method (Figure 19, Appendix C.8.2), the profile likelihood is not a strictly convex function though the global maximum is distinct from the local maximum as β_x approaching to infinity. It might pose problem for the optimisation algorithm and one should be careful about the initial starting points. However, we did not encounter any issues in our simulation (see Sections 6.3 and 6.4).

6 Results

A prediction score $S(F, \lambda)$ evaluates some measure of closeness between a pointwise estimate identified by a predictive distribution F , and an observed value λ . We define the expectation of

a score as $S(F, G) = \mathbb{E}_{\lambda \sim G}[S(F, \lambda)]$. A negatively oriented score (i.e. the lower the score, the better) is proper if it fulfils $S(F, G) \geq S(G, G)$. This implies that any predictive distributions with a higher or lower prediction uncertainty, other than the true one, will not lead to a better score on average (Gneiting and Raftery, 2007). The Squared Error (SE), $S_{SE}(F, \lambda) = (\lambda - \hat{\lambda}_F)^2$, and Dawid-Sebastiani (DS) score, $S_{DS}(F, \lambda) = \sigma_F^2(\hat{\lambda})^{-1}(\lambda - \hat{\lambda}_F)^2 + \log[\sigma_F^2(\hat{\lambda})]$, are common proper scoring rules (Dawid and Sebastiani, 1999). The Mean Squared Error (MSE) and Mean Dawid-Sebastiani (MDS) score for the points across a space are defined as $S(\{F_i\}, \{\lambda_i\}) = n^{-1} \sum_{i=1}^n S(F_i, \lambda_i)$.

We compare the prediction accuracy via the proper scoring rules, namely the SE and DS scores for the intensity field. The lower the score, the better the model is. We evaluate the mean scores for the intensity field pointwise at $n = 56,809$ evenly distributed point locations across Nepal. We compute these scores of the intensity field for the simulation models because the true simulated intensity field allows us to compare across point and aggregated count observation models.

6.1 Intensity Estimation under Aggregation Scenarios

We compare the performances of the RastFull, RastAgg and PolyAgg OP models for point patterns and aggregated count observations here. In Table 2, the point pattern models outperform the corresponding aggregated count models in both scores. The RastFull point pattern models achieves the best scores. As the aggregation scale and irregularity increase, the scores worsen across each observation category. The MDS scores for the RastFull and RastAgg models are similar due to well-justified variances. The score distributions are shown in Figures 4 and 5. The plots retain a piecewise linear pattern for both the RastAgg and PolyAgg models. In Figure 4, most SEs are concentrated in the central region, where the majority of observed points are located. In contrast, the aggregated count models exhibit better DS scores in the smaller provinces due to averaging effects. This observation leads us to consider projecting point observations onto mesh nodes, which will be discussed in Section 7. Despite this, the overall MDS scores remain lower for point pattern models. Figure 5 shows that the DS plots for aggregated count models display more consistent variances compared to point pattern models.

6.2 Covariate Estimation under Incomplete Covariate Field Scenario

The PolyAgg and PointVal models are not directly comparable under incomplete covariate field scenario (see Table 4 in Appendix C.9) as the latter includes Gaussian additive noise term ϵ_{x_i} from equation (26), while the former does not. However, this noise term negatively impacts the scores

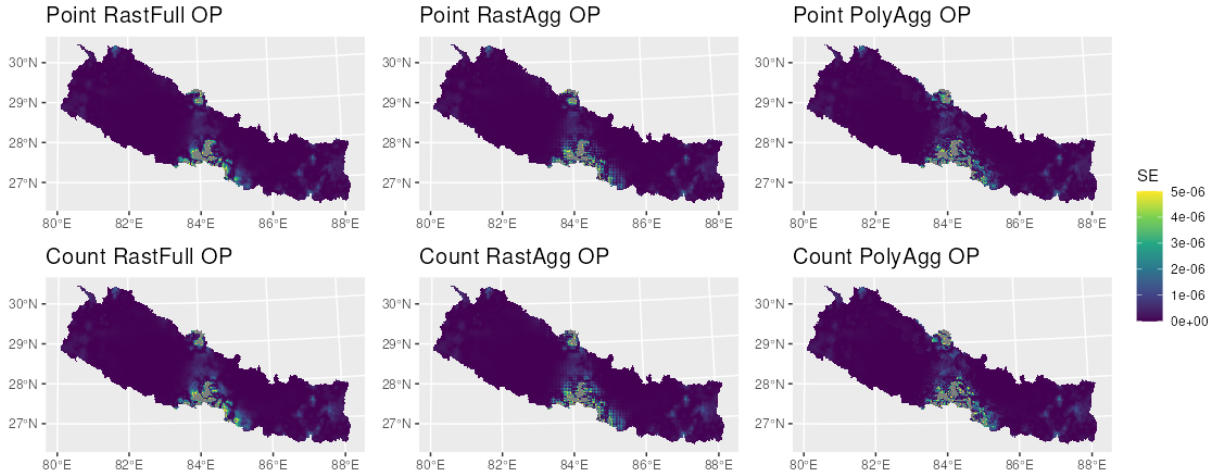


Figure 4: Squared Error (SE) for the intensity field λ across the models under aggregation scenarios (truncated at 5×10^{-6}). Point Pattern (top row) and Aggregated Count (bottom row) observation models. $\bar{\lambda} = 2.456 \times 10^{-3}$. RastFull: Raster at Full Resolution, RastAgg: Aggregated Raster, PolyAgg: Polygon Aggregations, OP: Observation Plugin.

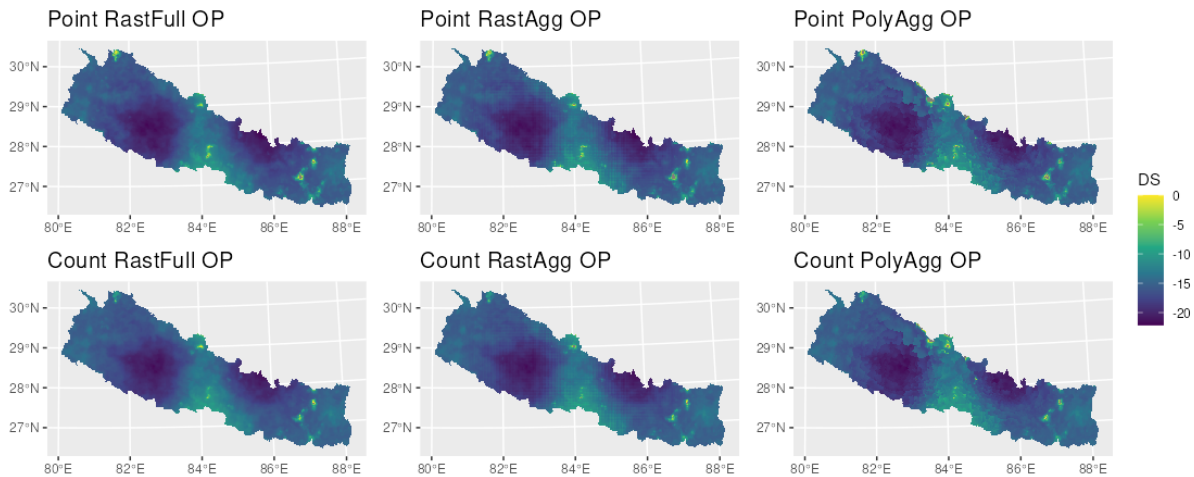


Figure 5: Dawid-Sebastiani (DS) score for the intensity field λ across the models under aggregation scenarios (truncated at 0). Point Pattern (top row) and Aggregated Count (bottom row) observation models. RastFull: Raster at Full Resolution, RastAgg: Aggregated Raster, PolyAgg: Polygon Aggregations, OP: Observation Plugin.

though stratified sampling for each polygon provides more precise point locations of the covariate field. This may partly explain why the PolyAgg models achieve better scores than PointVal models in predicting the covariate field. Under both PolyAgg and PointVal categories, the JU models outperform the VP and UP models. This suggests that jointly modelling the intensity and covariate fields offers more informative predictions than modeling them separately. For the PointVal category, the point pattern JU model slightly outperforms the corresponding aggregated count model in both scores.

Consequently, we will see how the predicted covariate fields may have an knock-on effect on the intensity field prediction in the following subsection given the covariate field is only part of the story to predict the intensity field. It is worth mentioning that there are visible hotspots in DS plots (see Appendix C.9 for DS and other plots) due to lower uncertainty where the observed points are.

6.3 Intensity Estimation under Incomplete Covariate Field Scenario

We compare the performances of the PolyAgg and PointVal models with OP, JU, VP and UP methods for point pattern and aggregated count observations here. In Table 2, in terms of MSE scores for the intensity field estimation under PolyAgg, the JU and UP models perform better than the OP model while the VP models perform worse. Hence, these results underscore the critical role of uncertainty quantification in intensity field prediction and downscaling the covariate field may not improve the model. The JU models perform better than the UP models in terms of MSE score and very close in terms of MDS score. This suggests that the joint estimation provides a slight edge for the robustness against the additional noises. However, the MDS scores of the JU and UP models are similar to the OP models, which might be due to the extra uncertainty introduced via the covariate field estimation (see discussion in Section 7).

The performance of PolyAgg models surpasses than that of the corresponding PointVal models due to the additional noises in the PointVal covariate observations, as in the covariate field estimation in the previous subsection. Across all PolyAgg and PointVal categories, the JU models achieve the highest scores or come very close. Despite the under-performance in estimating the

predicted covariate field in both PolyAgg and PointVal, the UP models perform reasonably well. In Figure 6, the areas with large SE (where high SE are truncated in grey for visualisation) for the VP models are larger compared to the JU and UP models in the regions with dense observations. The DS plots in Figure 7 show similar effects and the JU and UP models perform better in regions with fewer observations. Hence, this suggests the scores are consistent across Nepal.

Overall, the PolyAgg and PointVal models with the JU and UP methods show significant improvements, compared to the piecewise linear approach in the PolyAgg model in the previous subsection. The hotspots observed in DS plots for predicting the covariate field in the previous subsection are no longer observed in the DS plots for predicting the intensity field. This is likely because the Matérn field compensates for the under-performance at those locations.

6.4 Intensity Estimation under Nonlinear (NL) Misspecification

We compare the performances of the PolyAgg and PointVal models with JU, VP and UP methods for point pattern and aggregated count observations under NL here. In Table 3, the JU and UP models clearly outperform the VP models due to the uncertainty propagation. The scores also are the measures of the robustness of these models under the NL misspecification towards model misspecification. The linearisation and Matérn noise term ϵ_y are not flexible enough for the VP method to account for the model misspecification. Indeed, both JU and UP methods are better than the VP one in terms of MSE and, particularly, MDS scores. This is consistent with both the SE and DS plots in Figures 8 and 9. This implies that the uncertainty propagation is better explained in terms of variance thanks to the extra noise term in the UP methods.

Indeed, the VP method under NL misspecification is not as bad as expected in MSE scores because the Matérn field term $u(s)$ compensates for the model misspecification. Empirically, the JU and UP methods are more robust than the VP method. Again, we observe the PolyAgg models are better than the corresponding PointVal ones due to the additional noises in the observed covariate field. Surprisingly, the aggregated count models are better than point pattern ones in both scores. In Figure 9, the DS plots show the spread of the truncated area more clearly. This finding

leads us to consider the projection of point observations into weights on mesh nodes to better explain the variance (see Section 7 for discussion).

7 Conclusion and Discussion

Aggregating data to align common geometric objects is a standard approach to addressing spatial misalignment, but it introduces systematic biases that weaken statistical inference. We developed a disaggregation framework with uncertainty quantification that enables continuous-domain mod-

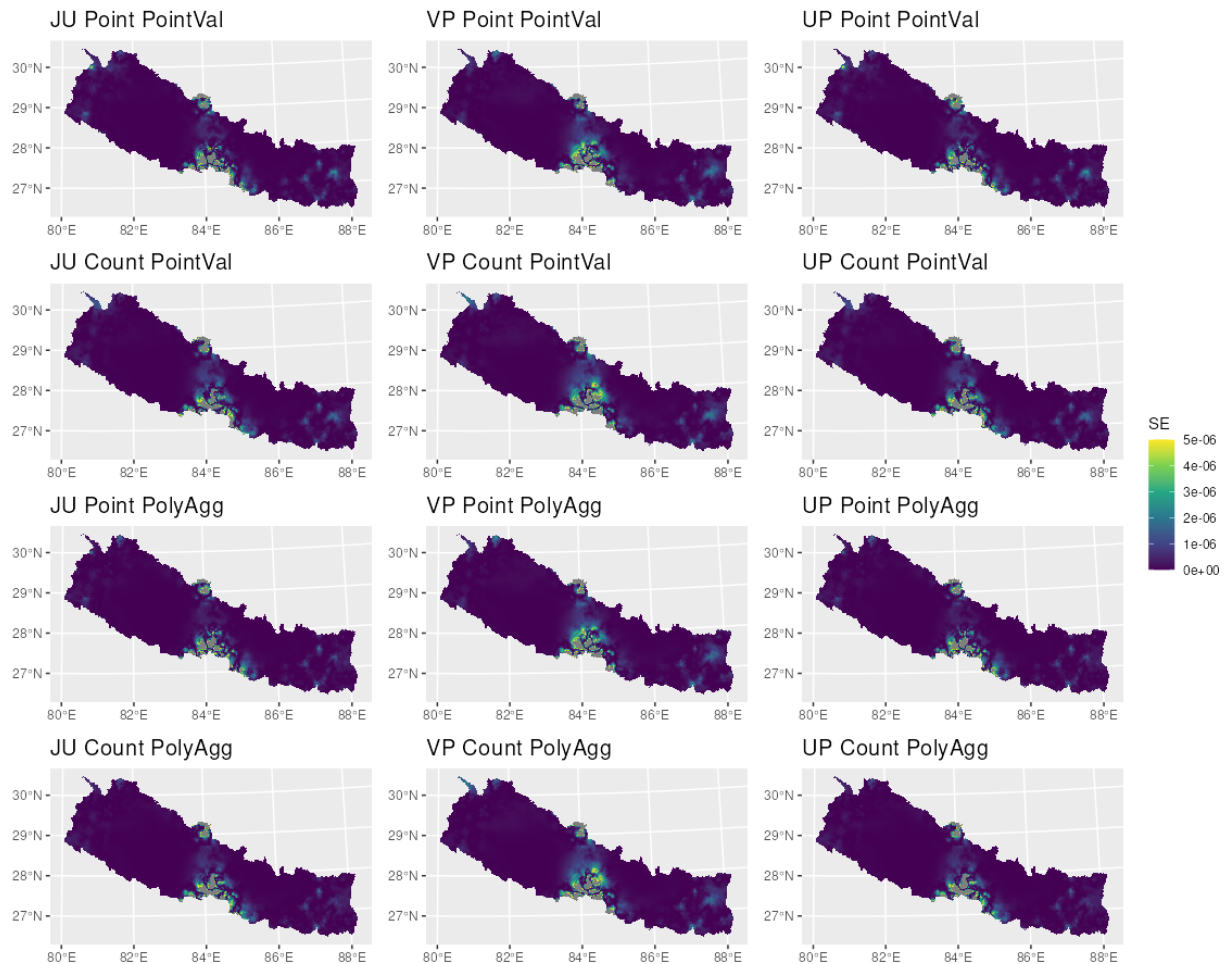


Figure 6: Squared Error (SE) for the intensity field λ across the models under incomplete covariate field scenario (truncated at 5×10^{-6}). JU: Joint Uncertainty, VP: Value Plugin, UP: Uncertainty Plugin, Point: Point Pattern, Count: Aggregated Count, PolyAgg: Polygon Aggregation, PointVal: Point Values. $\bar{\lambda} = 2.456 \times 10^{-3}$.

elling of both point pattern and aggregated count data while mitigating these biases. We applied this method to a landslide-motivated case study using synthetic data, demonstrating that it can recover the true underlying field under complex situations. These studies demonstrated that our approach achieved lower Mean Squared Error (MSE) and Dawid–Sebastiani (MDS) scores, with models based on point patterns and high-resolution raster covariates performing best, and traditional aggregated-count models performing worst. These results underscore the importance of preserving point-level information and propagating uncertainty. Under incomplete covariate fields and nonlinear model misspecification (i.e. modelling a nonlinear field as linear), Joint Uncertainty

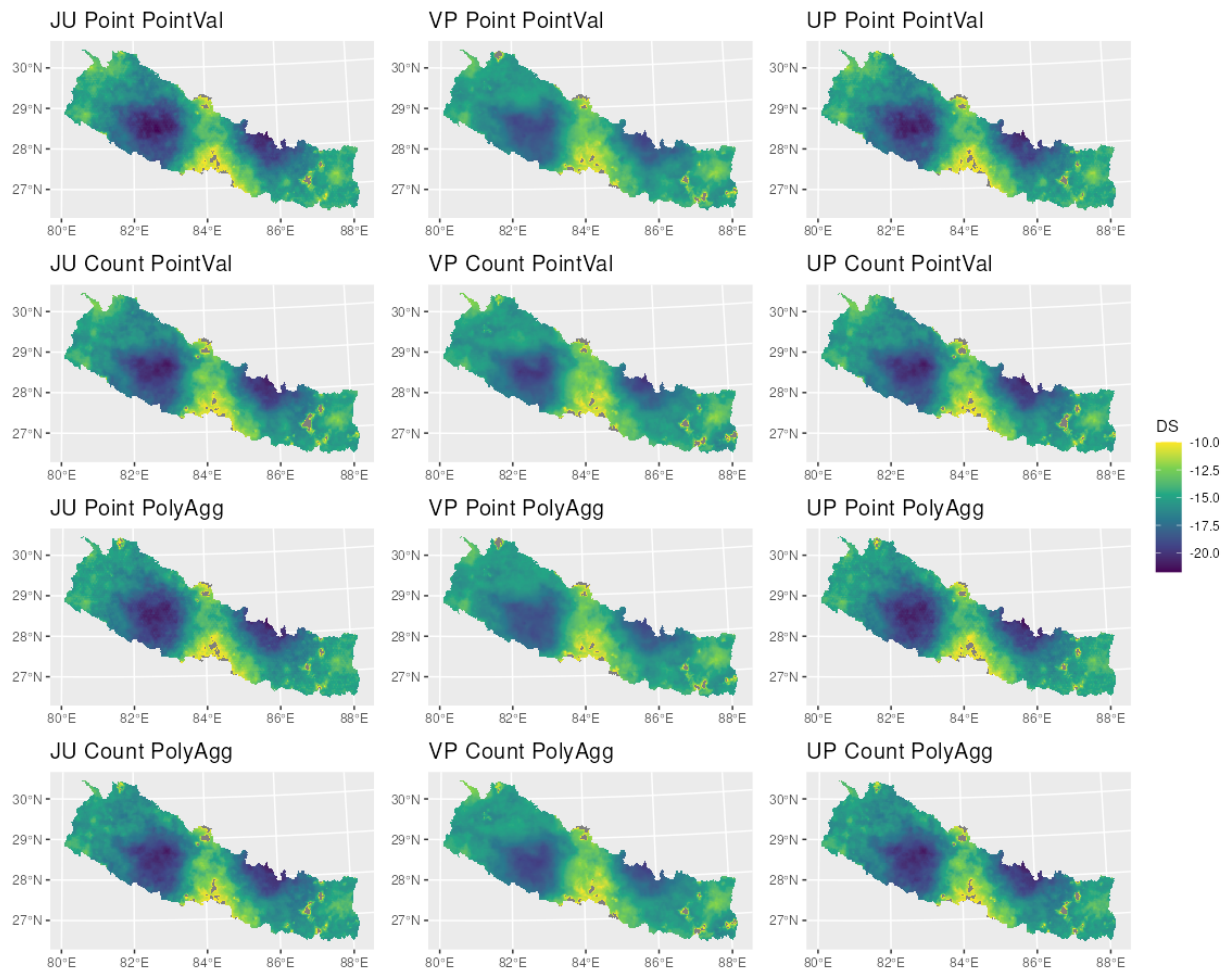


Figure 7: Dawid-Sebastiani (DS) score for the intensity field λ across the models under incomplete covariate field scenario (truncated at -10). JU: Joint Uncertainty, VP: Value Plugin, UP: Uncertainty Plugin, Point: Point Pattern, Count: Aggregated Count, PolyAgg: Polygon Aggregation, PointVal: Point Values.

(JU) and Uncertainty Plugin (UP) models consistently outperformed the Value Plugin (VP) model, with UP models offering computational efficiency and improved control over covariate predictions. As the correct linear predictor is rarely known a priori, our framework provides a flexible and robust basis for inference under both uncertainty propagation and misspecification.

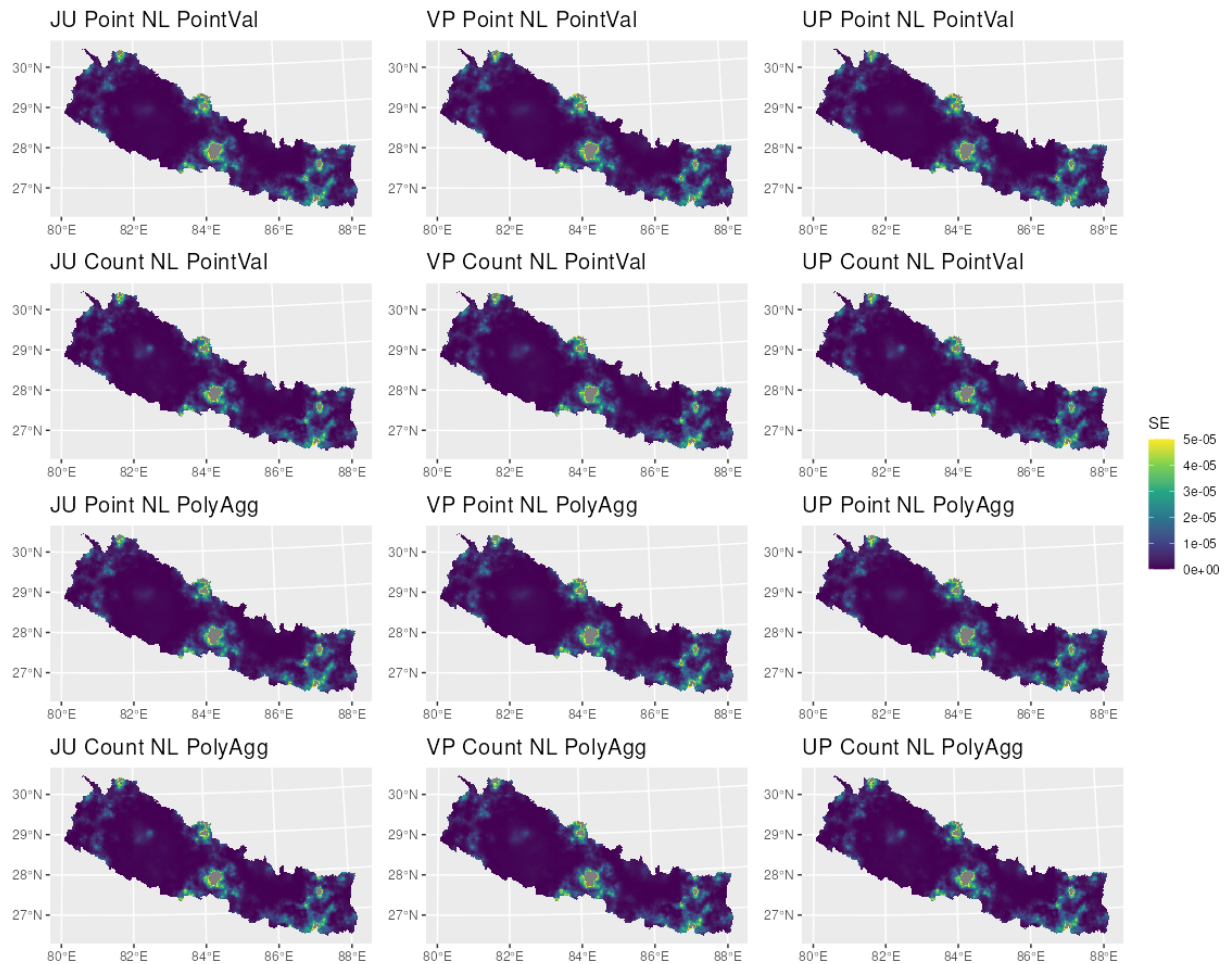


Figure 8: Squared Error (SE) for the intensity field λ across the misspecified models under incomplete covariate field scenario (truncated at 5×10^{-5}). JU: Joint Uncertainty, VP: Value Plugin, UP: Uncertainty Plugin, Point: Point Pattern, Count: Aggregated Count, NL: Nonlinear misspecification, PolyAgg: Polygon Aggregation, PointVal: Point Values. $\bar{\lambda} = 2.456 \times 10^{-3}$.

7.1 Limitations and Future Research Directions

To streamline the paper’s focus, we did not explore alternative precision matrices for uncertainty propagation (see Section 4.4 and Appendix C.7). The number of iterations needed for convergence is unpredictable and depends on factors such as tolerance levels, line search direction, mode assessment in INLA, the data, and the model specification (see convergence diagnostics in Appendix D). Further research is needed to determine the optimal settings. Implementing automatic differentiation can help accelerate computation (Carpenter et al., 2015).

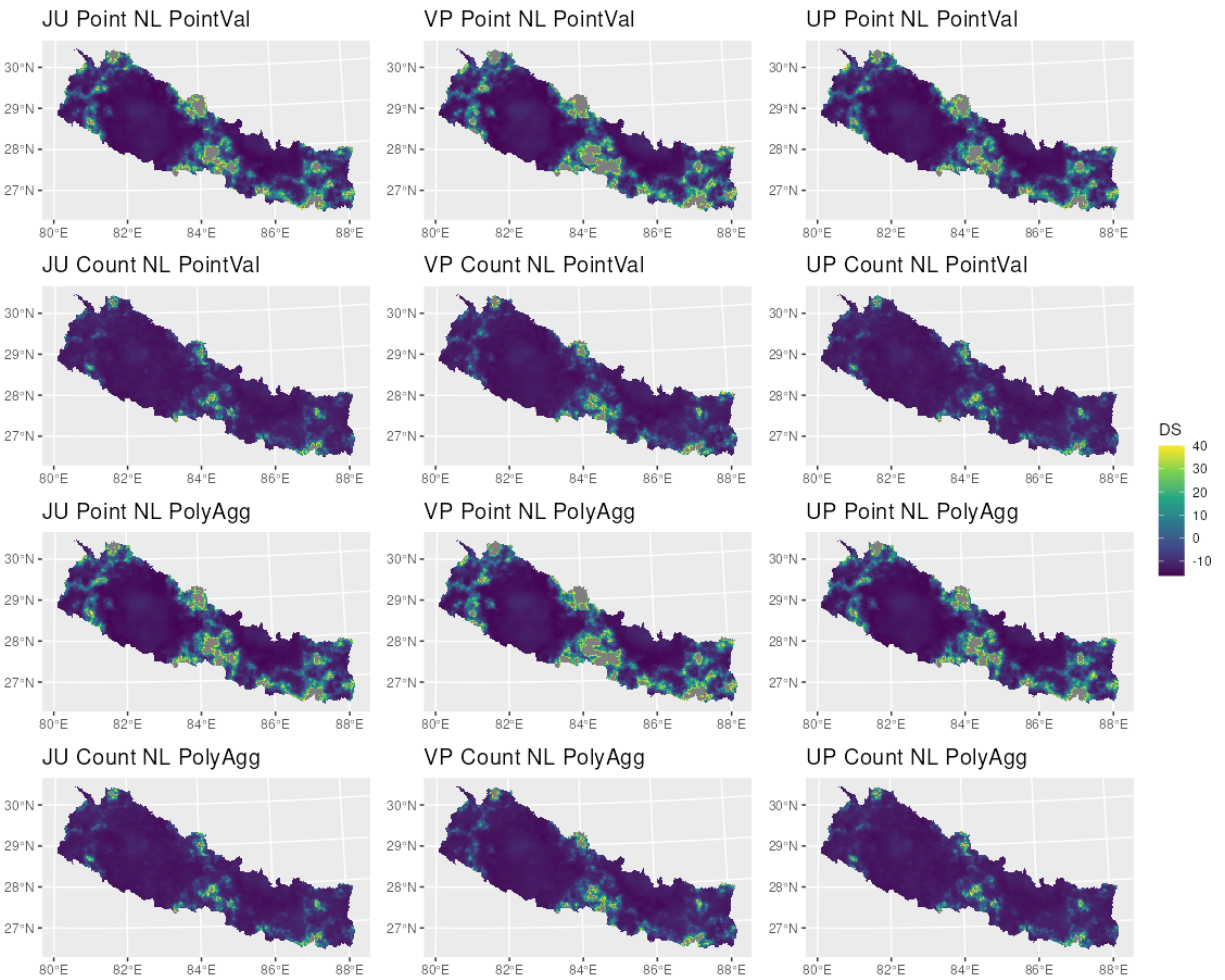


Figure 9: Dawid-Sebastiani (DS) score for the intensity field λ across the misspecified models under incomplete covariate field scenario (truncated at 40). JU: Joint Uncertainty, VP: Value Plugin, UP: Uncertainty Plugin, Point: Point Pattern, Count: Aggregated Count, NL: Nonlinear misspecification, PolyAgg: Polygon Aggregation, PointVal: Point Values.

Observations, including those related to landslides and other fields, are manually registered, introducing inherent uncertainties regarding their exact spatial and temporal accuracy. To address this, we can split the observed point information and project it onto nearby mesh nodes with partial weights so that we introduce uncertainty in a manner akin to aggregated count models but with more controlled adjustments. This approach helps mitigate the covariate field uncertainties caused by model misspecification.

The flexibility and *degrees of freedom (DoF)* of the estimated intensity field is determined by the mesh resolution. For the integration schemes, we need to respect the function variability and degrees of freedom to all spatial random fields to ensure a bounded likelihood approximation. In particular, this applies to Matérn effects defined on triangulation meshes and uncertainty propagation fields for high resolution covariates. If too few integration points were to be used, the nonlinear integral approximations would not sufficiently bound the likelihood. We address this by ensuring the integration scheme aligns with both mesh and covariate resolutions. Apart from the linearisation, the Matérn random field in our models indeed accounts for the data misalignment, which can be controlled under stricter PC priors.

The linearisation becomes more stable with an increase in integration points. A finer mesh by subdividing the elements would stabilise the linearisation further (see Appendix B.9). There is a fundamental difference between increasing the integration points within each element and subdivision of elements. The former adds more equally weighted points, while the latter creates more piecewise linear mesh elements to account for the nonlinearity. In the future, we will explore alternative integration schemes, such as Simpson’s rule or Gaussian quadrature.

7.2 Connection to INLA Extension Packages

In various applications, including landslides, there is often uncertainty regarding the exact locations, as these are determined manually. In some instances, we cannot revert to the original trigger location over time. Hence, contour map can be useful in assessing the joint uncertainty excursion sets via `excursions` package (Bolin and Lindgren, 2017). These maps add an extra dimension

for evaluating contour credible risk regions and help propagate uncertainty arising from the aggregation. Assuming stationarity can be quite restrictive. Extending the models to nonstationary and anisotropic scenarios would be complex, as it requires understanding how meshing and linearisation adapt to underlying unknown nonstationary and anisotropic features (Llamazares-Elias et al., 2024). One potential workaround is to ensure that the mesh resolution is sufficiently fine to accommodate the shortest range of the anisotropic field. Another extension is to consider the nonseparable class of models using the `INLAspacetime` package (Lindgren et al., 2020). The linearisation would work the same for the diffusion process. In principal, a drift term can be incorporated into the Matérn field to account for the nonseparability. However, a caveat is that more data would be needed to accurately estimate these models.

We have extended the framework to incorporate river channel incision networks for landslide modelling (Suen et al., 2025), an important development given that landslides frequently cluster along drainage pathways. Including channel data improves the representation of spatial dependencies and strengthens susceptibility predictions. Another promising direction is to link our aggregation framework with metric graph models implemented in the `MetricGraph` package (Bolin et al., 2024). Integrating graph-based representations would enable modelling landslide risk along linear infrastructures such as road networks, supporting applications in road design, maintenance, and earthquake-driven evacuation planning.

References

- Alvioli, M., Guzzetti, F., and Marchesini, I. (2020). Parameter-free delineation of slope units and terrain subdivision of Italy. *Geomorphology*, 358:107124.
- Alvioli, M., Marchesini, I., Reichenbach, P., Rossi, M., Ardizzone, F., Fiorucci, F., and Guzzetti, F. (2016). Automatic delineation of geomorphological slope units with `r.slopeunits v1.0` and their optimization for landslide susceptibility modeling. *Geoscientific Model Development*, 9(11):3975–3991. Publisher: Copernicus GmbH.

- Baddeley, A., Bárány, I., and Schneider, R. (2007). Spatial point processes and their applications. Stochastic Geometry: Lectures Given at the CIME Summer School Held in Martina Franca, Italy, September 13–18, 2004, pages 1–75.
- Berrocal, V. J., Gelfand, A. E., and Holland, D. M. (2010). A spatio-temporal downscaler for output from numerical models. Journal of agricultural, biological, and environmental statistics, 15:176–197.
- Bolin, D. and Lindgren, F. (2017). Quantifying the uncertainty of contour maps. Journal of Computational and Graphical Statistics, 26(3):513–524.
- Bolin, D., Simas, A. B., and Wallin, J. (2024). Gaussian Whittle-Matérn fields on metric graphs. Bernoulli, 30(2):1611–1639.
- Cameletti, M., Gómez-Rubio, V., and Blangiardo, M. (2019). Bayesian modelling for spatially misaligned health and air pollution data through the inla-spde approach. Spatial Statistics, 31:100353.
- Carpenter, B., Hoffman, M. D., Brubaker, M., Lee, D., Li, P., and Betancourt, M. (2015). The stan math library: Reverse-mode automatic differentiation in c++. arXiv preprint arXiv:1509.07164.
- Dawid, A. P. and Sebastiani, P. (1999). Coherent dispersion criteria for optimal experimental design. Annals of Statistics, pages 65–81.
- Diggle, P. J. (2013). Spatial point processes. In Statistical Analysis of Spatial and Spatio-Temporal Point Patterns. Chapman and Hall/CRC, 3 edition. Num Pages: 28.
- Forlani, C., Bhatt, S., Cameletti, M., Krainski, E., and Blangiardo, M. (2020). A joint bayesian space-time model to integrate spatially misaligned air pollution data in r-inla. Environmetrics, 31(8):e2644.
- Fuentes, M. and Raftery, A. E. (2005). Model evaluation and spatial interpolation by bayesian combination of observations with outputs from numerical models. Biometrics, 61(1):36–45.

- Fuglstad, G.-A., Simpson, D., Lindgren, F., and Rue, H. (2015). Interpretable priors for hyperparameters for Gaussian random fields. arXiv preprint arXiv:1503.00256, 2.
- Fuglstad, G.-A., Simpson, D., Lindgren, F., and Rue, H. (2019). Constructing priors that penalize the complexity of Gaussian random fields. Journal of the American Statistical Association, 114(525):445–452.
- Gelfand, A. E., Zhu, L., and Carlin, B. P. (2001). On the change of support problem for spatio-temporal data. Biostatistics, 2(1):31–45.
- Gneiting, T. and Raftery, A. E. (2007). Strictly proper scoring rules, prediction, and estimation. Journal of the American statistical Association, 102(477):359–378.
- Gotway, C. A. and Young, L. J. (2002). Combining incompatible spatial data. Journal of the American Statistical Association, 97(458):632–648.
- Hjelle, Ø. and Dæhlen, M. (2006). Triangulations and Applications. Springer Science & Business Media. Google-Books-ID: cRXAe8CVbBYC.
- Kelejian, H. H. and Prucha, I. R. (1998). A generalized spatial two-stage least squares procedure for estimating a spatial autoregressive model with autoregressive disturbances. The journal of real estate finance and economics, 17:99–121.
- Konrad, J.-M. and Morgenstern, N. (1982). Effects of applied pressure on freezing soils. Canadian Geotechnical Journal, 19(4):494–505.
- Lambert, D. M., Brown, J. P., and Florax, R. J. (2010). A two-step estimator for a spatial lag model of counts: Theory, small sample performance and an application. Regional science and urban economics, 40(4):241–252.
- Lindgren, F. (2025). fmesher: Triangle Meshes and Related Geometry Tools. R package version 0.5.0.

- Lindgren, F., Bachl, F., Illian, J., Suen, M. H., Rue, H., and Seaton, A. E. (2024). inlabru: software for fitting latent Gaussian models with non-linear predictors. [arXiv preprint arXiv:2407.00791](#).
- Lindgren, F., Bakka, H., Bolin, D., Krainski, E., and Rue, H. (2020). A diffusion-based spatio-temporal extension of Gaussian Matérn fields. [arXiv preprint arXiv:2006.04917](#).
- Lindgren, F., Bolin, D., and Rue, H. (2022). The SPDE approach for Gaussian and non-Gaussian fields: 10 years and still running. [Spatial Statistics](#), 50:100599.
- Lindgren, F., Rue, H., and Lindström, J. (2011). An explicit link between Gaussian fields and Gaussian Markov random fields: the stochastic partial differential equation approach. [Journal of the Royal Statistical Society: Series B \(Statistical Methodology\)](#), 73(4):423–498.
- Liu, G.-R. (2009). [Meshfree methods: moving beyond the finite element method](#). CRC press.
- Llamazares-Elias, L., Latz, J., and Lindgren, F. (2024). A parameterization of anisotropic Gaussian fields with penalized complexity priors. [arXiv preprint arXiv:2409.02331](#).
- Loche, M., Alvioli, M., Marchesini, I., Bakka, H., and Lombardo, L. (2022). Landslide susceptibility maps of Italy: Lesson learnt from dealing with multiple landslide types and the uneven spatial distribution of the national inventory. [Earth-Science Reviews](#), 232:104125.
- Lombardo, L., Opitz, T., and Huser, R. (2018). Point process-based modeling of multiple debris flow landslides using INLA: an application to the 2009 Messina disaster. [Stochastic Environmental Research and Risk Assessment](#), 32(7):2179–2198.
- Lombardo, L., Opitz, T., and Huser, R. (2019). 3 - Numerical Recipes for Landslide Spatial Prediction Using R-INLA: A Step-by-Step Tutorial. In Pourghasemi, H. R. and Gokceoglu, C., editors, [Spatial Modeling in GIS and R for Earth and Environmental Sciences](#), pages 55–83. Elsevier.
- Moraga, P., Cramb, S. M., Mengersen, K. L., and Pagano, M. (2017). A geostatistical model

- for combined analysis of point-level and area-level data using inla and spde. Spatial Statistics, 21:27–41.
- Møller, J., Syversveen, A. R., and Waagepetersen, R. P. (1998). Log Gaussian Cox Processes. Scandinavian Journal of Statistics, 25(3):451–482.
- Opitz, T., Bakka, H., Huser, R., and Lombardo, L. (2022). High-resolution Bayesian mapping of landslide hazard with unobserved trigger event. The Annals of Applied Statistics, 16(3):1653–1675. Publisher: Institute of Mathematical Statistics.
- Rue, H., Gómez-Rubio, V., Bakka, H., Lenzi, A., Castro-Camilo, D., Simpson, D., Lindgren, F., and Krainski, E. (2018). Advanced Spatial Modeling with Stochastic Partial Differential Equations Using R and INLA. Chapman and Hall/CRC, New York.
- Rue, H., Martino, S., and Chopin, N. (2009). Approximate bayesian inference for latent gaussian models by using integrated nested laplace approximations. Journal of the Royal Statistical Society Series B: Statistical Methodology, 71(2):319–392.
- Simpson, D., Illian, J. B., Lindgren, F., Sørbye, S. H., and Rue, H. (2016). Going off grid: computationally efficient inference for log-Gaussian Cox processes. Biometrika, 103(1):49–70.
- Spiekermann, K. and Wegener, M. (2008). Environmental feedback in urban models. International Journal of Sustainable Transportation, 2(1):41–57.
- Suen, M. H., Naylor, M., Mudd, S., and Lindgren, F. (2025). Influence of river incision on landslides triggered in nepal by the gorkha earthquake: Results from a pixel-based susceptibility model using inlabru. arXiv preprint arXiv:2507.08742.
- Villejo, S. J., Illian, J. B., and Swallow, B. (2023). Data fusion in a two-stage spatio-temporal model using the inla-spde approach. Spatial Statistics, 54:100744.
- Whittle, P. (1954). On stationary processes in the plane. Biometrika, pages 434–449.

Whittle, P. (1963). Stochastic-processes in several dimensions. Bulletin of the International Statistical Institute, 40(2):974–994.

Wilkie, C. J., Miller, C. A., Scott, E. M., O'Donnell, R. A., Hunter, P. D., Spyrakos, E., and Tyler, A. N. (2019). Nonparametric statistical downscaling for the fusion of data of different spatiotemporal support. Environmetrics, 30(3):e2549.

Zhong, R. and Moraga, P. (2024). Bayesian hierarchical models for the combination of spatially misaligned data: a comparison of melding and downscaler approaches using inla and spde. Journal of Agricultural, Biological and Environmental Statistics, 29(1):110–129.

Tables

Abbreviations: Cov.: Covariate Observation, Obs.: Observation, $\bar{\lambda}(\cdot)$: Mean of Intensity Field, $\bar{\bar{\lambda}}$: Mean of Intensity Field under Nonlinear misspecification (NL), RastFull: Raster at Full Resolution, RastAgg: Aggregated Raster, PolyAgg: Polygon Aggregations, PointVal: Point Values, OP: Observation Plugin, JU: Joint Uncertainty, VP: Value Plugin, UP: Uncertainty Plugin, \mathcal{Y} : Point Pattern, \mathcal{N} : Aggregated Count, $\check{\mathcal{Y}}$: Point Pattern under Nonlinear misspecification (NL), $\check{\mathcal{N}}$: Aggregated Count under Nonlinear misspecification (NL).

	RastFull	RastAgg	Predicted raster	Mesh (i)	Mesh (ii)
Area (km ²)	0.737	73.70	2.61	6.785	26.1
Edge length (km)	0.858	8.58	1.62	3.96	7.76

Table 1: Comparison of the areas and edge lengths of raster cells and interior equilateral mesh triangles. See Section 5.1 for details.

Cov.	Obs.	Method	MSE	MDS	$\bar{\lambda}$
RastFull	\mathcal{Y}	OP	4.226×10^{-7}	-1.615×10^1	8.915×10^{-4}
RastAgg			4.559×10^{-7}	-1.610×10^1	
RastFull	\mathcal{N}		4.339×10^{-7}	-1.593×10^1	
RastAgg			4.706×10^{-7}	-1.591×10^1	
PolyAgg	\mathcal{Y}	JU	5.523×10^{-7}	-1.586×10^1	
		VP	5.946×10^{-7}	-1.521×10^1	
		UP	4.092×10^{-7}	-1.574×10^1	
		OP	5.995×10^{-7}	-1.579×10^1	
	\mathcal{N}	JU	4.541×10^{-7}	-1.578×10^1	
		VP	7.228×10^{-7}	-1.517×10^1	
		UP	4.540×10^{-7}	-1.578×10^1	
		OP	5.995×10^{-7}	-1.579×10^1	
PointVal	\mathcal{Y}	JU	4.400×10^{-7}	-1.568×10^1	
		VP	6.019×10^{-7}	-1.522×10^1	
		UP	4.933×10^{-7}	-1.560×10^1	
	\mathcal{N}	JU	4.690×10^{-7}	-1.568×10^1	
		VP	7.308×10^{-7}	-1.517×10^1	
		UP	5.354×10^{-7}	-1.561×10^1	

Table 2: Table of the Mean Squared Error (MSE) and Mean Dawid-Sebastiani (MDS) scores for the intensity field λ across the models under the aggregation and incomplete covariate field scenarios.

Cov.	Obs.	Method	MSE	MDS	$\bar{\lambda}$
PolyAgg	\check{Y}	JU	5.952×10^{-6}	-2.690	2.456×10^{-3}
		VP	6.150×10^{-6}	1.354	
		UP	5.948×10^{-6}	-2.901	
	\check{N}	JU	5.401×10^{-6}	-9.667	
		VP	5.682×10^{-6}	-8.125	
		UP	5.379×10^{-6}	-9.797	
PointVal	\check{Y}	JU	5.962×10^{-6}	-2.124	
		VP	6.152×10^{-6}	1.504	
		UP	5.964×10^{-6}	-2.170	
	\check{N}	JU	5.398×10^{-6}	-9.723	
		VP	5.702×10^{-6}	-7.940	
		UP	5.379×10^{-6}	-9.797	

Table 3: Table of the Mean Squared Error (MSE) and Mean Dawid-Sebastiani (MDS) scores for the intensity field λ across the models under the Nonlinear misspecification (NL).

Supplementary Information

Appendices

A Derivations related to Poisson Point and Count Processes

Here, we provide the derivations and implementations mentioned in Section 2.

A.1 Derivation of the likelihood function

Here, we provide the derivation of the likelihood function for the Poisson point process specified in Definition 2.3. Let $\mathcal{Y} = \{y_1, \dots, y_{N(\Omega)}\}$ be some observed point pattern, where $N(\cdot)$ is the random count measure on a bounded domain $\Omega \subset \mathbb{R}^d, d \in \mathbb{N}$, given some intensity function λ that is defined on every Borel measurable set $A \subseteq \Omega$. This point process is locally finite such that $N(A) < \infty$ for all A ; this implies the intensity functions are locally integrable (see Baddeley et al. (2007) for details). The likelihood function of the observed point pattern can be specified given the intensity function λ and $N(\Omega) = n$,

$$p_Y(\mathcal{Y}, N(\Omega) = n | \lambda) := \mathbb{P}(N(\Omega) = n | \lambda) \cdot p(\{y_1, \dots, y_n\} | \lambda, N(\Omega) = n),$$

where $p(\{y_1, \dots, y_n\} | \lambda, N(\Omega) = n)$ is the joint density function of the observations. Since event locations are conditional independent,

$$\begin{aligned} p_Y(\mathcal{Y}, N(\Omega) = n | \lambda) &= \mathbb{P}(N(\Omega) = n | \lambda) \prod_{i=1}^n p(y_i | \lambda, N(\Omega) = n) \\ &= e^{-\Lambda(\Omega)} \frac{[\Lambda(\Omega)]^n}{n!} \prod_{i=1}^n \frac{\lambda(y_i)}{\Lambda(\Omega)} \\ &= \frac{e^{-\Lambda(\Omega)}}{n!} \prod_{i=1}^n \lambda(y_i). \end{aligned}$$

For Poisson count process, we have the set of counts $\{N_p := N(A_p)\}_{p=1}^{n_A}$, the likelihood function is

$$\begin{aligned} p_Y(\{N_p\}|\lambda) &:= \mathbb{P}(\{N_p\}|\lambda) \\ &= e^{-\sum_p \Lambda(A_p)} \prod_p \frac{\Lambda(A_p)^{N_p}}{N_p!} \end{aligned}$$

The log-likelihood w.r.t a unit-rate count process is

$$\ell(\lambda; \{N_p\}) = |\Omega| - \Lambda(\Omega) + \underbrace{\sum_p N_p \log(\Lambda(A_p)) - \sum_p N_p \log(|A_p|)}_{:= \sum_p \log \lambda(A_p)}.$$

B Derivations related to Computation

Here, we provide the derivations mentioned in Section 3.

B.1 Derivations of first-order Taylor approximation

Derivations of $\bar{M}_j(\mathbf{u})$ and $\bar{m}_j(\mathbf{u})$ in equations (12) and (13) from Section 3.1 are shown here.

Assuming λ is log-linear,

$$\begin{aligned} - \int_{\Omega} \lambda(\mathbf{s}) d\mathbf{s} &= - \sum_{j=1}^J \int_{\Omega_j} \lambda(\mathbf{s}) d\mathbf{s} \\ &= - \sum_{j=1}^J \int_{\Omega_j} \exp[\underbrace{\log \lambda(\mathbf{s})}_{\approx \eta(\mathbf{s})}] d\mathbf{s} \end{aligned} \tag{B1}$$

$$\neq - \sum_{j=1}^J \exp \left(\int_{\Omega_j} \eta(\mathbf{s}) d\mathbf{s} \right) \tag{B2}$$

A common problem shown in equation (B2) is that the observed point locations are lost when being aggregated with respect to the subset Ω_j to overcome the data misalignment. Mathematically speaking, the exponential function and the integral function are not commutative. This can lead to

wrong estimation of intensity function thus the effects of the covariates.

Following equation (B1),

$$\begin{aligned}
& - \sum_{j=1}^J \int_{\Omega_j} \exp[\eta(\mathbf{s})] d\mathbf{s} \\
&= - \sum_{j=1}^J \exp \left[\underbrace{\log \left(\int_{\Omega_j} \exp[\eta(\mathbf{s})] d\mathbf{s} \right)}_{=: M_j(\mathbf{u}) \approx m_j(\mathbf{u}_*) + \mathbf{J}^{(j)}(\mathbf{u}_*)^\top (\mathbf{u} - \mathbf{u}_*) =: \bar{M}_j(\mathbf{u})} \right] \\
&\approx - \sum_{j=1}^J \sum_{k=1}^{n_j} w_{jk} \exp(\eta(\mathbf{s}_{jk})) \\
&= - \sum_{j=1}^J \exp \left[\underbrace{\log \left(\sum_{k=1}^{n_j} w_{jk} \exp[\eta(\mathbf{s}_{jk})] \right)}_{\approx m_j(\mathbf{u}) \approx m_j(\mathbf{u}_*) + \mathbf{J}^{(j)}(\mathbf{u}_*)^\top (\mathbf{u} - \mathbf{u}_*) =: \bar{m}_j(\mathbf{u})} \right]
\end{aligned}$$

It is worth noting that w_{jk} do not have unique solutions. Thus $\sum_{k=1}^{n_j} w_{jk}$ do not have to sum up to 1 because these account for the contributions of the integration points towards an integral via a stable integration scheme (see details in Appendix B.9).

When $J \rightarrow \infty$, then the function is closer to a piecewise linear function across Ω_j as $\Omega_j \rightarrow 0$, thus converges into the true field.

B.2 Continuous Linearisation Case

Here, we provide the proof for the continuous linearisation case mentioned in Theorem 3.1. We assume the following:

1. The function $M_j(\mathbf{u})$ is twice differentiable at some points $\mathbf{u}_* \in \mathbb{R}$; and
2. The linear predictor $\eta(\cdot) = b + \mathbf{A}\mathbf{u}$ is an affine function of \mathbf{u} .

Given the subset Ω_j does not depend on \mathbf{u} and by Leibniz's integral rule, the terms related to $\partial\Omega_j$ disappear. we spell out the derivation for the first and second-order partial derivatives of the

j -th term with respect to the l and l' , for $l, l' = 1, \dots, L$,

$$\frac{\partial M_j}{\partial u_l} = \frac{\int_{\Omega_j} \lambda(s) \nabla_u \eta(s) ds}{\int_{\Omega_j} \lambda(s) ds} < \infty, \quad (\text{B3})$$

$$\begin{aligned} \frac{\partial^2 M_j}{\partial u_l \partial u_{l'}} &= \frac{\partial}{\partial u_{l'}} \frac{\int_{\Omega_j} \lambda(s) \nabla_u \eta(s) ds}{\int_{\Omega_j} \lambda(s) ds} \\ &= \frac{\int_{\Omega_j} \lambda(s) \nabla_u \eta(s) \nabla_u^\top \eta(s) ds}{\int_{\Omega_j} \lambda(s) ds} - \frac{\int_{\Omega_j} \lambda(s) \nabla_u \eta(s) ds}{\int_{\Omega_j} \lambda(s) ds} \cdot \frac{\int_{\Omega_j} \lambda(s) \nabla_u^\top \eta(s) ds}{\int_{\Omega_j} \lambda(s) ds} < \infty. \end{aligned} \quad (\text{B4})$$

Hence, equations (B3) and (B4) are bounded because $\int_{\Omega_j} \lambda(s) ds$ is bounded by definition and $\nabla_u \eta(\cdot) = \mathbf{A}$ is bounded. We interpret equation (B4) as the difference between the product of gradient average and a product of average gradient. Recall that the predictor $\eta(\cdot)$ comprises of covariate contribution here; without such contribution, there might be identifiability issue.

The subsets can be specified as `block` argument with `ibm_eval` function in the `inlabru` package.

```
R> ibm_eval(..., input = list(block = .block, weights = weight))
```

B.3 Discretised Linearisation Case

Here, we provide the proof for the discretised linearisation case mentioned in Theorem 3.1. We assume the following:

1. The function $m_j(\mathbf{u})$ are twice differentiable at some points $\mathbf{u}_* \in \mathbb{R}$;
2. The linear predictor $\eta(\cdot) = b + \mathbf{A}\mathbf{u}$ is an affine function of \mathbf{u} .

Given the subset Ω_j does not depend on \mathbf{u} and by Leibniz's integral rule, the terms related to $\partial \Omega_j$ disappear, we spell out the derivation for the first and second-order partial derivatives of the j -th term with respect to the l and l' for $l, l' = 1, \dots, L$.

We denote the following vectors and matrices, for $j = 1, \dots, J$, and $k = 1, \dots, n_j$,

$$\begin{aligned} \mathbf{s}_j &:= \begin{bmatrix} \vdots \\ \mathbf{s}_{jk} \\ \vdots \end{bmatrix}, \\ \eta_{jk} = \eta(\mathbf{s}_j; \mathbf{u}) &:= \begin{bmatrix} \vdots \\ \eta(\mathbf{s}_{jk}) \\ \vdots \end{bmatrix} = \mathbf{b}^{(j)} + \mathbf{A}^{(j)}\mathbf{u}, \\ \mathbf{J}^{(j)} &= \begin{bmatrix} \frac{\partial m_j}{\partial u_1} & \cdots & \frac{\partial m_j}{\partial u_L} \end{bmatrix}, \\ \mathbf{H}^{(j)} &= \begin{bmatrix} \frac{\partial^2 m_j}{\partial u_1^2} & \cdots & \frac{\partial^2 m_j}{\partial u_1 \partial u_L} \\ \vdots & \ddots & \vdots \\ \frac{\partial^2 m_j}{\partial u_L \partial u_1} & \cdots & \frac{\partial^2 m_j}{\partial u_L^2} \end{bmatrix}. \end{aligned}$$

Then for the j -th component of the first-order derivative, we denote $q_{jk} = w_{jk} \exp(\eta_{jk})$ and $\mathbf{A}_{kl}^{(j)} = \frac{\partial \eta_{jk}}{\partial u_l}$ and we have

$$\begin{aligned} \frac{\partial m_j}{\partial u_l} &= \frac{\sum_k w_{jk} \exp(\eta_{jk}) \frac{\partial \eta_{jk}}{\partial u_l}}{\sum_k w_{jk} \exp(\eta_{jk})} \\ &= \frac{\sum_k q_{jk} \frac{\partial \eta_{jk}}{\partial u_l}}{\sum_k q_{jk}} \\ &= \frac{\sum_k q_{jk} \mathbf{A}_{kl}^{(j)}}{\sum_k q_{jk}} < \infty \\ &= \frac{\mathbf{A}^{(j)\top} \mathbf{q}^{(j)}}{\mathbf{1}^\top \mathbf{q}^{(j)}}. \end{aligned}$$

Since the term $\mathbf{q}^{(j)}$ is bounded by definition given a stable integration scheme, thus the Jacobian term is bounded. For the second-order derivative, by the quotient rule $\frac{d}{dx} \frac{f}{g} = \frac{f'g - fg'}{g^2}$, and for some $l, l' = 1, \dots, L$, we have

$$\frac{\partial^2 m_j}{\partial u_l \partial u_{l'}} = \frac{(\sum_k q_{jk})(\sum_k q_{jk} \mathbf{A}_{kl}^{(j)} \mathbf{A}_{kl'}^{(j)}) - (\sum_k q_{jk} \mathbf{A}_{kl}^{(j)})(\sum_k q_{jk} \mathbf{A}_{kl'}^{(j)})}{(\sum_k q_{jk})^2} < \infty.$$

Hence, the matrix $\mathbf{J}^{(j)}$ is a ratio with nominator adjusted by the gradient of the linear predictor function at \mathbf{u} . $\mathbf{H}^{(j)}$ is the difference between the ratios. For $l, l' = 1, \dots, L$, $\frac{\partial m_j}{\partial u_l} < \infty$ and $\frac{\partial^2 m_j}{\partial u_l \partial u_{l'}} < \infty$ are bounded. To further simplify the notation, we denote

$$\begin{aligned}\mathbf{q}^{(j)} &= \mathbf{q}_{j\cdot}, \\ \widehat{\mathbf{q}}^{(j)} &:= \frac{\mathbf{q}^{(j)}}{\sum_k \mathbf{q}_{jk}}, \\ \mathbf{d}^{(j)} &= \text{diag}(\mathbf{q}^{(j)}), \\ \widehat{\mathbf{d}}^{(j)} &= \text{diag}\left(\frac{\mathbf{q}^{(j)}}{\sum_k \mathbf{q}_{jk}}\right).\end{aligned}$$

Then we can simplify the expressions into,

$$\begin{aligned}\mathbf{J}^{(j)} &= \mathbf{A}^{(j)\top} \widehat{\mathbf{q}}^{(j)} \\ \mathbf{H}^{(j)} &= \frac{(\mathbf{1}^\top \mathbf{q}^{(j)}) (\mathbf{A}^{(j)\top} \mathbf{d}^{(j)} \mathbf{A}^{(j)}) - (\mathbf{A}^{(j)\top} \mathbf{q}^{(j)}) (\mathbf{q}^{(j)\top} \mathbf{A}^{(j)})}{(\mathbf{1}^\top \mathbf{q}^{(j)})^2} \\ &= \mathbf{A}^{(j)\top} \widehat{\mathbf{d}}^{(j)} \mathbf{A}^{(j)} - \mathbf{A}^{(j)\top} \widehat{\mathbf{q}}^{(j)} \widehat{\mathbf{q}}^{(j)\top} \mathbf{A}^{(j)}.\end{aligned}$$

B.4 Aggregation Mapper

Here, we provide the implementation of the logarithmic sum, i.e. $\overline{m}_j(\cdot)$ approximation mentioned in Section 3.1. The two mapper functions, `bm_aggregate` and `bm_logsumexp`, in the `inlabru` package, construct mapper objects to compute the blockwise sum and logarithmic sum of exponential terms in equation (16). Here the blocks (`sf_obj` in the sample code below) are defined by Ω_j . By default, `n_block=NULL`, the maximum block index in the inputs is used, i.e. `nrow(sf_obj)`. Otherwise, `n_block` can be defined as the predetermined number of output blocks by users.

A shortcut tool for aggregating these latent state vectors \mathbf{u} to effect scalars $\overline{m}_j(\mathbf{u})$ for each `inlabru` latent model component in equation (16) are provided by the low level mapper

`bm_logsumexp`. This mapper aggregates elements of `exp(state)`, where `state` are components, with optional non-negative weighting, and then takes the `log()`, so it can be used

- for `rescale=FALSE` (default), $v_k = \log[\sum_{i \in I_k} w_k \exp(u_i)]$, and
- for `rescale=TRUE`, $v_k = \log[\sum_{i \in I_k} w_k \exp(u_i) / \sum_{i \in I_k} w_k]$.

The mapper `bm_logsumexp` relies on the input handling methods for

`bm_aggregate`, but also allows the weights to be supplied on a logarithmic scale as `log_weights`.

To avoid numerical overflow, it uses the common method of internally shifting the state block-wise via Ω_j with

```
(state-log_weights)[block] - max((state-log_weights)[block]),
```

and shifts the result back afterwards.

The reconstruction of the continuous covariate field described in Section 4.2 involves evaluating the aggregated field using a piecewise linear mesh via the `bm_aggregate(..., rescale = TRUE)` mapper. The option `rescale = TRUE` specifies that z_p is computed as the mean of the covariate field within the p -th polygon. A sample code snippet is provided below.

```
R> # sf_obj: the aggregated polygon sf object
R> # matern: the model defined by inla.spde2.pcmatern here
R> cmp <- ~ x(main = geometry, model = matern)
R> agg_mapper <- bm_aggregate(
+   rescale = TRUE,
+   n_block = NULL
+ )
R> fml <- ~ ibm_eval(agg_mapper,
+   input = list(
+     block = .block,
+     weights = weight
+   ),
```

```
+ state = x
+ )
```

In `inlabru` version 2.12.0.9021, the standard mapper class names were shortened from `bru_mapper_<type>` to `bm_<type>` for readability, with old objects automatically converted and legacy constructors redirected to the new ones.

B.5 Nonlinear Taylor Expansion

Here, we provide the derivation of a further Taylor expansion on a nonlinear predictor expression mentioned in Section 3.3. This is an extension from the linearisation case in Appendices B.2 and B.3. Let f be some known non-linear function and once differentiable,

$$\eta_{jk} = b^{(j)} + \mathbf{A}^{(j)} f(\mathbf{u}), \text{ and } \frac{\partial \eta_{jk}}{\partial u_l} = \mathbf{A}^{(j)} \frac{\partial f(\mathbf{u})}{\partial u_l} < \infty.$$

With first-order Taylor expansion, we have

$$f(\mathbf{u}) = f(\mathbf{u}_*) + \mathbf{J}(\mathbf{u}_*)^\top (\mathbf{u} - \mathbf{u}_*) + \mathcal{O}(\|\mathbf{u} - \mathbf{u}_*\|^2).$$

B.6 Linearisation Difference

Here, we provide the derivation of the difference between the continuous and discretised linearisation cases mentioned in Theorem 3.2.

By definition, $\exp(x) := \sum_{k=0}^{\infty} \frac{x^k}{k!} = 1 + x + \frac{x^2}{2} + \dots$, we ignore the higher-order terms that are more than or equal to cubic. Then we have the difference of the domain contribution terms between the continuous and discretised linearisation cases is

$$\begin{aligned} \log \frac{\tilde{\mathbb{P}}(\mathbf{y}|\mathbf{u}, \boldsymbol{\theta})}{\mathbb{P}(\mathbf{y}|\mathbf{u}, \boldsymbol{\theta})} &= \sum_j^J e^{\bar{m}_j} - \sum_j^J e^{m_j} \\ &= \sum_j^J (e^{\bar{m}_j} - e^{m_j}) \end{aligned}$$

$$\begin{aligned}
&= \sum_j^J e^{\bar{m}_j} (1 - e^{m_j - \bar{m}_j}) \\
&= \sum_j^J [e^{\bar{m}_j(\mathbf{u}_*) + \mathbf{J}_j(\mathbf{u}_*)^\top(\mathbf{u} - \mathbf{u}_*)}] \\
&\quad \cdot \left[1 - \exp \left\{ \frac{1}{2}(\mathbf{u} - \mathbf{u}_*)^\top \mathbf{H}^{(j)}(\mathbf{u} - \mathbf{u}_*) + \mathcal{O}(\|\mathbf{u} - \mathbf{u}_*\|^3) \right\} \right] \\
&= - \sum_j^J [e^{\bar{m}_j(\mathbf{u}_*) + \mathbf{J}_j(\mathbf{u}_*)^\top(\mathbf{u} - \mathbf{u}_*)}] \\
&\quad \cdot \left[\frac{1}{2}(\mathbf{u} - \mathbf{u}_*)^\top \mathbf{H}^{(j)}(\mathbf{u} - \mathbf{u}_*) + \mathcal{O}(\|\mathbf{u} - \mathbf{u}_*\|^3) \right] \\
&= - \sum_j^J [e^{\bar{m}_j(\mathbf{u}_*)} (1 + \mathbf{J}_j(\mathbf{u}_*)^\top(\mathbf{u} - \mathbf{u}_*) + \mathcal{O}(\|\mathbf{u} - \mathbf{u}_*\|^2))] \\
&\quad \cdot \left[\frac{1}{2}(\mathbf{u} - \mathbf{u}_*)^\top \mathbf{H}^{(j)}(\mathbf{u} - \mathbf{u}_*) + \mathcal{O}(\|\mathbf{u} - \mathbf{u}_*\|^3) \right] \\
&= - \sum_j^J e^{\bar{m}_j(\mathbf{u}_*)} \left[\frac{1}{2}(\mathbf{u} - \mathbf{u}_*)^\top \mathbf{H}^{(j)}(\mathbf{u} - \mathbf{u}_*) + \mathcal{O}(\|\mathbf{u} - \mathbf{u}_*\|^3) \right]
\end{aligned}$$

B.7 Expectation Difference

Here, we provide the derivation of the expectation difference between the continuous and discretised linearisation cases mentioned in Theorem 3.2. We denote $\boldsymbol{\mu}_\theta = \mathbb{E}(\mathbf{u}|\mathbf{y}, \boldsymbol{\theta})$ and $\mathbf{Q}_\theta^{-1} = \text{Var}(\mathbf{u}|\mathbf{y}, \boldsymbol{\theta}) = \mathbb{E}[(\mathbf{u} - \boldsymbol{\mu})(\mathbf{u} - \boldsymbol{\mu})^\top | \mathbf{y}]$.

$$\begin{aligned}
\mathbb{E}_{\mathbf{u} \sim \mathcal{N}(\boldsymbol{\mu}, \mathbf{Q}^{-1})} \left(\log \frac{\tilde{\mathbb{P}}(\mathbf{y}|\mathbf{u}, \boldsymbol{\theta})}{\mathbb{P}(\mathbf{y}|\mathbf{u}, \boldsymbol{\theta})} \right) &= \mathbb{E}_{\mathbf{u} \sim \mathcal{N}(\boldsymbol{\mu}, \mathbf{Q}^{-1})} \left(\sum_{j=1}^J e^{\bar{m}_j} - \sum_{j=1}^J e^{m_j} \right) \\
&= \mathbb{E} \left(- \sum_j^J e^{\bar{m}_j(\mathbf{u}_*)} \left[\frac{1}{2}(\mathbf{u} - \mathbf{u}_*)^\top \mathbf{H}^{(j)}(\mathbf{u} - \mathbf{u}_*) + \mathcal{O}(\|\mathbf{u} - \mathbf{u}_*\|^3) \right] \right) \\
&= -\frac{1}{2} \sum_j^J e^{\bar{m}_j(\mathbf{u}_*)} \mathbb{E}(\text{tr}[(\mathbf{u} - \mathbf{u}_*)^\top \mathbf{H}^{(j)}(\mathbf{u} - \mathbf{u}_*)]) \\
&\quad + \mathcal{O}(\mathbb{E}[\|\mathbf{u} - \mathbf{u}_*\|^3 | \mathbf{y}])
\end{aligned}$$

$$\begin{aligned}
&= -\frac{1}{2} \sum_j^J e^{\bar{m}_j(\mathbf{u}_*)} \\
&\quad \cdot \mathbb{E} \left(\text{tr} \left\{ \mathbf{H}^{(j)} [(\mathbf{u} - \boldsymbol{\mu}) + (\boldsymbol{\mu} - \mathbf{u}_*)] [(\mathbf{u} - \boldsymbol{\mu}) + (\boldsymbol{\mu} - \mathbf{u}_*)]^\top \right\} \right) \\
&\quad + \mathcal{O} \left(\mathbb{E} [\|\mathbf{u} - \mathbf{u}_*\|^3 | \mathbf{y}] \right) \\
&= -\frac{1}{2} \sum_j^J e^{\bar{m}_j(\mathbf{u}_*)} \left[\text{tr}(\mathbf{H}^{(j)} \mathbf{Q}^{-1}) + (\boldsymbol{\mu} - \mathbf{u}_*)^\top \mathbf{H}^{(j)} (\boldsymbol{\mu} - \mathbf{u}_*) \right] \\
&\quad + \mathcal{O} \left(\mathbb{E} [\|\mathbf{u} - \mathbf{u}_*\|^3 | \mathbf{y}] \right)
\end{aligned}$$

B.8 Kullback-Leibler (KL) Divergence

Here, we provide the derivation of the KL divergence between the continuous and discretised linearisation cases mentioned in Theorem 3.3. We follow the proof of Theorem 1 in Lindgren et al. (2024) and denote

$$\mathbf{G} = \sum_i J^{(i)}|_{\mathbf{u}_*} \mathbf{H}^{(i)}|_{\mathbf{u}_*} = - \sum_i e^{\bar{m}_i} \mathbf{H}^{(i)}. \quad (\text{B5})$$

We denote $\bar{\mathbf{m}}_\theta = \mathbb{E}_{\bar{p}}(\mathbf{u} | \mathbf{y}, \theta)$ and $\bar{\mathbf{Q}}_\theta^{-1} = \text{Cov}_{\bar{p}}(\mathbf{u}, \mathbf{u} | \mathbf{y}, \theta)$. Hence, the first term in the KL divergence is

$$\begin{aligned}
\mathbb{E}_{\bar{p}} [\log \tilde{p}(\mathbf{y} | \mathbf{u}, \theta) - \log \bar{p}(\mathbf{y} | \mathbf{u}, \theta)] &= \frac{1}{2} \text{tr}(\mathbf{G} \bar{\mathbf{Q}}_\theta^{-1}) + \frac{1}{2} (\bar{\mathbf{m}}_\theta - \mathbf{u}_*)^\top \mathbf{G} (\bar{\mathbf{m}}_\theta - \mathbf{u}_*) \\
&\quad + \mathcal{O} \left(\mathbb{E}_{\bar{p}} [\|\mathbf{u} - \mathbf{u}_*\|^3 | \mathbf{y}, \theta] \right). \quad (\text{B6})
\end{aligned}$$

Proof. The KL divergence for the first and second Taylor expansion can be expressed as

$$\text{KL} \left(\tilde{\mathbb{P}}(\mathbf{u} | \mathbf{y}, \theta) \parallel \bar{\mathbb{P}}(\mathbf{u} | \mathbf{y}, \theta) \right) = E_{\tilde{\mathbb{P}}} \left[\log \frac{\tilde{\mathbb{P}}(\mathbf{y} | \mathbf{u}, \theta)}{\bar{\mathbb{P}}(\mathbf{y} | \mathbf{u}, \theta)} \right] - \log \frac{\bar{\mathbb{P}}(\mathbf{y} | \theta)}{\tilde{\mathbb{P}}(\mathbf{y} | \theta)} \quad (\text{B7})$$

The details of the first term and corresponding derivation see Lindgren et al. (2024).

$$\mathbb{E}_{\tilde{p}} \left[\log \tilde{p}(\mathbf{y} | \mathbf{u}, \theta) - \log \bar{p}(\mathbf{y} | \mathbf{u}, \theta) \right] = -\frac{1}{2} \text{tr}(\mathbf{G} \bar{\mathbf{Q}}_\theta^{-1}) - \frac{1}{2} (\bar{\boldsymbol{\mu}}_\theta - \mathbf{u}_*)^\top \mathbf{G} (\bar{\boldsymbol{\mu}}_\theta - \mathbf{u}_*)$$

$$+ \mathcal{O}(\mathbb{E}_{\bar{p}}[\|\mathbf{u} - \mathbf{u}_*\|^3 | \mathbf{y}, \boldsymbol{\theta}])$$

The second term above can be expressed as

$$-\text{tr} \left[\left(\sum_j e^{\bar{m}_j(\mathbf{u}_*)} \mathbf{H}^{(j)} \right) (\mathbf{Q}_\theta + \sum_j e^{\bar{m}_j(\mathbf{u}_*)} \mathbf{H}^{(j)})^{-1} \right], \quad (\text{B8})$$

where \mathbf{Q}_θ is the Gaussian prior on the latent variable \mathbf{u} . □

B.9 Stable Integration Scheme

Here, we provide the technical details of a stable integration scheme mentioned in Sections 3.1 and 5.1. We present the stable integration scheme for \mathbb{R}^2 implemented in INLA and `inlabru` packages. There are alternative stable integration schemes to be implemented in the pipeline.

We refer to a stable integration scheme as a bounded estimate of the likelihood which is the combination of the domain and the observed contribution, as shown in equation (4), is bounded, i.e. $\ell(\lambda | \mathcal{Y}) < \infty$. The calculation of observed contribution is evaluated at the observed point which further details available in Simpson et al. (2016).

We denote a function on a triangulation of space $f(\cdot)$ with $t = 1, \dots, n_t$ and $v = 1, 2, 3$, as the indices of the triangular mesh and the vertex respectively and \mathcal{T}_t referring to the t -th element. We further define $f_{(t,v)} := f(s_{(t,v)})$ and $\sum_t \sum_{v \in \mathcal{T}_t} w_{(t,v)} = 1$, for some weights $\{w_{(t,v)}\}$, and some vertices $\{s_{(t,v)}\} \subset \Omega$ inside the sample space. The domain contribution can be approximated via integration points as,

$$\int_{\Omega} f(s) ds \approx \sum_t \sum_{v \in \mathcal{T}_t} w_{(t,v)} f_{(t,v)}; \quad (\text{B9})$$

A 3-column integer matrix with 1-based vertex indices for each triangle (t, v) (with reference to `mesh$loc`) is stored under `mesh$graph$tv` in the mesh object under the `fmeshr` package.

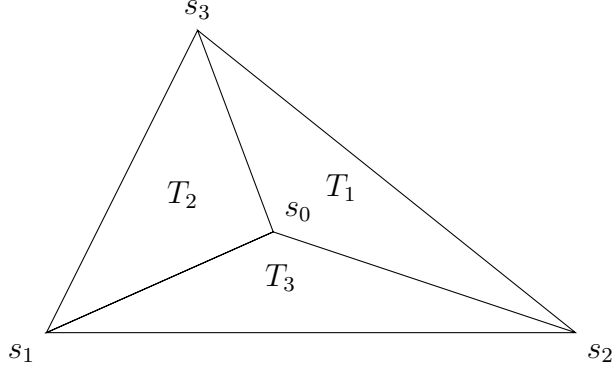


Figure 10: Barycentric coordinates of a triangle. The volume of T_v for $v = 1, 2, 3$ is $|T_{(t,v)}|$.

We illustrate with a single triangle, i.e. $t = 1$, as in Figure 10. We denote the volume of the triangle $|T_{(t,\cdot)}| = \sum_{v=1}^3 |T_{(t,v)}|$ where $|T_{(t,v)}|$ are the volume of the sub-triangles through barycentric subdivision. We assume a piecewise linear function within the triangle $\Delta_{s_1 s_2 s_3}$. The barycentre can be computed

$$s_{t_0} = \sum_{v=1}^3 w_{(t,v)} s_{(t,v)}; \quad w_{(t,v)} = \frac{|T_{(t,v)}|}{|T_{(t,\cdot)}|}, \quad (\text{B10})$$

where $w_{t,v}$ is known as the barycentric coordinates with respect to s_{t_0} . Since the triangle is piecewise linear, $w_{t,v} = \psi_{k(t,v)}(s_{t_0})$ specified in equation (6). The weighted sum of a function evaluated at these points is the integral of this function approximated by linear basis functions $\psi_{k(t,v)}$ as in equation (6). Hence, the function evaluated at the barycentre

$$f(s_{t_0}) = \sum_{v=1}^3 w_{(t,v)} f_{(t,v)}. \quad (\text{B11})$$

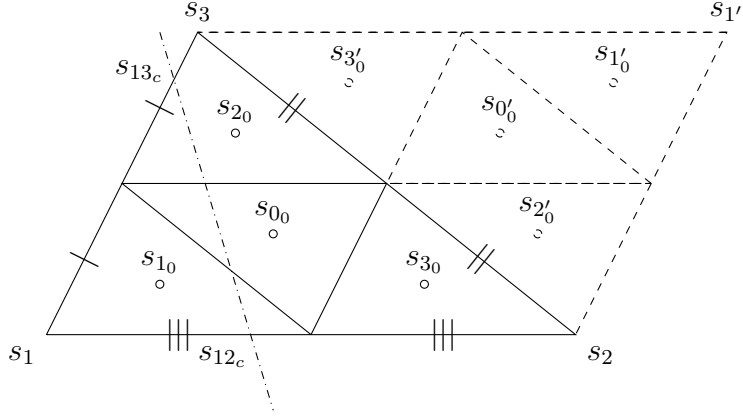


Figure 11: Illustration of integration points with mirror triangle and mid-edge subdivision. Circle: integration points; Points above the diagonal (s_2s_3) should be reflected into the lower triangle. Solid line: triangular mesh; Dashed line: mirror image; Dashdotted line: cut.

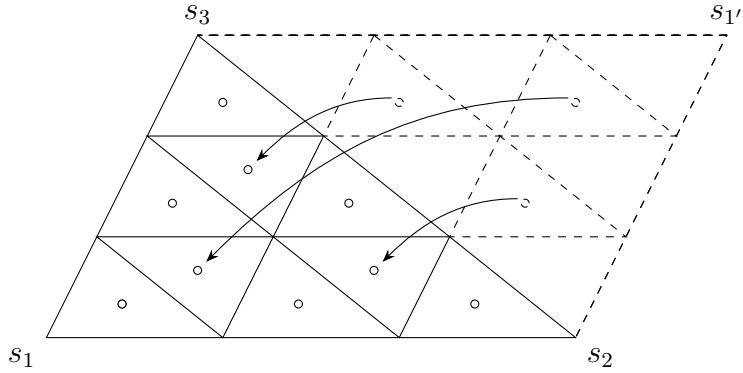


Figure 12: Illustration of integration points with mirror triangle and mid-edge subdivision. Circle: integration points; Solid line: triangular mesh; Dashed line: mirror image

We mirror the triangular element to create a parallelogram and distribute integration points s_{i_0} for $i = 1, \dots, n$ over the parallelogram in Figure 11 and halve the integration in the end. Generally speaking, the more integration points are, the more accurate the approximation is. It is an implementation trick to avoid considering whether the integration points are inside or outside the triangle. The integration points are the barycentres of the sub-triangles generated via mid-edge subdivision. Let $w_{(t_i,v)}$ be the barycentric weight with respect to the v -th vertex of the i -th sub-triangle in the t -th triangle and $s_{t_{i_0}}$ be the barycentre of the sub-triangle. The integral of the function for the triangle can be approximated as

$$\begin{aligned}
\int_{|T(t,\cdot)|} f(s_{t_0}) ds &\approx \frac{|T(t,\cdot)|}{n} \sum_{i=1}^n f(s_{t_{i_0}}) \\
&= \frac{|T(t,\cdot)|}{n} \sum_{i=1}^n \sum_{v=1}^3 f(t_{i,v}) w_{(t_i,v)} \\
&= \sum_{v=1}^3 f(t,v) \underbrace{\frac{|T(t,\cdot)|}{n} \sum_{i=1}^n w_{(t_i,v)}}_{:=w_{(t,v)}}
\end{aligned} \tag{B12}$$

In the scenario of removing a part of the integration via triangle dissection, say due to out of the boundary $\partial\Omega$, we simply set the weights to zero. For instance, the line segment $s_{13_c}s_{12_c}$ cuts through the mesh, thus $\Delta_{s_1s_{13_c}s_{12_c}}$ is removed and the weight of s_{1_0} set to zero in Figure 11. Refer to Hjelle and Dæhlen (2006) for further details of the algorithm.

If we consider the function $f(\cdot)$ to be nonlinear, we can improve the approximation by subdividing each mesh through the mid-edge subdivision thus with more integration points, each with less weight (via `fmesher::fm_subdivide` function, see Figure 13). When the sub-triangles are sufficiently fine in scale, we can assume piecewise linear sub-triangles and approximate the integral. Gaussian quadrature rule is considered as well but reweighing integration points on the corners complicates the rule when there is a cut.

A sample code of the `bm_logsumexp` mapper is shown below.

```

R> logsumexp_mapper <- bm_logsumexp(
+   rescale = FALSE,
+   n_block = nrow(sf_object)
+ )
R> formula <- ~ ibm_eval(logsumexp_mapper,
+   input = list(block = .block, weights = weight),
+   state = state
+ )

```

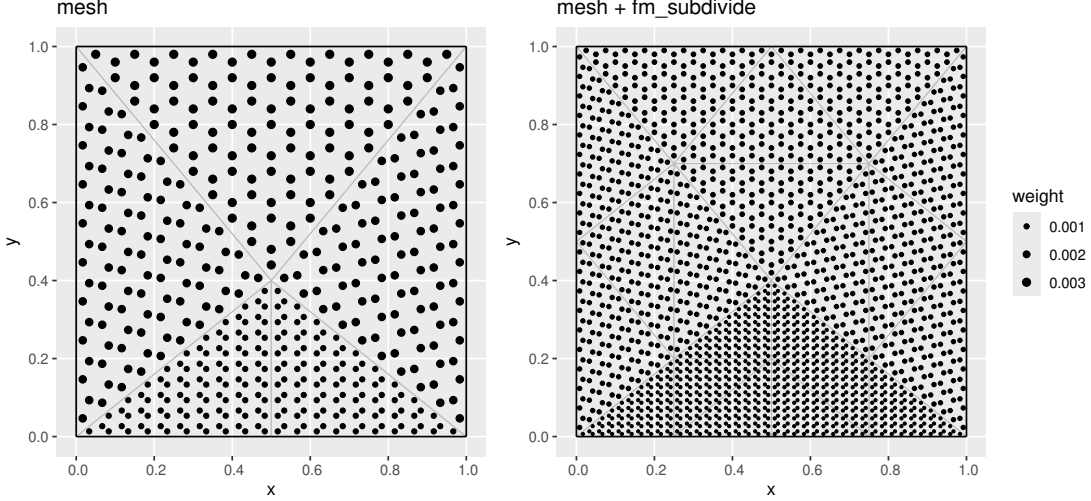


Figure 13: An example of integration points weights given a triangulation over a unit square

B.10 Degree of Freedom (DoF)

Here, we provide the technical details of the degree of freedom (Dof) mentioned in Section 3.1.1. We use the notations from Section B.9. The DoF is a measure of the flexibility of a function space. We simplify and rewrite equation (6) as

$$\log \lambda(\mathbf{s}) = \eta(\mathbf{s}) := u(\mathbf{s}) = \sum_{k=1}^K \psi_k(\mathbf{s}) u_k, \quad (\text{B13})$$

for some weight u_k . Given the volume of the bounded domain $|\Omega|$ is fixed, we only consider the latter two terms in equation (4), and combining with equation (B9),

$$-\int_{\Omega} \lambda(\mathbf{s}) d\mathbf{s} + \sum_{i=1}^n \log \lambda(y_i) \approx -\sum_t \sum_{v \in \mathcal{T}_t} w_{(t,v)} \lambda_{(t,v)} + \sum_{i=1}^n \sum_{k=1}^K u_k \psi_k(y_i), \quad (\text{B14})$$

where $\{u_1, \dots, u_k\}$ is defined in equation (6). We can see observations are pulling the likelihood upwards, hence the locations of the integration points are crucial to bound the estimation of the likelihood.

By placing the integration points at proper locations in the domain space, we can bound the likelihood specified in equations (4) and (5). We now illustrate how the construction in equation

(B12) is crucial to obtain stable estimation for the numerical integration of the likelihood function.

We illustrate unstable and stable integration schemes using a one-dimensional mesh on the range $[0, 1]$ (see Figure 14). For the unstable scheme, a single integration point is placed at $x = 0.5$, whereas the stable scheme uses two points at $x = 0$ and $x = 1$. In both cases, there is one observation point (indicated by the red arrow in the figure, which pulls the log-likelihood upwards). As shown in Figure 14(left), the single-point integration scheme results in unbounded integration. Since we put the integration point at the end points, we can stabilise the integration. This one dimensional mesh example translates to the integration points in triangular mesh formulation. The message that we want to convey here is with `fmesher::fm_subdivide` which subdivides an existing mesh, we can improve the approximation of likelihood by placing the more integration points evaluated at more locations.

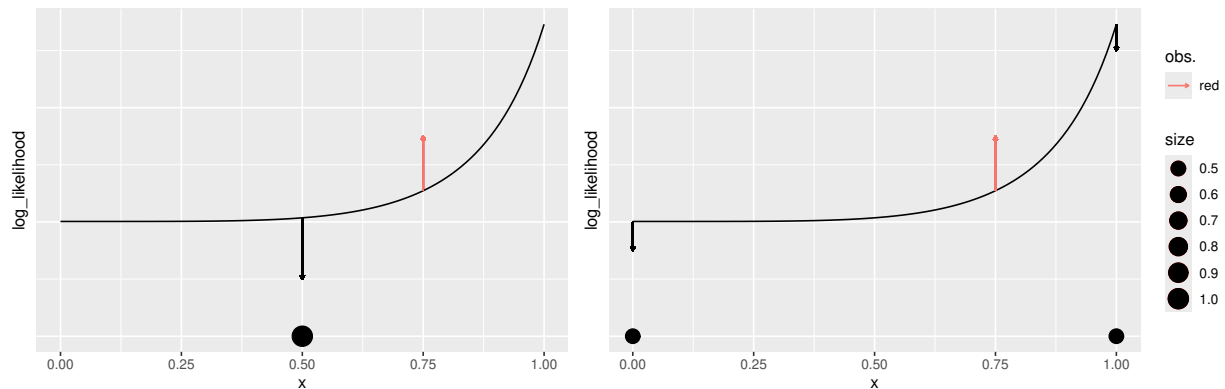


Figure 14: Unstable integration point (left) and stable integration point (right) with respect to log-likelihood for a single observation point (red). Arrow: observed contribution (red), domain contribution (black).

C Simulation

Here, we provide the implementation details and plots of the simulation study mentioned in Sections 3, 4 and 5.

C.1 Implementation Details of `fmesher::fm_extensions`

Here, we provide the implementation details of the function `fmesher::fm_extensions` mentioned in Section 5.1. The function `fmesher::fm_extensions` constructs inner and outer boundaries of a mesh. internally calls `fmesher::fm_nonconvex_hull` to create nonconvex hull over the domain.

```
R> # d1, d2: some distances from the boundary
R> mesh <- fm_mesh_2d_inla(...,
+   boundary = fm_extensions(
+     bnd,
+     c(d1, d2)
+   )
+ )
```

For this reason, the covariate field is simulated over the mesh domain for the purpose of easy handling. In real application, we might not have data at the buffered region that `inlabru::bru_fill_missing` can help fill missing data with nearest neighbour values.

C.2 Sampling from an Inhomogeneous Poisson Process

Here, we provide the implementation details of the function `inlabru::sample.lgcp` mentioned in Section 5.1. The function `inlabru::sample.lgcp` is a function for sampling from an inhomogeneous Poisson process. The log intensity has to be provided via its values at the vertices of the mesh elements. In between mesh nodes the log intensity is assumed to be linear. The function is called as follows:

```
R> # mesh: An INLA::inla.mesh object
R> # loglambda: A vector of log intensities at the mesh vertices
R> # samplers: A sf or inla.mesh object where simulated points
```

```
R> # that fall outside these polygons are discarded.
R> sample.lgcp(mesh, loglambda, samplers)
```

The algorithm is based on rejection sampling. The maximum of the `loglambda`, denoted by `wmax`, is input to simulate a Poisson random variable based on the product of the areas of the mesh elements and the maximal for each mesh element. If this random variable is larger than zero, another uniform random variable is simulated based on this Poisson random variable. The point(s) is only accepted with a probability that the uniform random variable is smaller than $\exp(\loglambda - wmax)$. This is repeated for all mesh elements within the `samplers`.

C.3 Simulated Point Pattern

Here, we provide the plots of the simulated point patterns mentioned in Section 5.1. The point pattern observations over Nepal are simulated via `sample.lgcp` (see Appendix C.2) according to equation (1) with the linear predictor $\eta(\mathbf{s}) = \beta_0 + \beta_x x(\mathbf{s}) + u(\mathbf{s})$, where $x(\mathbf{s})$ is a continuous covariate field formulated as $(s_1^2 - s_2^2) \exp[-\frac{1}{2}(s_1^2 + s_2^2)]$; $s_1 \in [-4, 4]$, $s_2 \in [-2, 2]$ projected to Nepal, and $u(\mathbf{s})$ is defined in equation (6). We set $\beta_0 = -7$, $\beta_x = -6$ and $u(\mathbf{s})$ with $\rho = 50$ and $\sigma = 0.5$. The nonlinear transformation of the covariate field is via a nonlinear function $f(\cdot)$, i.e. $\log \check{\lambda}(\cdot) := \check{\eta}(\cdot) = \beta_0 + \beta_x f[x(\cdot)] + u(\cdot)$. We construct $f(\cdot)$ as a nonlinear function, $f[x(\cdot)] = b^{-1} \exp[ax(\cdot)] - c$, where we set $a = 3$, $b = 9$ and $c = 3$.

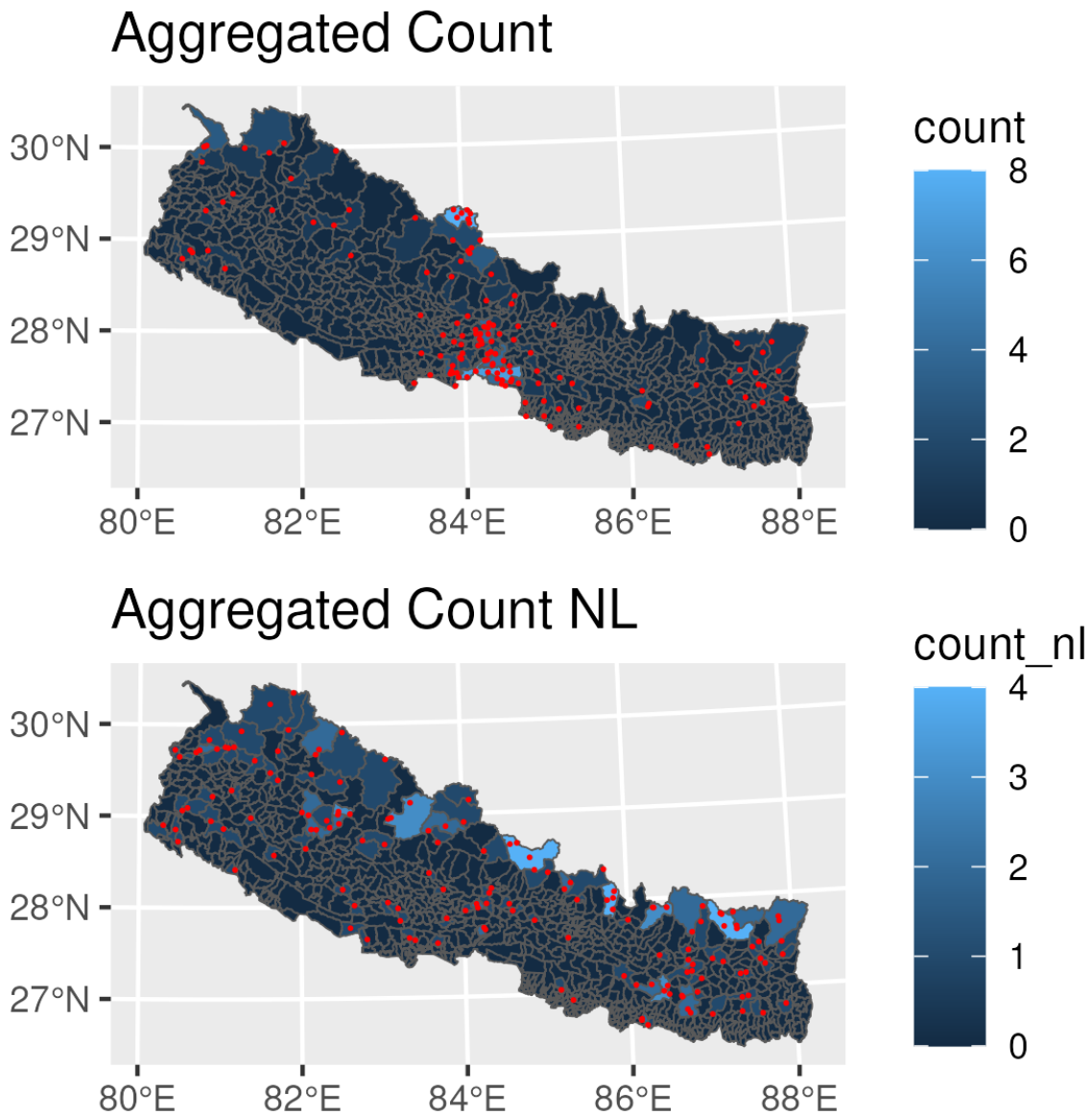


Figure 15: Simulated point pattern (red dots) and aggregated count observations from covariate field (top) and covariate field after nonlinear transformation (bottom). The underlying intensity field of the top panel follows equation (25) in the main text while the bottom follows equation in the main text.

C.4 Sampled Covariate Points

Here, we illustrate the plot of Incomplete covariate field for Point Values (PointVal) mentioned in Section 5.2.2. We sample one point from each administrative district and evaluate the covariate

field at that point.

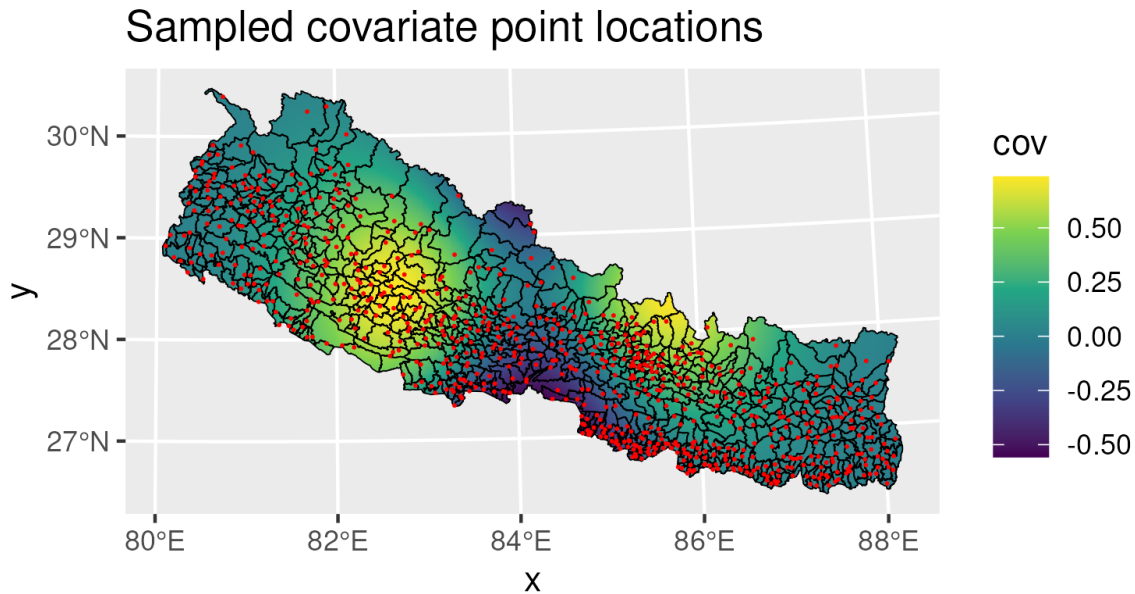


Figure 16: Sampled covariate points (red dots) with the covariate field.

C.5 PC Priors

Here, we provide the implementation code for the Penalised Complexity (PC) priors mentioned in Sections 4. The PC priors are implemented in the

`INLA::inla.spde2.pcmatern` function. The PC priors are used to set the range and standard deviation of the Matérn covariance function, following equation (11).

In Sections 4.1 and 4.2, the PC priors for *mesh (i)* are set to be $\mathbb{P}(\rho < 4) = 0.1$ and $\mathbb{P}(\sigma > 2) = 0.1$.

In Section 4.4, the PC priors for *mesh (ii)* are set to be $\mathbb{P}(\rho < 8) = 0.1$ and $\mathbb{P}(\sigma > 2) = 0.1$.

The PC priors are implemented for *mesh (i)* as follows:

```
R> # mesh_fm: fm_mesh_2d object; mesh (i) in Sec 5
R> INLA::inla.spde2.pcmatern(mesh_fm,
+   prior.range = c(4, 0.1),
+   prior.sigma = c(2, 0.1))
```

```
+ )
```

C.6 Rasterisation and Meshing

Here, we provide the implementation details of the rasterisation of covariate field and meshing, mentioned in Sections 3.2.2 and 5.1. The R scripts of full implementation are `mesh.R` and `covariate_rast.R` on <https://github.com/enoch26/misalignedata>. We illustrate the outline of the code below.

```
R> # INPUT
R> # df: data.frame of covariate field with x, y, and
R> #     covariate values columns
R> # bnd: sf object of boundary
R> # OUTPUT
R> # nepal_rast: SpatRaster object of covariate field;
R> #             RastFull in Sec 5
R> # nepal_rast_agg: SpatRaster object of aggregated (10x)
R> #             covariate field; RastAgg in Sec 5
R>
R> nepal_rast <- terra::rast(df,
+   type = "xyz",
+   crs = fm_crs(bnd)
+ )
R>
R> nepal_rast_agg <- terra::aggregate(nepal_rast,
+   fact = 10, fun = mean,
+   na.rm = TRUE
+ )
R>
```

```

R> # INPUT
R> # lattice: sf object of lattice points for mesh (i);
R> #           the resolution of the lattice points has taken
R> #           the resolution of nepal_rast into consideration;
R> #           see comparison of mesh and raster in Table 1
R> # lattice2: sf object of lattice points for mesh (ii);
R> #           1.961 times apart from lattice in terms of
R> #           edge_len
R> # edge_len(2): numeric; edge length of the mesh (i)/(ii) element
R> # bnd_out: sf object of outer boundary extension
R> # OUTPUT
R> # mesh_fm: fm_mesh_2d object; mesh (i) in Sec 5
R> # mesh_fmc: fm_mesh_2d object; mesh (ii) in Sec 5
R>
R> mesh_fm <- fm_mesh_2d_inla(
+   loc = lattice,
+   max.edge = c(
+     1.1 * edge_len, # 1.1* to avoid interfering with the lattice
+     5 * edge_len
+   ),
+   boundary = fm_extensions(bnd, bnd_out),
+   crs = fm_crs(bnd)
+ )
R>
R> mesh_fmc <- fm_mesh_2d_inla(
+   loc = lattice2,
+   max.edge = c(

```

```

+     1.1 * edge_len2, # 1.1* to avoid interfering with the lattice
+     5 * edge_len2
+   ),
+   boundary = fm_extensions(bnd, bnd_out),
+   crs = fm_crs(bnd)
+ )

```

C.7 Precision Matrix (**CMatrix**)

Here we illustrate how to convert upper triangular storage precision matrix U_{ϵ_x} generated from INLA into the full symmetric matrix \hat{Q}_{ϵ_x} mentioned in Sections 4.4 and 7.1.

$$\begin{aligned} \text{adiag}(\hat{Q}_{\epsilon_x}) &= \text{adiag}(U_{\epsilon_x} + U_{\epsilon_x}^\top) \\ \text{diag}(\hat{Q}_{\epsilon_x}) &= \text{diag}(U_{\epsilon_x}), \end{aligned}$$

where `adiag` denotes the anti-diagonal matrix. The implementation code for fitting Type 0 generic model and making the full symmetric precision matrix is shown below.

```

R> # fit: a INLA/inlabru::bru object
R> # cmp: inlabru model component object
R> # make_sym function to make the precision matrix symmetric
R> make_sym <- function(Q) {
+   d <- diag(Q)
+   Q <- (Q + t(Q))
+   diag(Q) <- d
+   return(Q)
+ }
R> Q_hat <- make_sym(fit$misc$configs$config[[1]]$Q)
R> cmp <- ~ covariate(geometry,

```

```
+ mapper = bru_get_mapper(matern),
+ model = "generic0", Cmatrix = Q_hat
+ )
```

Type 0 generic model implements a precision matrix $Q = \tau \hat{Q}_{\epsilon_x}$ as in equation 24, where τ is a precision parameter.

We did not explore different priors for the precision matrix in this paper. However, different initial values can be set to explore the effect of the priors on the estimation.

C.7.1 Creating a Mesh for Prediction `fm_pixels`

In Section 5.2, we precompute the point locations for rasterised mesh elements at the outset. Details are provided in the GitHub repository (see Section E). Here, we present an alternative method to create a rasterised mesh for prediction mentioned in Section 5.2. The function `fmesher::fm_pixels` can generate lattice locations from a rasterised mesh for prediction. A sample code is shown below.

```
R> # mesh: the mesh object
R> # dims: the dimensions of the raster
R> # mask: the boundary sf object
R> fm_pixels(mesh,
+   dims = rep(250, 2),
+   mask = bnd_buff, format = "sf"
+ )
```

C.8 One- and Two-stage Uncertainty Quantification

Here, we illustrate the analytical and computational approaches for accessing the stability of the model mentioned in Section 5.3.

C.8.1 Analytical Approach for Uncertainty Quantification

Here, we try to find a closed form solution for the derivatives of the density with respect to the coefficient and the uncertainty term.

$$\begin{aligned}
\frac{\partial \log p(\theta|x)}{\partial \epsilon_{x_j}} &= \sum_j (-e^{\eta_j} + y_j)(\beta_x) - \frac{\epsilon_{x_j}}{\sigma_{x_j|z_p}^2} = 0 \\
\frac{\partial^2 \log p(\theta|x)}{\partial \epsilon_{x_j}^2} &= \sum_j -e^{\eta_j} \beta_x^2 - \frac{1}{\sigma_{x_j|z_p}^2} < 0 \\
\frac{\partial \log p(\theta|x)}{\partial \beta_x} &= \sum_i (-e^{\eta_i} + y_i)(\hat{x}_i + \epsilon_{x_i}) = 0 \\
\frac{\partial^2 \log p(\theta|x)}{\partial \beta_x^2} &= \sum_i (-e^{\eta_i})(\hat{x}_i + \epsilon_{x_i})^2 \leq 0 \\
&\Rightarrow \sum_i \frac{\epsilon_{x_i}(\hat{x}_i + \epsilon_{x_i})}{\beta_x \sigma_{x_i|z_i}^2} = 0 \\
&\Rightarrow \sum_i \frac{(\hat{x}_i \epsilon_{x_i} + \epsilon_{x_i}^2)}{\sigma_{x_i|z_i}^2} = 0 \\
&\Rightarrow \sum_i \left(\frac{\hat{x}_i + 2\epsilon_{x_i}}{2\sigma_{x_i|z_i}} \right)^2 = \sum_i \left(\frac{\hat{x}_i}{2\sigma_{x_i|z_i}} \right)^2
\end{aligned}$$

Hence, we cannot derive a closed form solution for the derivatives.

C.8.2 Profile Likelihood for Uncertainty Quantification

Since we cannot derive a closed form solution, we seek to optimise the profile likelihood for the coefficient. Here, we illustrate one dimensional toy example for JU, VP and UP methods. We use the profile likelihood to optimise β_x with $n_z \in \{2, 4, 8, 16, 32, 64, 128, 256\}$, $\arg \max_{\beta_x} (\arg \max_{(\beta_0, \epsilon_x)}(\mathbf{p}))$ as in equation (27) in Section 5.3. In Figures 17 and 18, there are only one global maximum for JU and VP methods. However, in Figure 19, there is another one local maximum for β_x approaching infinity for UP method. This shows that one should be careful about the initial starting points when using the UP method. Nonetheless, we did not encounter optimisation issues in the simulation.

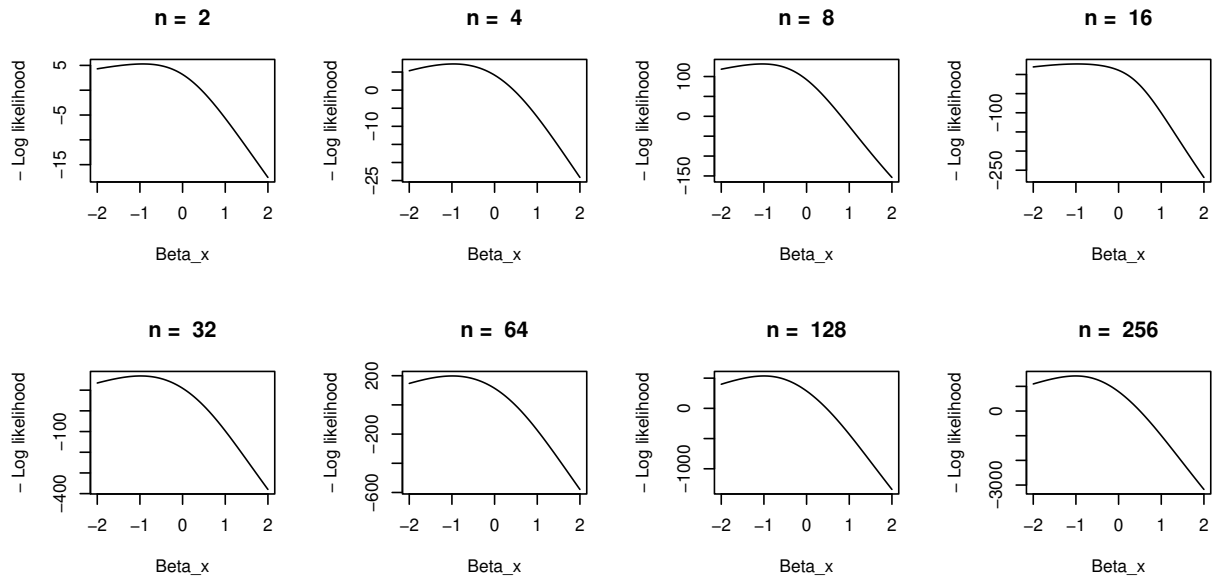


Figure 17: Profile likelihood optimisation of β_x for single-stage Joint Uncertainty (JU) approach.

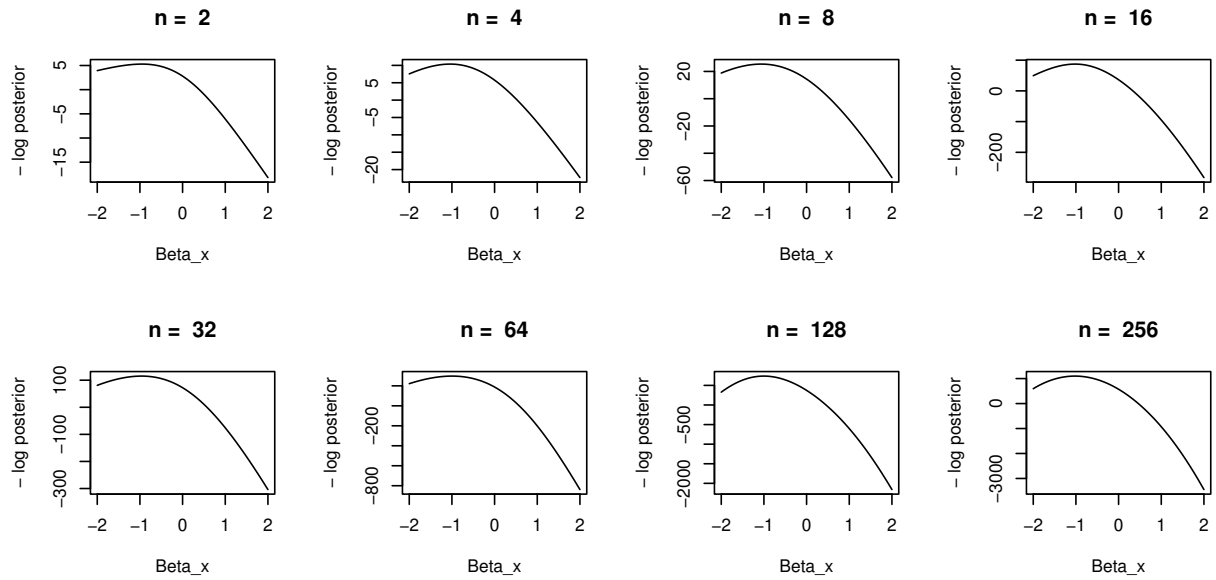


Figure 18: Profile likelihood optimisation of β_x for two-stage Value Plugin (VP) approach.

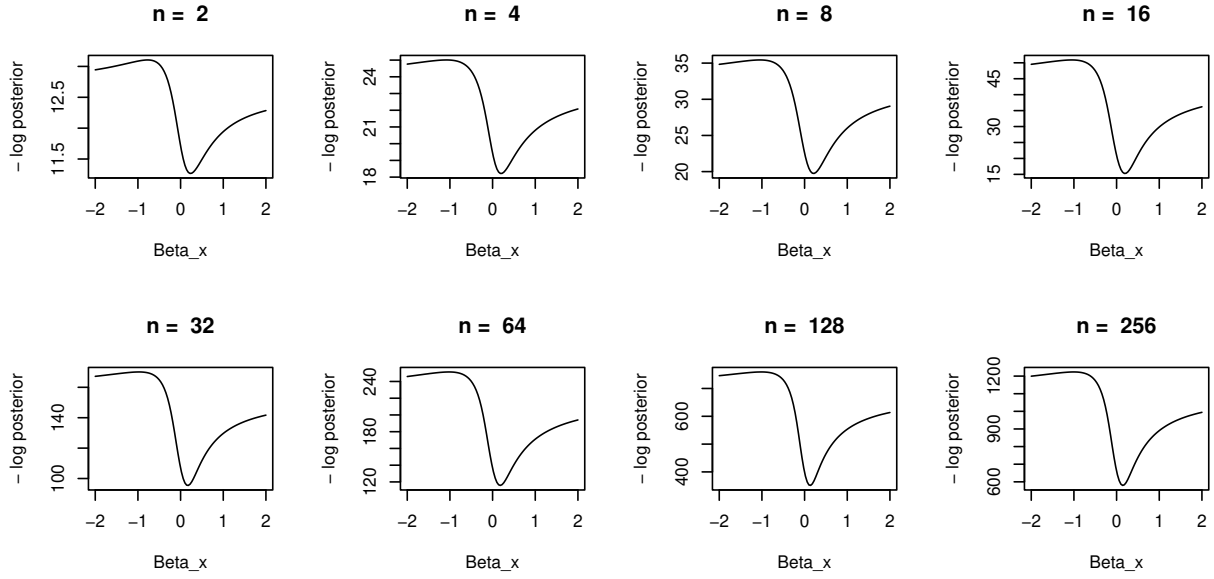


Figure 19: Profile likelihood optimisation of β_x for two-stage Uncertainty Plugin (UP) approach.

C.9 Covariate Estimation under Incomplete Covariate Field Scenario

The table and plots refer to Section 6.2.

Cov.	Obs.	Method	MSE	MDS	$\bar{X}(\cdot)$
PolyAgg	$\mathcal{Y}, \check{\mathcal{Y}}, \mathcal{N}, \check{\mathcal{N}}$	VP and UP	7.915×10^{-6}	-1.115×10^1	0.18262
	\mathcal{Y}	JU	7.571×10^{-6}	-1.116×10^1	
	\mathcal{N}		7.575×10^{-6}	-1.116×10^1	
	$\check{\mathcal{Y}}$		7.562×10^{-6}	-1.116×10^1	
	$\check{\mathcal{N}}$		7.513×10^{-6}	-1.116×10^1	
PointVal	$\mathcal{Y}, \check{\mathcal{Y}}, \mathcal{N}, \check{\mathcal{N}}$	VP and UP	1.309×10^{-3}	-5.842	
	\mathcal{Y}	JU	1.116×10^{-3}	-5.908	
	\mathcal{N}		1.163×10^{-3}	-5.891	
	$\check{\mathcal{Y}}$		1.247×10^{-3}	-5.861	
	$\check{\mathcal{N}}$		1.196×10^{-3}	-5.883	

Table 4: Table of the Mean Squared Error (MSE) and Mean Dawid-Sebastiani (MDS) scores for the covariate field x across the models under incomplete covariate field scenario. PointVal: Point Values, PolyAgg: Polygon Aggregation, $\bar{X}(\cdot)$: Mean of Covariate field.

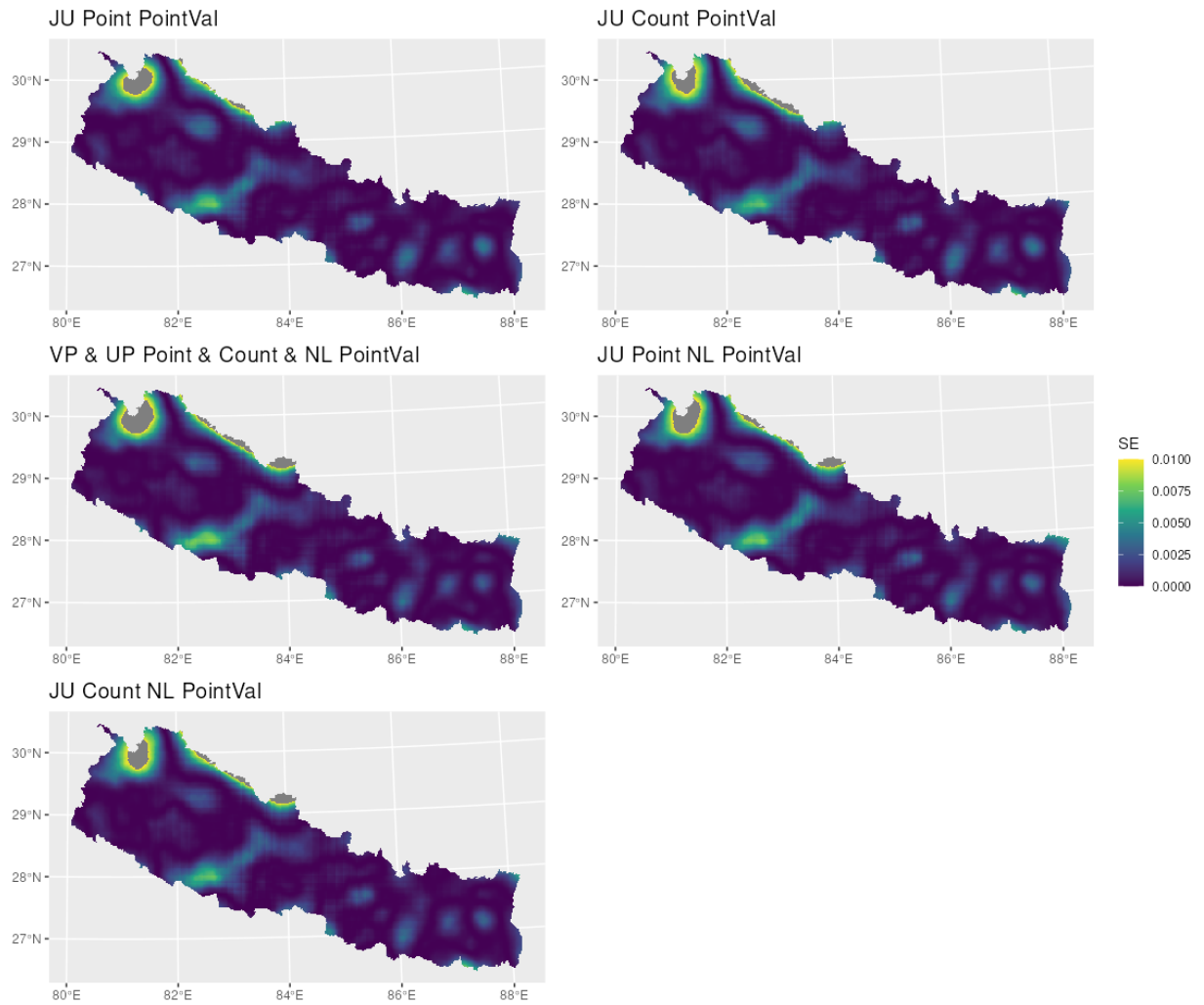


Figure 20: Squared Error (SE) for the covariate field X across the models under incomplete covariate field scenario with observed noises σ_{ϵ_x} (truncated at 0.01). JU: Joint Uncertainty, VP: Value Plugin, UP: Uncertainty Plugin, Point: Observed Point, Count: Aggregated Count, PointVal: Point Values. $\bar{X}(\cdot) = 0.18262$

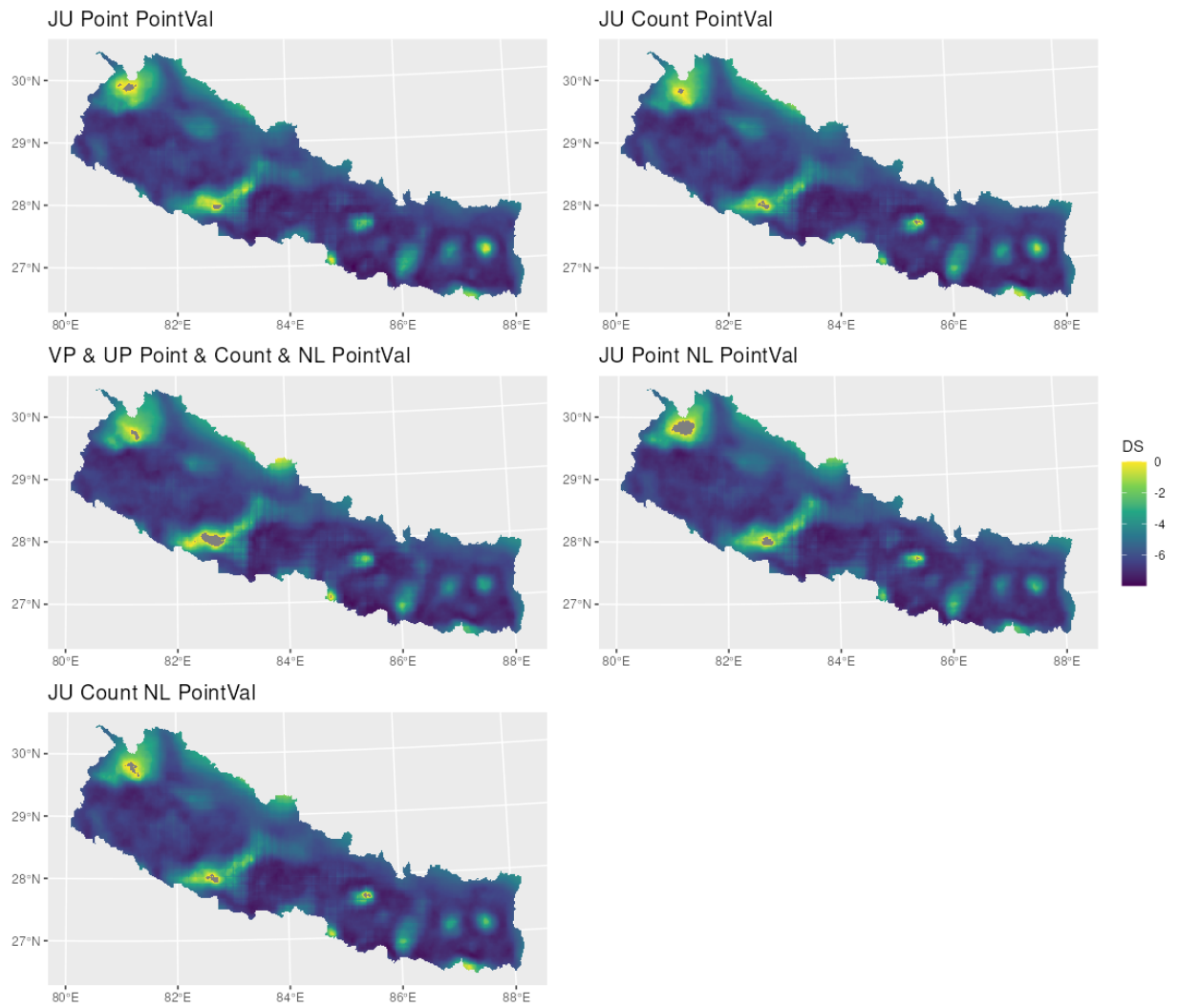


Figure 21: Dawid-Sebastiani (DS) score for the covariate field X across the models under incomplete covariate field scenario with observed noises σ_{ϵ_x} (truncated at 0). JU: Joint Uncertainty, VP: Value Plugin, UP: Uncertainty Plugin, Point: Observed Point, Count: Aggregated Count, PointVal: Point Values.

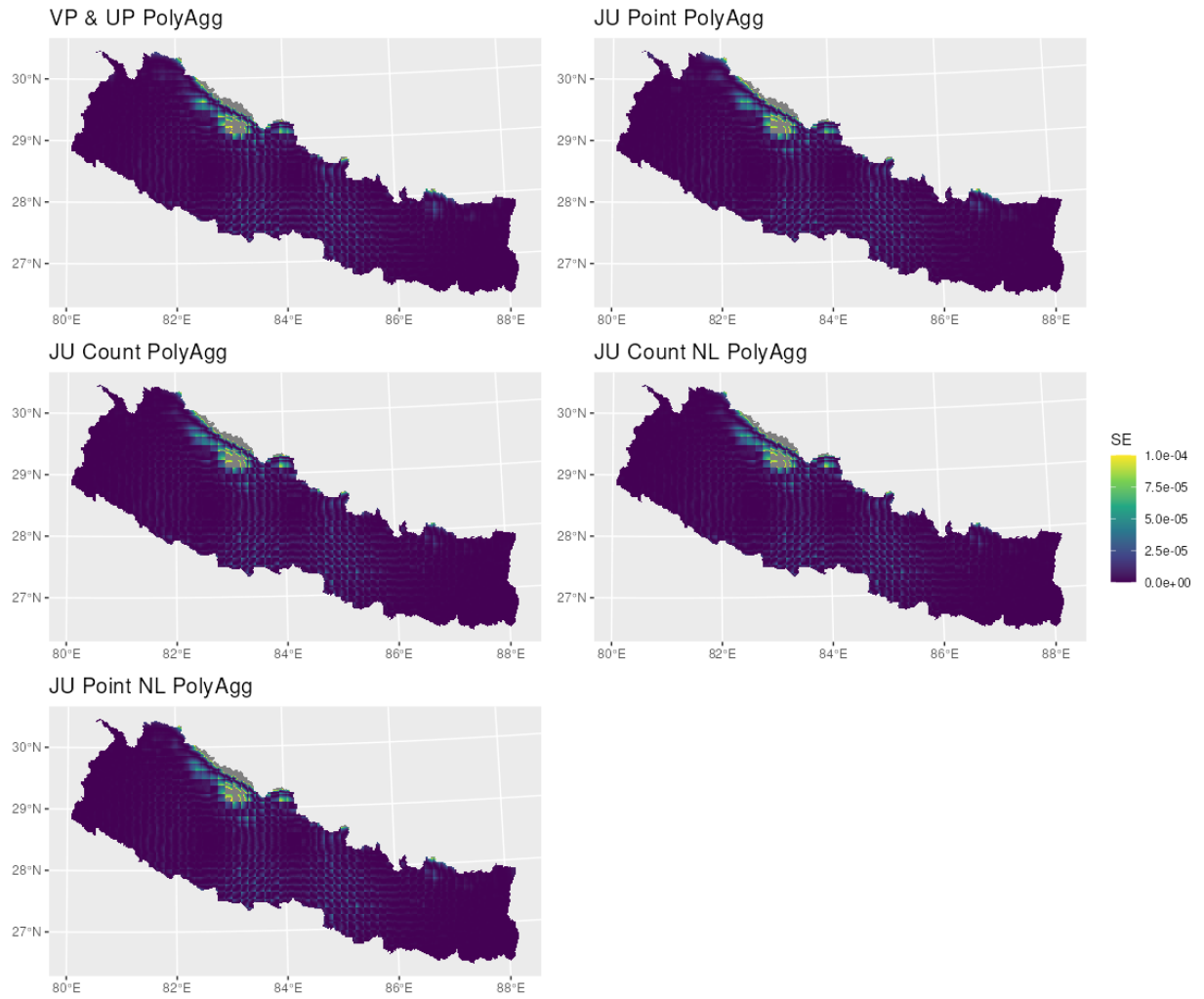


Figure 22: Squared Error (SE) for the covariate field X across the models under incomplete covariate field scenario with observed noises σ_{ϵ_x} (truncated at 1×10^{-4}). JU: Joint Uncertainty, VP: Value Plugin, UP: Uncertainty Plugin, Point: Observed Point, Count: Aggregated Count, PolyAgg: Polygon Aggregation. $\bar{X}(\cdot) = 0.18262$

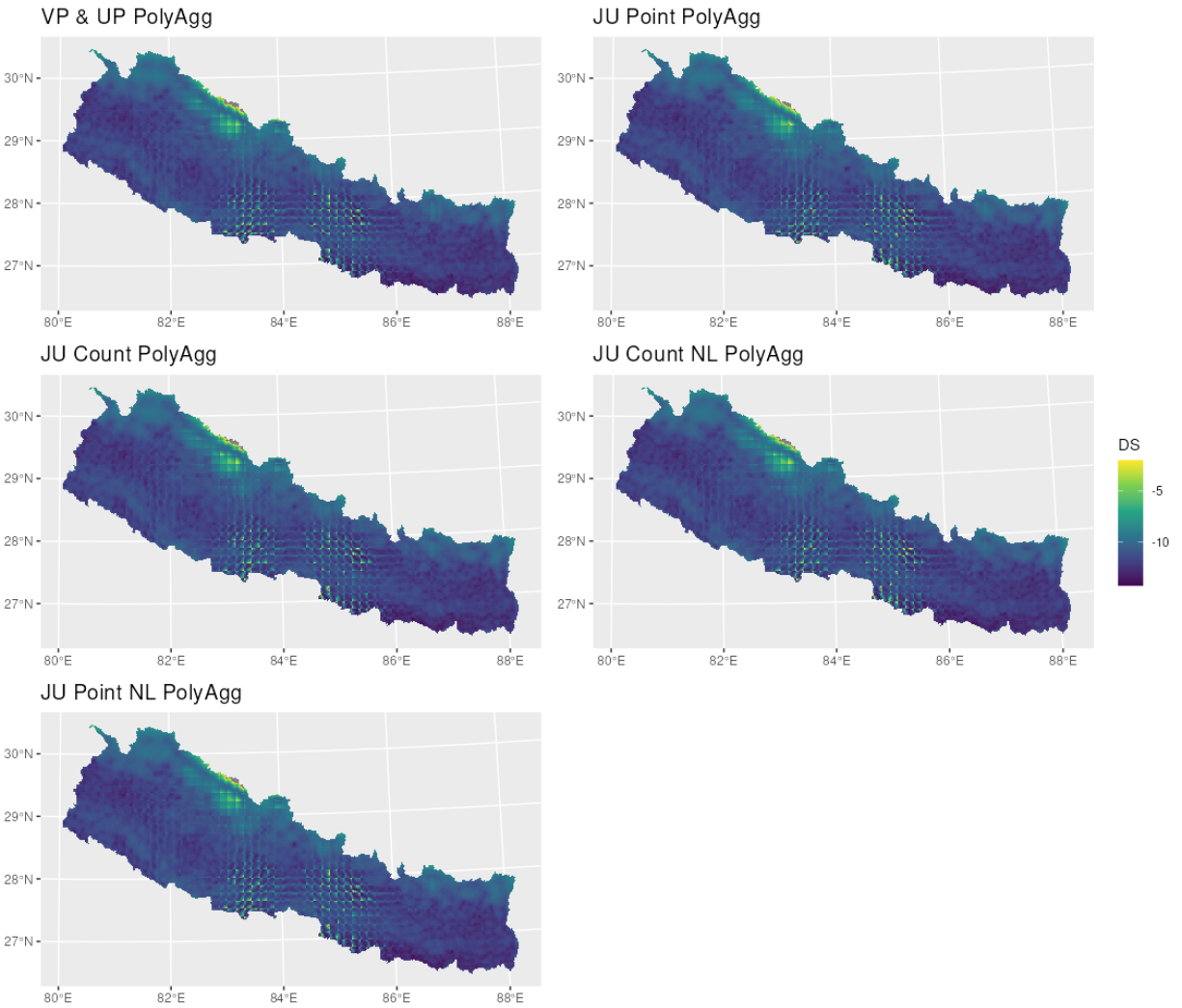


Figure 23: Dawid-Sebastiani (DS) score for the covariate field X across the models under incomplete covariate field scenario with observed noises σ_{ϵ_x} (truncated at 0). JU: Joint Uncertainty, VP: Value Plugin, UP: Uncertainty Plugin, Point: Observed Point, Count: Aggregated Count, PolyAgg: Polygon Aggregation.

C.10 Computation Time

Here refers to Sections 4.3 and 4.4 to compare the computation time across different models.

All numerical experiments for the case study/simulation were performed limited to 10 threads

on a Four Intel Xeon E5-2680 v3 2.5GHz, 30M Cache, 9.6 GT/s QPI 192 GB RAM machine (i.e. 48 cores in total and 2 threads each core).

Model name	Description	Time (sec)
fit_pts	Point RastFull	413.67
fit_pts_agg	Point RastAgg	387.74
fit_pts_poly	Point PolyAgg	412.79
fit_count	Count RastFull	1223.40
fit_agg	Count RastAgg	1327.17
fitly	Count PolyAgg	1383.79
fit_icov_sd01	VP and UP point+count NL PointVal	474.51
fit_ap	VP and UP PolyAgg	973.82
fit_ic_pts_sd01	JU Point PointVal	5373.32
fit_ic_sd01	JU Count PointVal	6549.09
fit_ic_ap_pts	JU Point PolyAgg	10479.75
fit_ic_ap	JU Count PolyAgg	13643.07
fit_ic_pts_sd01_nl	JU Point NL PointVal	4822.12
fit_ic_sd01_nl	JU Count NL PointVal	4950.74
fit_ic_ap_pts_nl	JU Point NL PolyAgg	5374.53
fit_ic_ap_nl	JU Count NL PolyAgg	8100.82
fit_icov2_pts_sd01	VP Point PointVal	335.58
fit_icov2_sd01	VP Count PointVal	475.57
fit_icov2_ap_pts	VP Point PolyAgg	421.68
fit_icov2_ap	VP Count PolyAgg	487.53
fit_icov2_pts_nl_sd01	VP Point NL PointVal	308.22
fit_icov2_nl_sd01	VP Count NL PointVal	609.28
fit_icov2_ap_pts_nl	VP Point NL PolyAgg	286.63
fit_icov2_nl_ap	VP Count NL PolyAgg	613.25
fit_icov3_pts_sd01	UP Point PointVal	1540.68
fit_icov3_sd01	UP Count PointVal	2899.59
fit_icovap_pts	UP Point PolyAgg	2255.58
fit_icovap	UP Count PolyAgg	3189.34
fit_icov3_pts_nl_sd01	UP Point NL PointVal	2605.85
fit_icov3_nl_sd01	UP Count NL PointVal	2840.81
fit_icovap_nl	UP Point NL PolyAgg	3485.97
fit_icovap_pts_nl	UP Count NL PolyAgg	3670.17

Table 5: Table of computation times for different models. JU: Joint Uncertainty, VP: Value Plugin, UP: Uncertainty Plugin, Point: Observed Point, Count: Aggregated Count, PointVal: Point Values, PolyAgg: Polygon Aggregation.

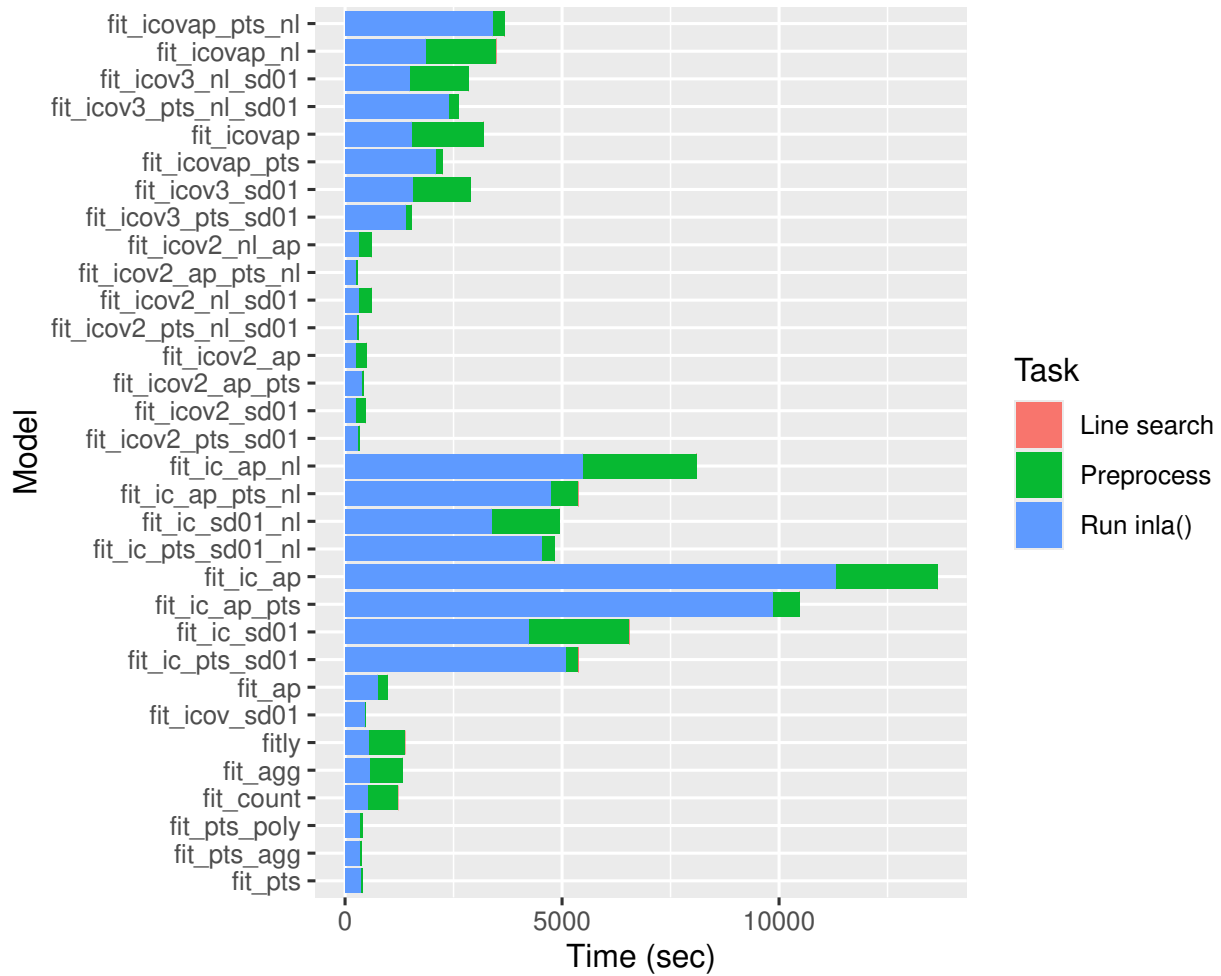


Figure 24: Computation times for different models.

D Convergence Diagnostic for Linearisation

In Section 7.1, we discussed the limitations on convergence iterations. The convergence plots of the models across iterations are shown below. The four panels of convergence diagnostics:

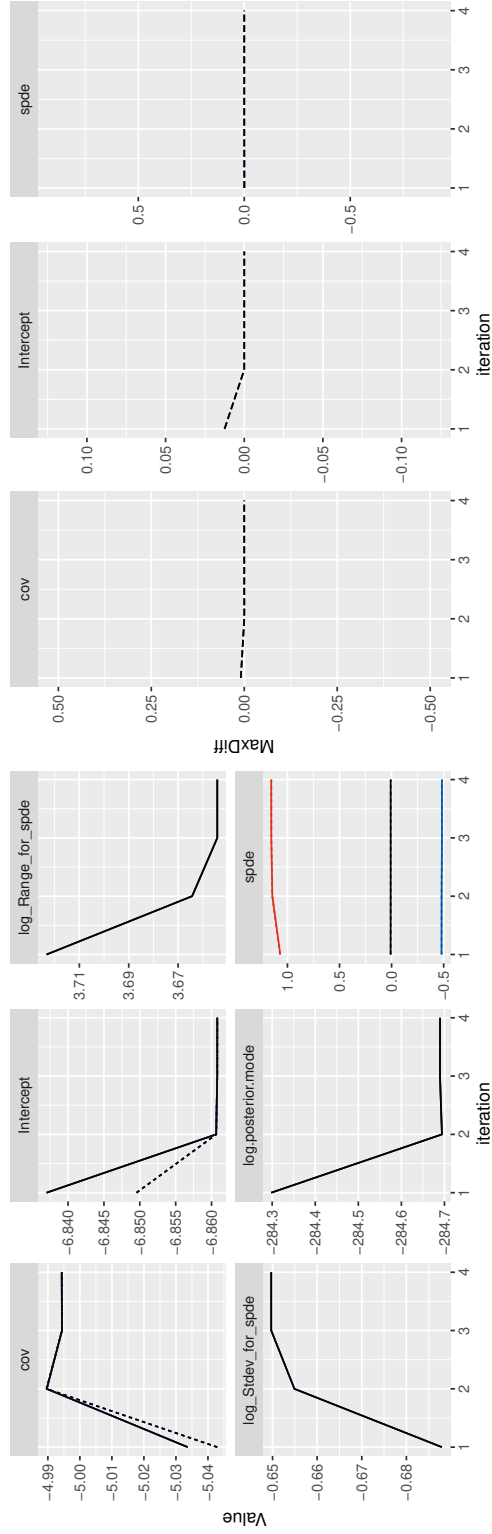
- Tracks: Mode and linearisation values for each effect;
- Mode - Lin: Difference between mode and linearisation values for each effect;
- $|\text{Change}|/\text{sd}$: Absolute change in mode and linearisation values divided by the standard deviation for each effect;

- Change & sd: Absolute change in mode and linearisation values and standard deviation for each effect.

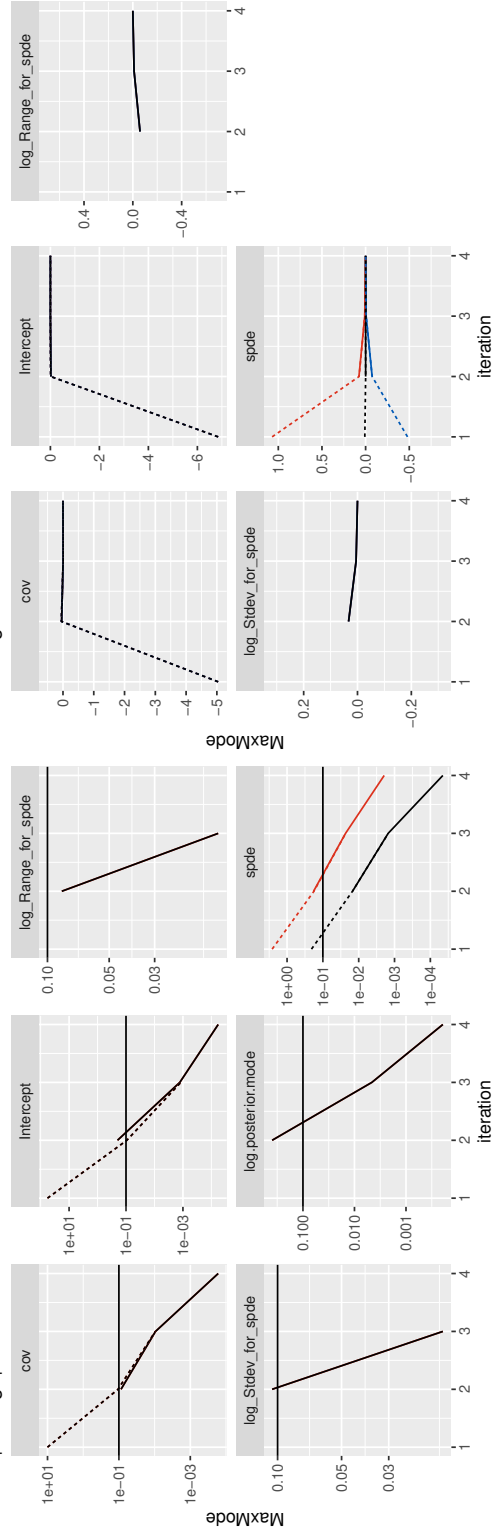
Refer to Table 5 in Appendix C.10 for the model names and descriptions.

Convergence plots for fit_agg

Tracks



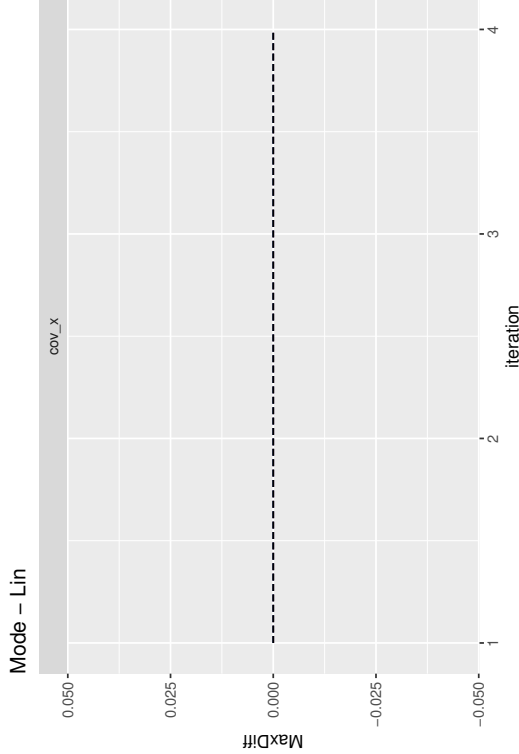
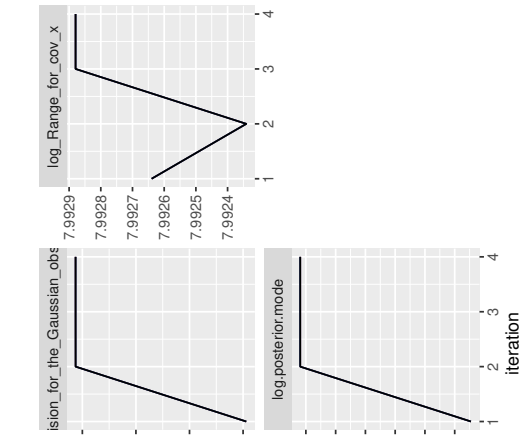
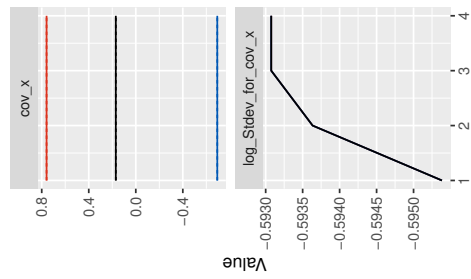
|Change| / sd



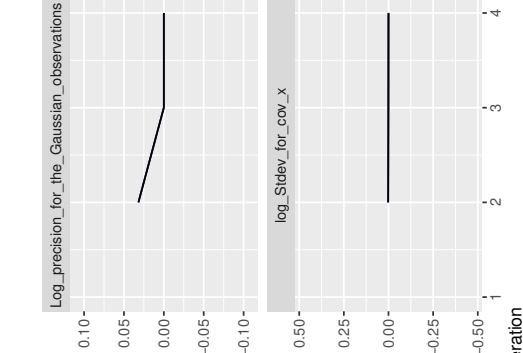
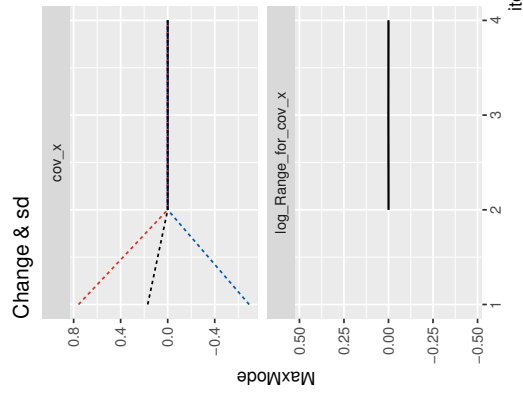
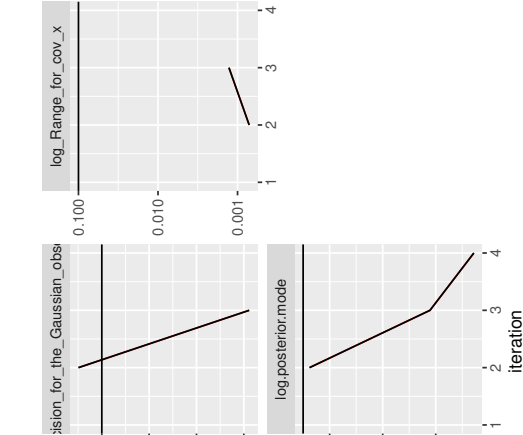
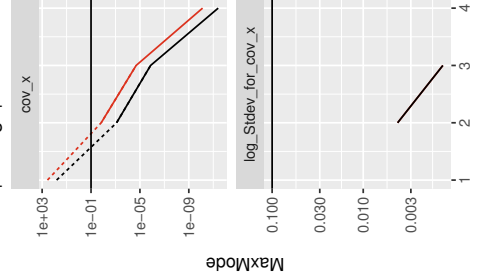
Aspect — Max — Mean — Min — Quantity — Mode — Lin — Mode-Lin — SD

Convergence plots for fit_ap

Tracks



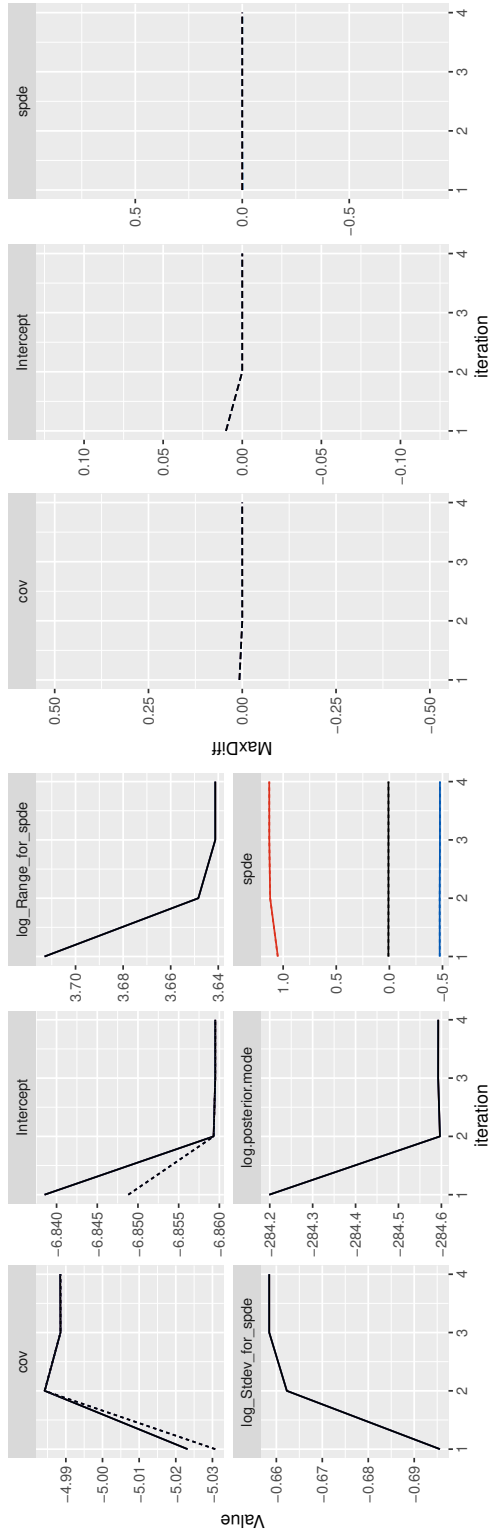
|Change| / sd



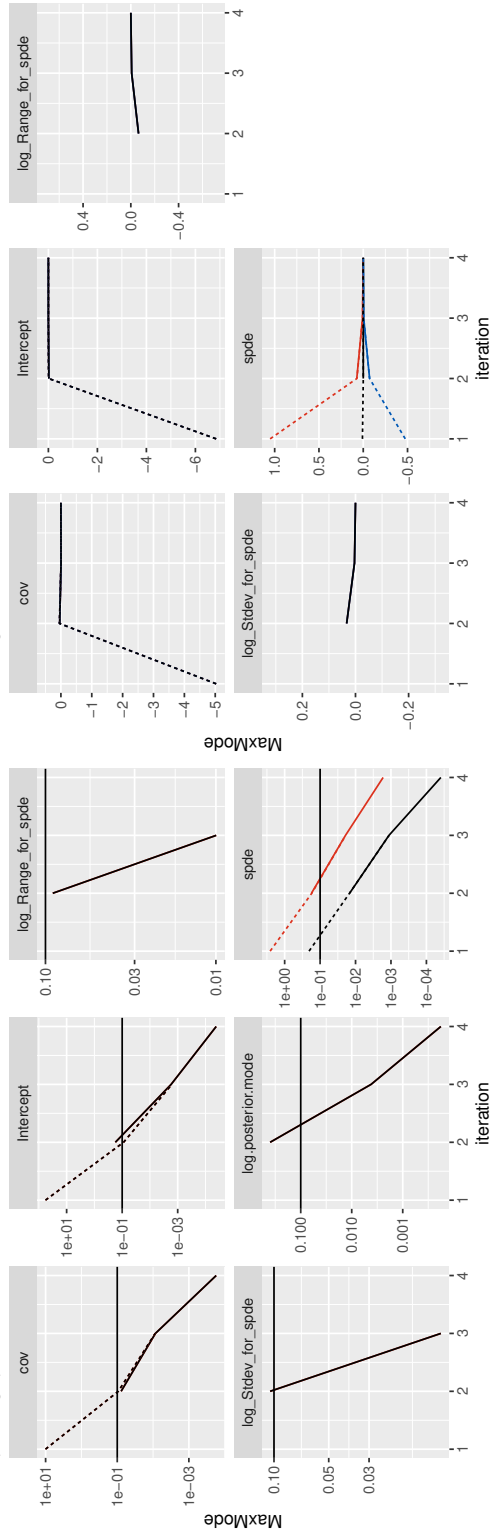
Aspect — Max — Mean — Min — Quantity — Mode — Lin — Mode-Lin — SD

Convergence plots for fit_count

Tracks



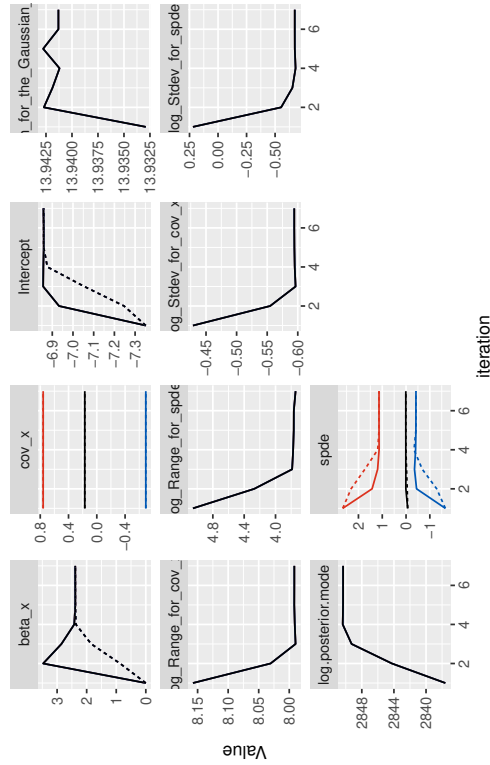
|Change| / sd



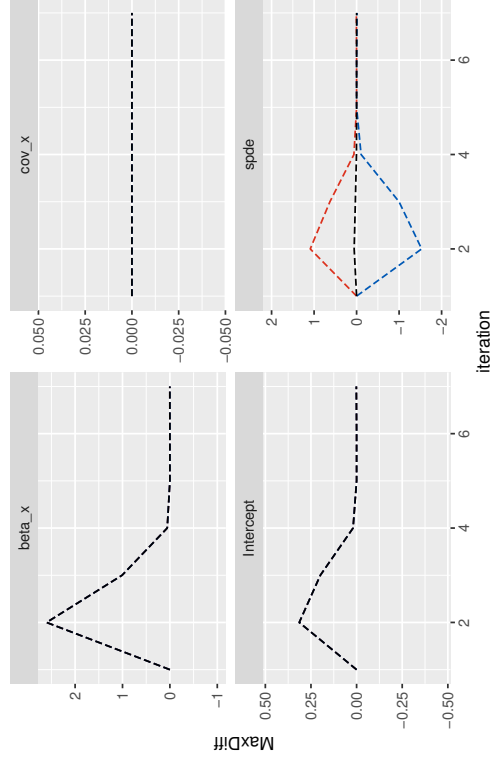
Aspect — Max — Mean — Min — Quantity — Mode — Lin — Mode-Lin — SD

Convergence plots for fit_ic_ap

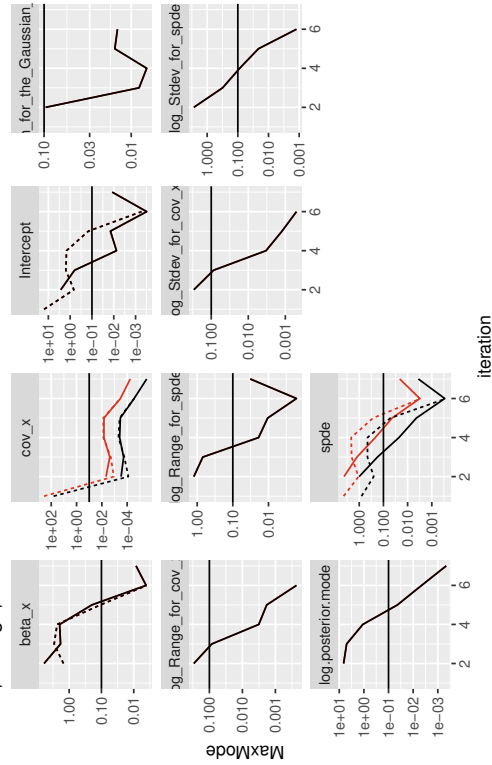
Tracks



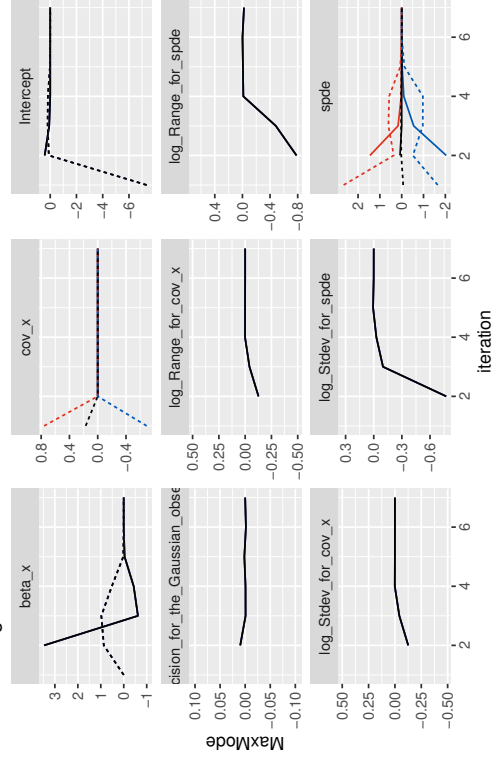
Mode - Lin



|Change| / sd



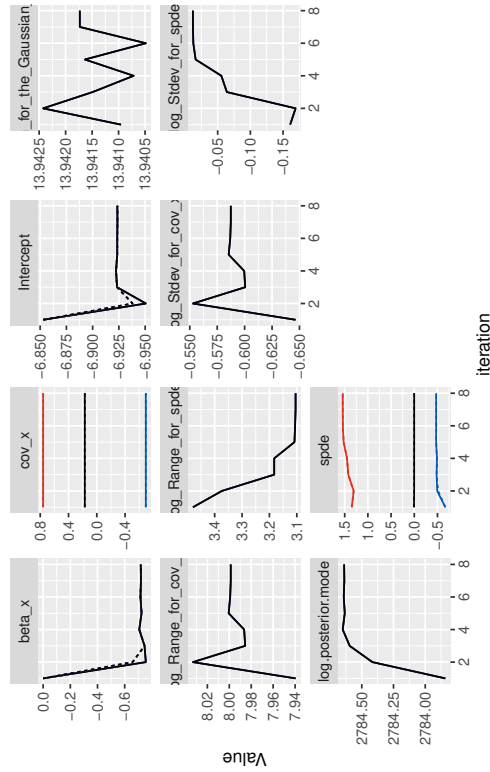
Change & sd



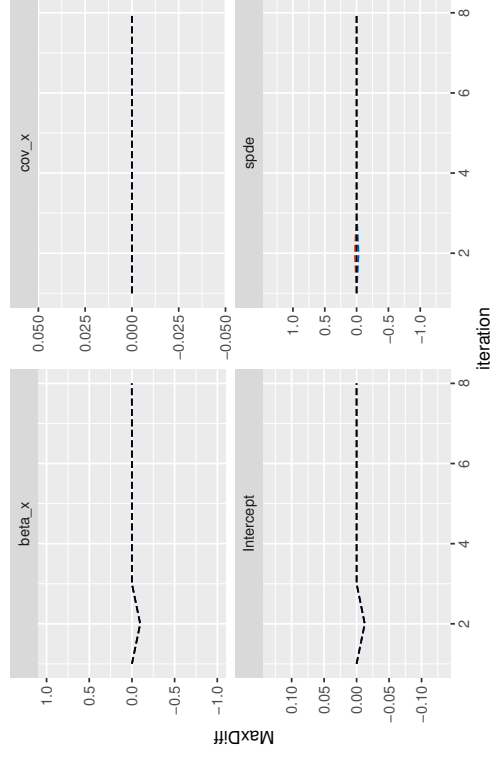
Aspect — Max — Mean — Min Quantity — Mode — Lin — Mode-Lin — SD

Convergence plots for fit_ic_ap_n1

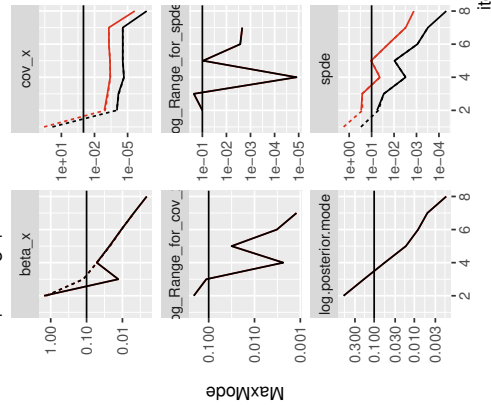
Tracks



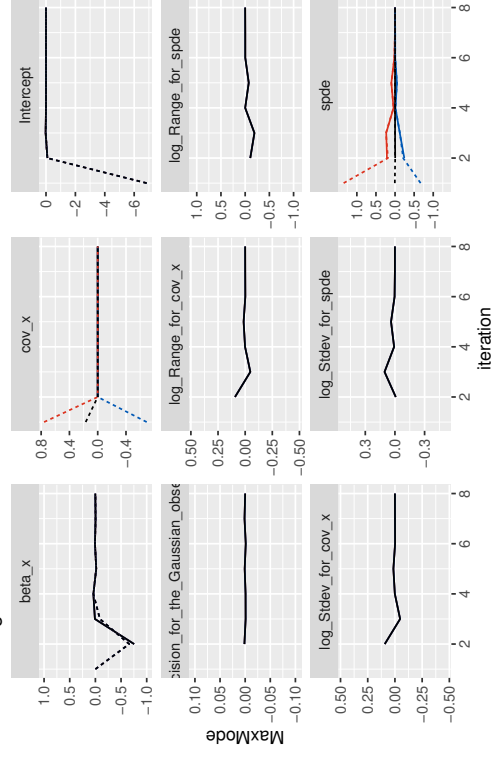
Mode - Lin



|Change| / sd



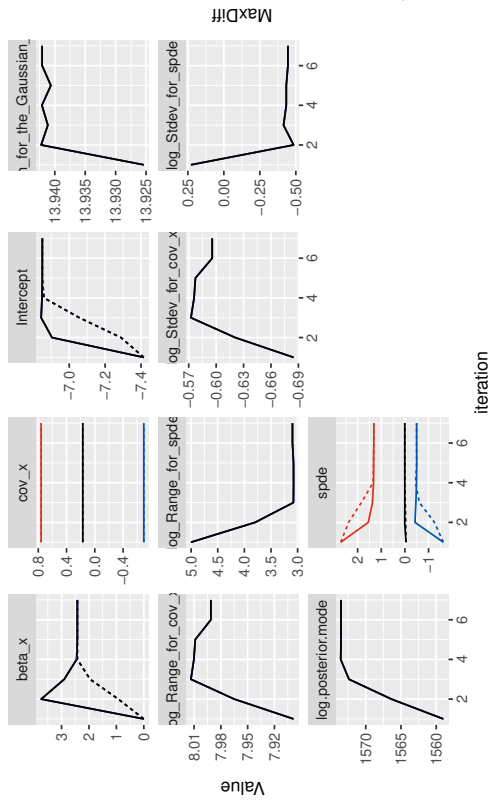
Change & sd



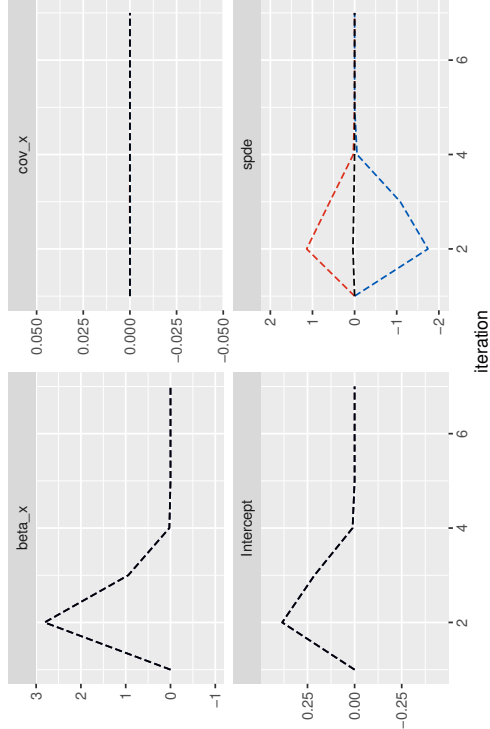
Aspect — Max — Mean — Min — Mode — Lin — Mode-Lin — SD

Convergence plots for fit_ic_ap_pts

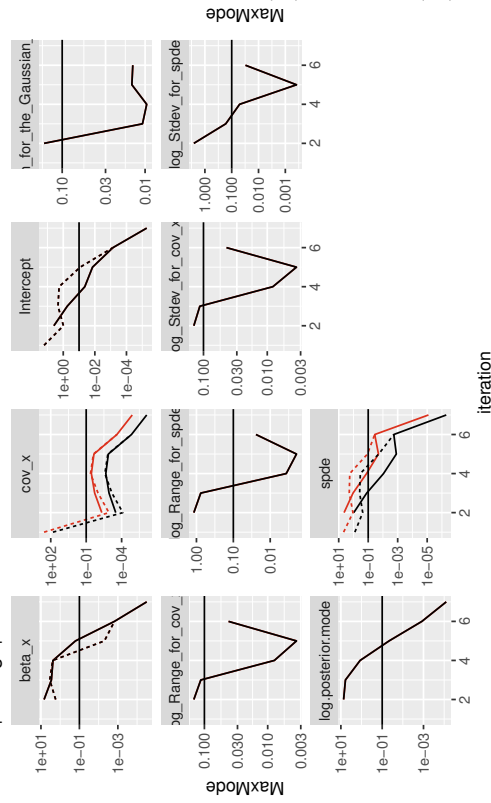
Tracks



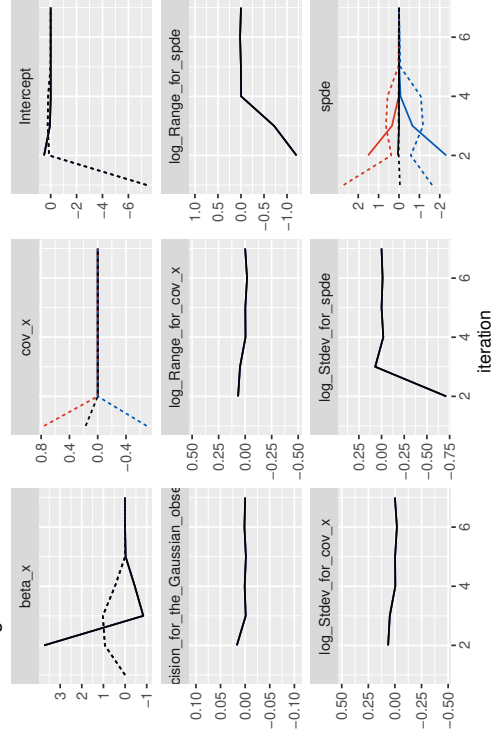
Mode - Lin



|Change| / sd



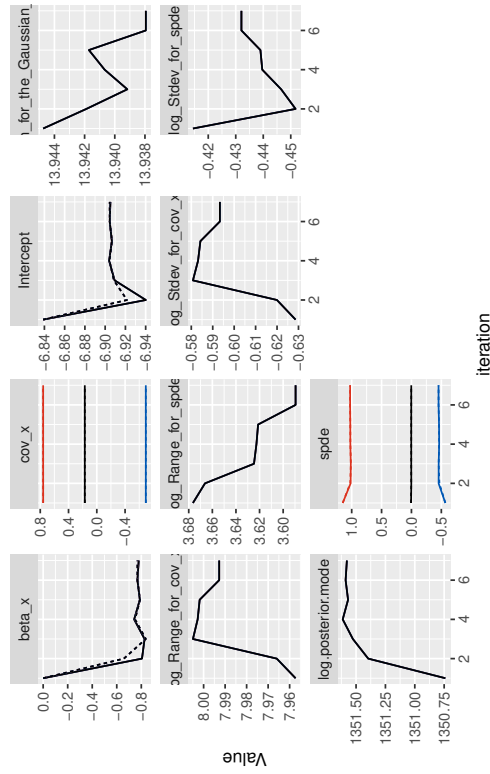
Change & sd



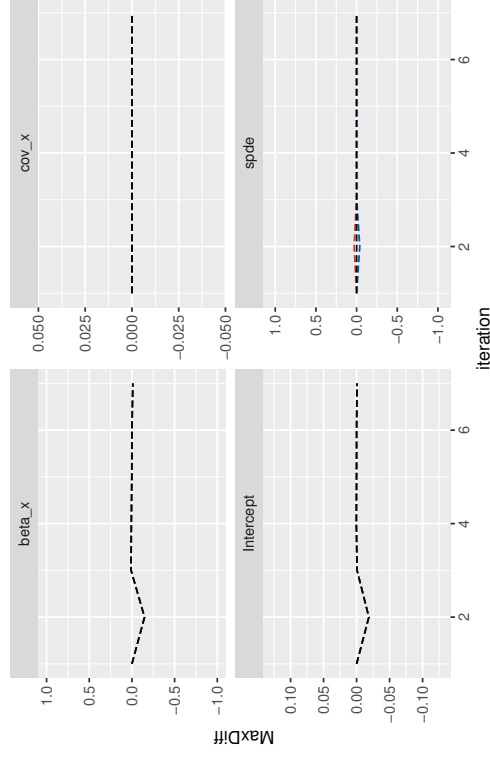
Aspect — Max — Mean — Min — Quantity — Mode — Lin — Mode-Lin — SD

Convergence plots for fit_ic_ap_pts_nl

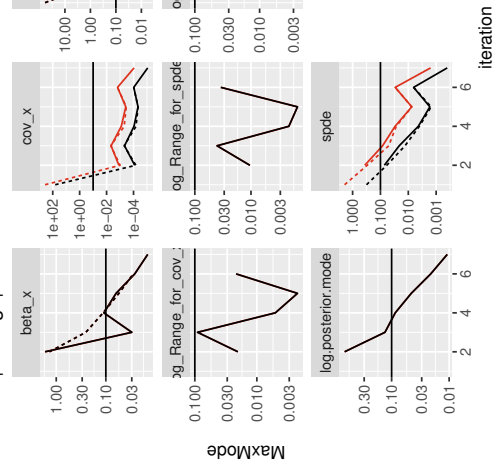
Tracks



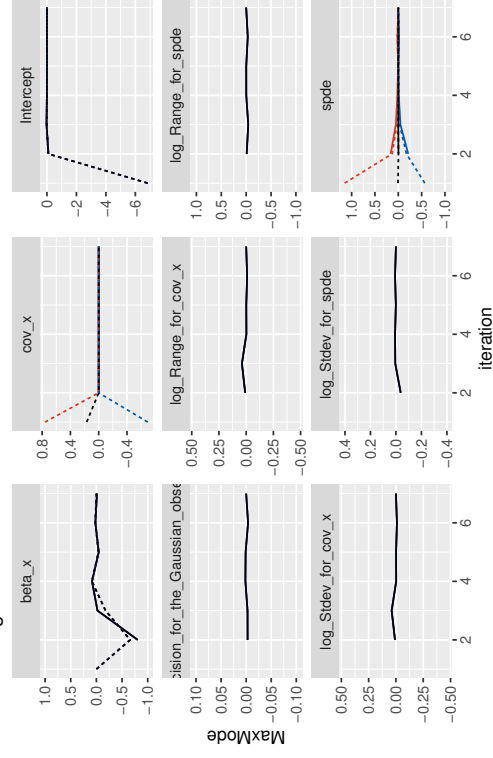
Mode - Lin



|Change| / sd



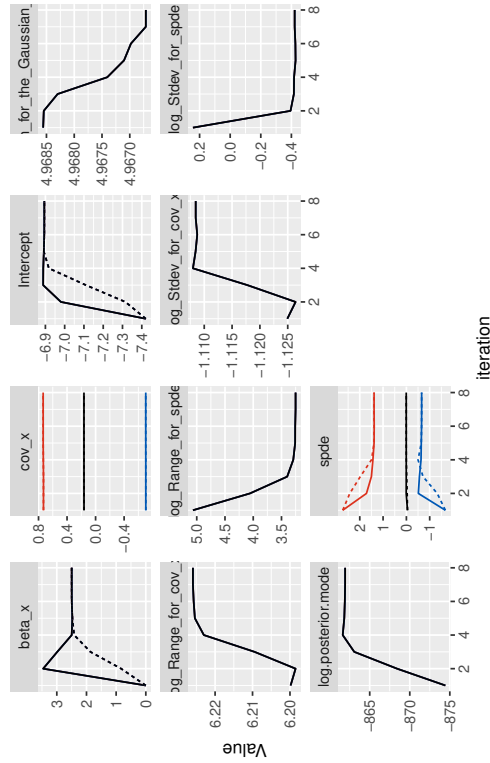
Change & sd



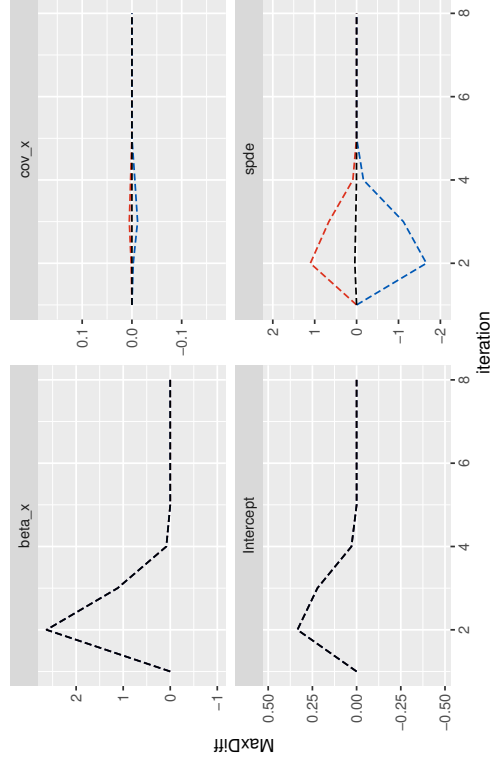
Aspect — Max — Mean — Min — Quantity — Mode — Lin — Mode-Lin — SD

Convergence plots for fit_ic_pts_sd01

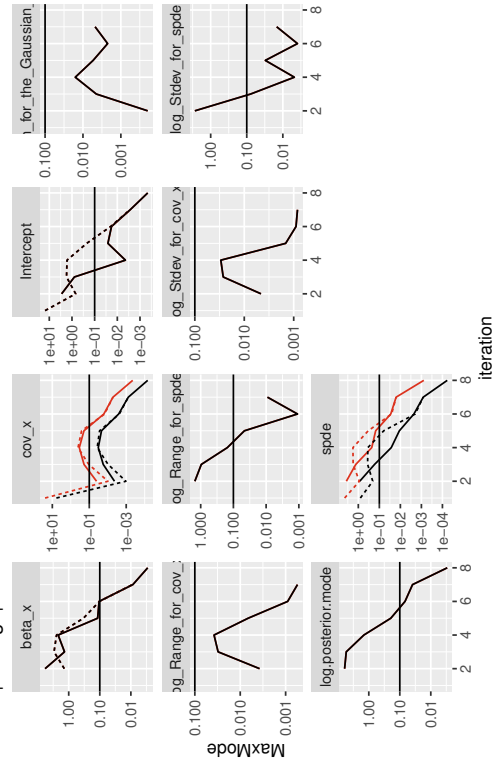
Tracks



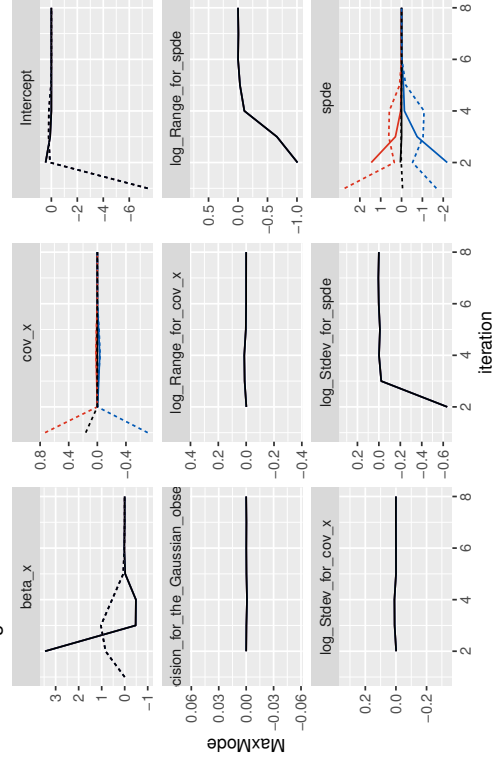
Mode - Lin



|Change| / sd

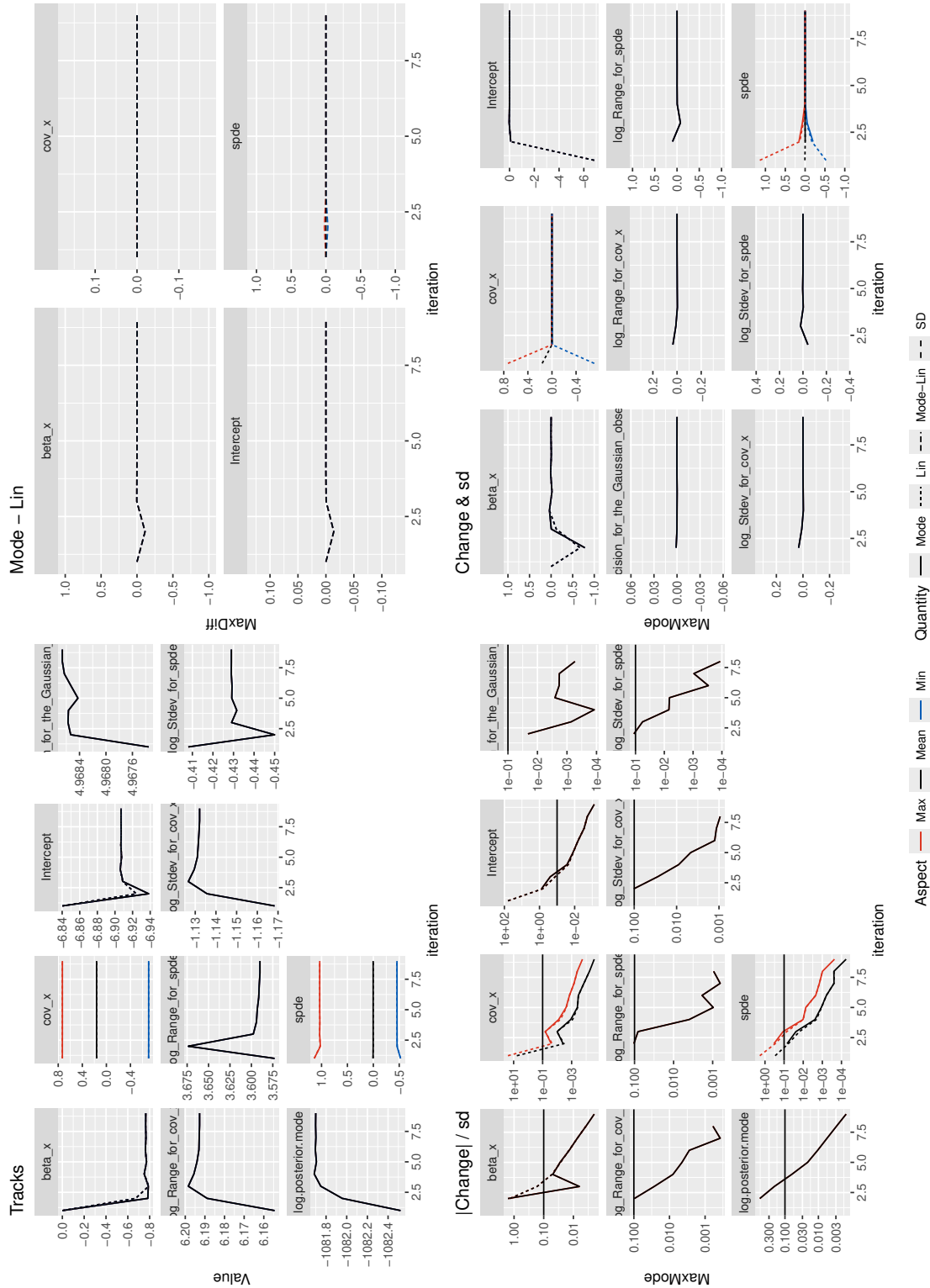


Change & sd



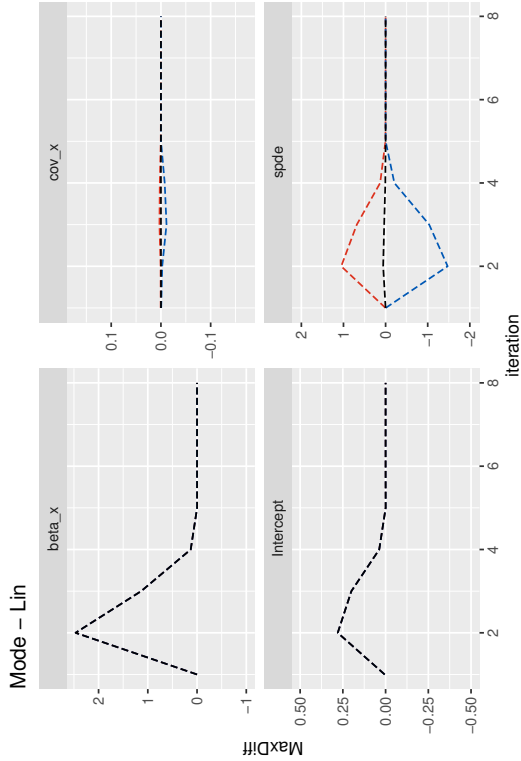
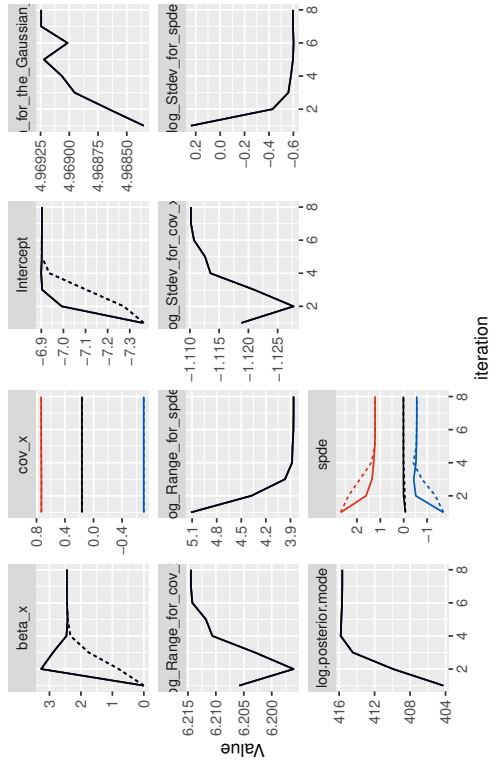
Aspect — Max — Mean — Min — Quantity — Mode — Lin — Mode-Lin — SD

Convergence plots for fit_ic_pts_sd01_n1

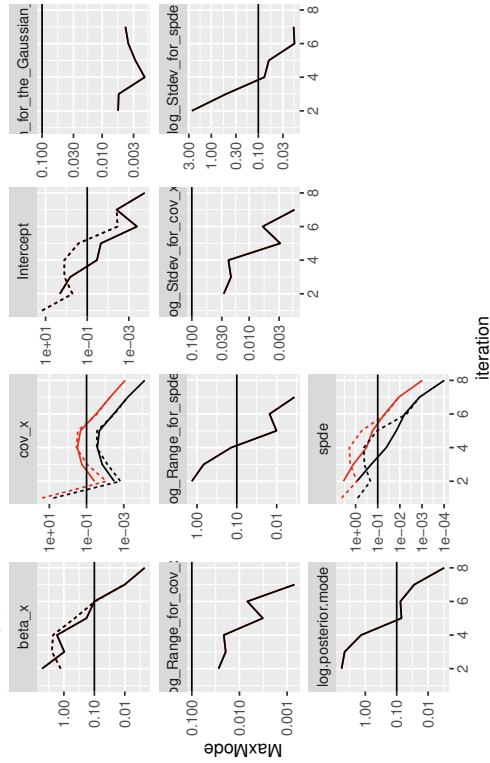


Convergence plots for fit_ic_sd01

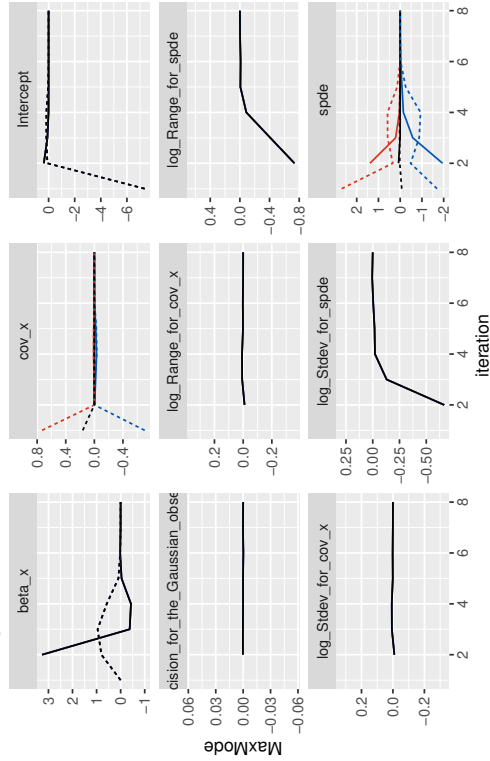
Tracks



|Change| / sd



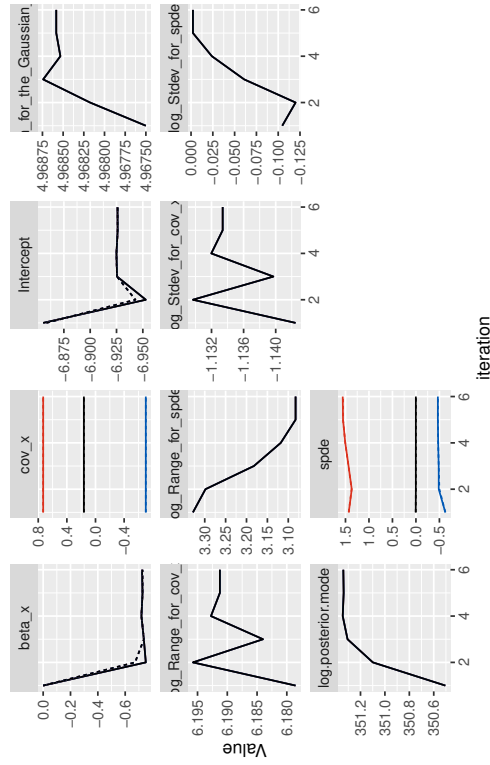
Change & sd



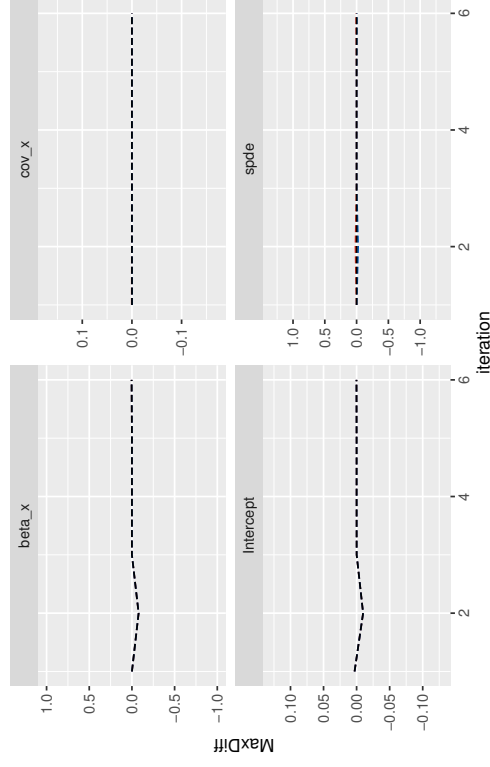
Aspect — Max — Mean — Min — Quantity — Mode — Lin — Mode-Lin — SD

Convergence plots for fit_ic_sd01_n1

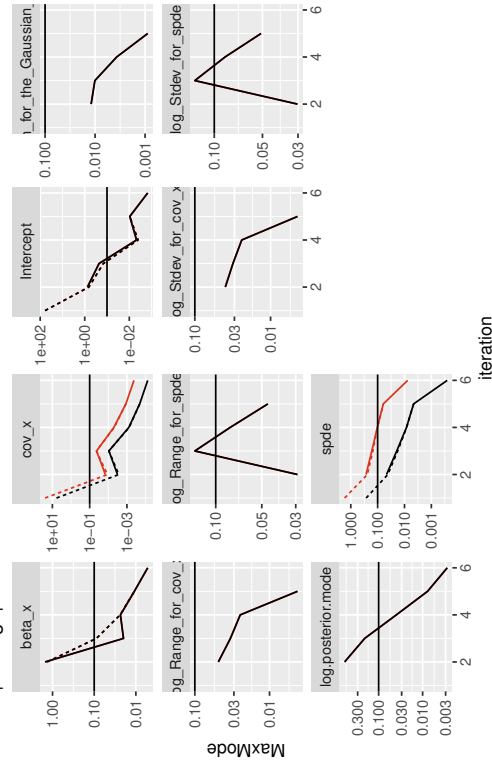
Tracks



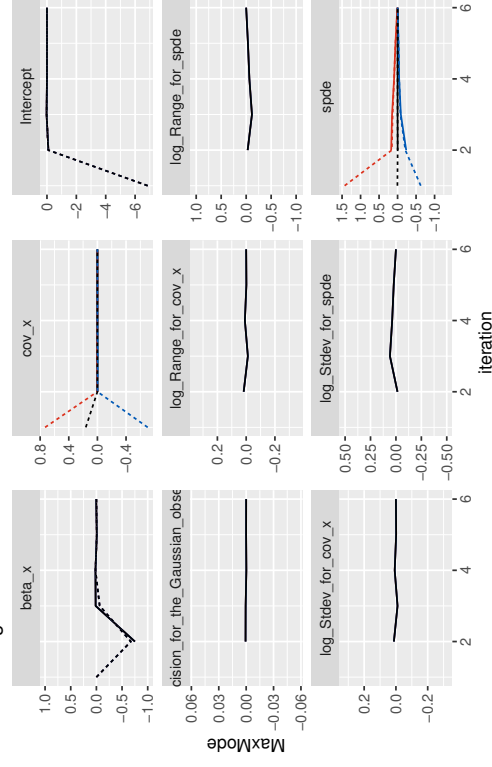
Mode - Lin



|Change| / sd



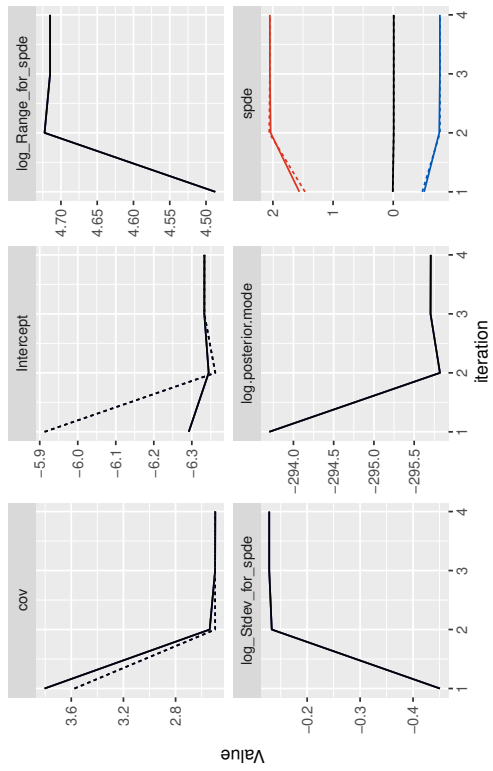
Change & sd



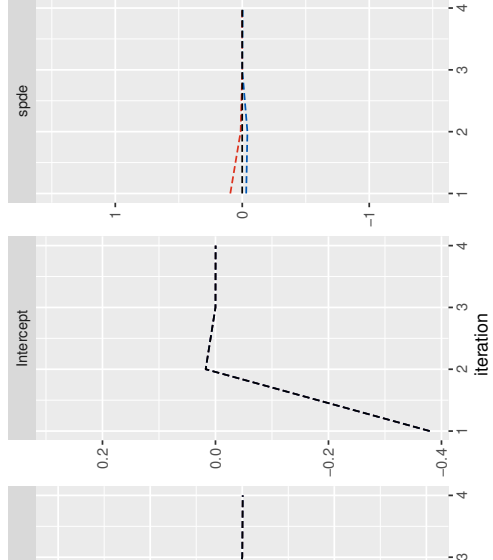
Aspect — Max — Mean — Min — Quantity — Mode — Lin — Mode-Lin — SD

Convergence plots for fit_icov2_ap

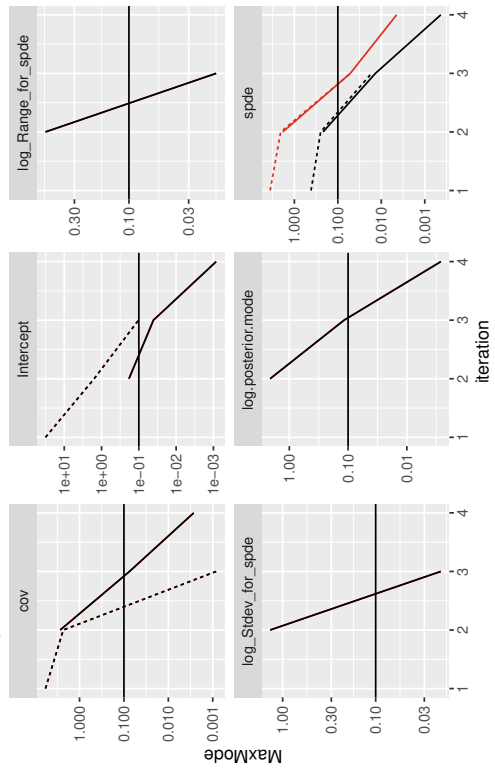
Tracks



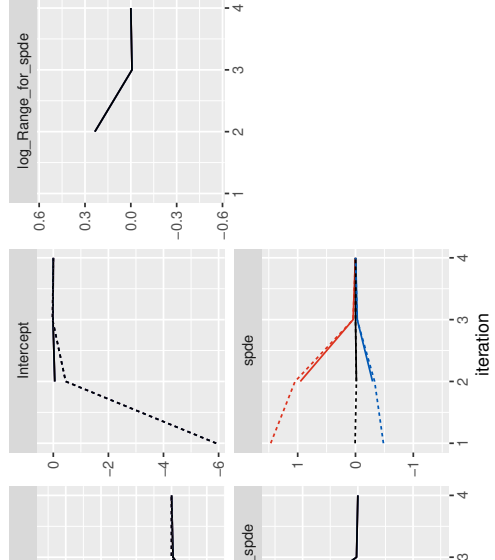
Mode - Lin



|Change| / sd

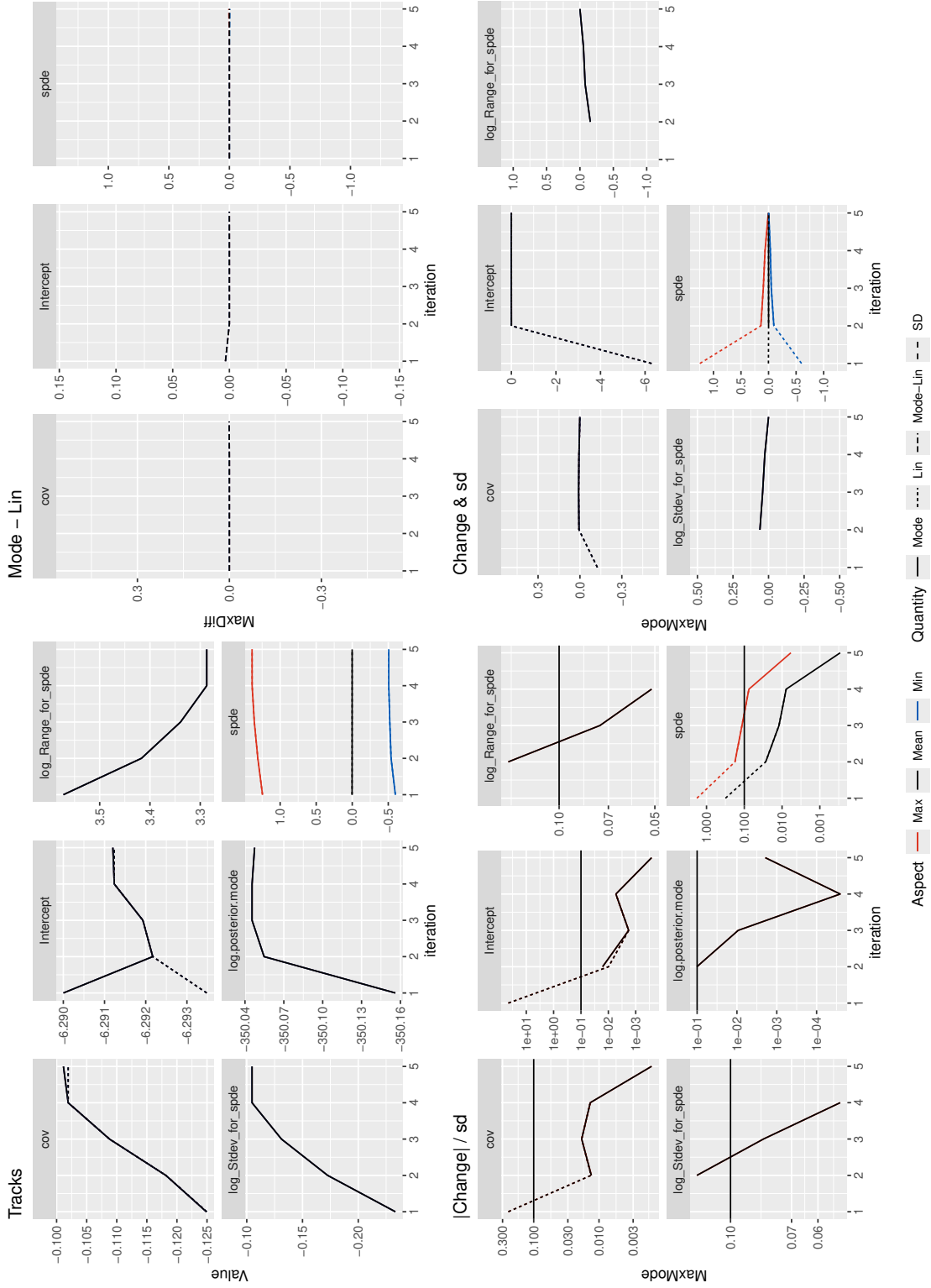


Change & sd

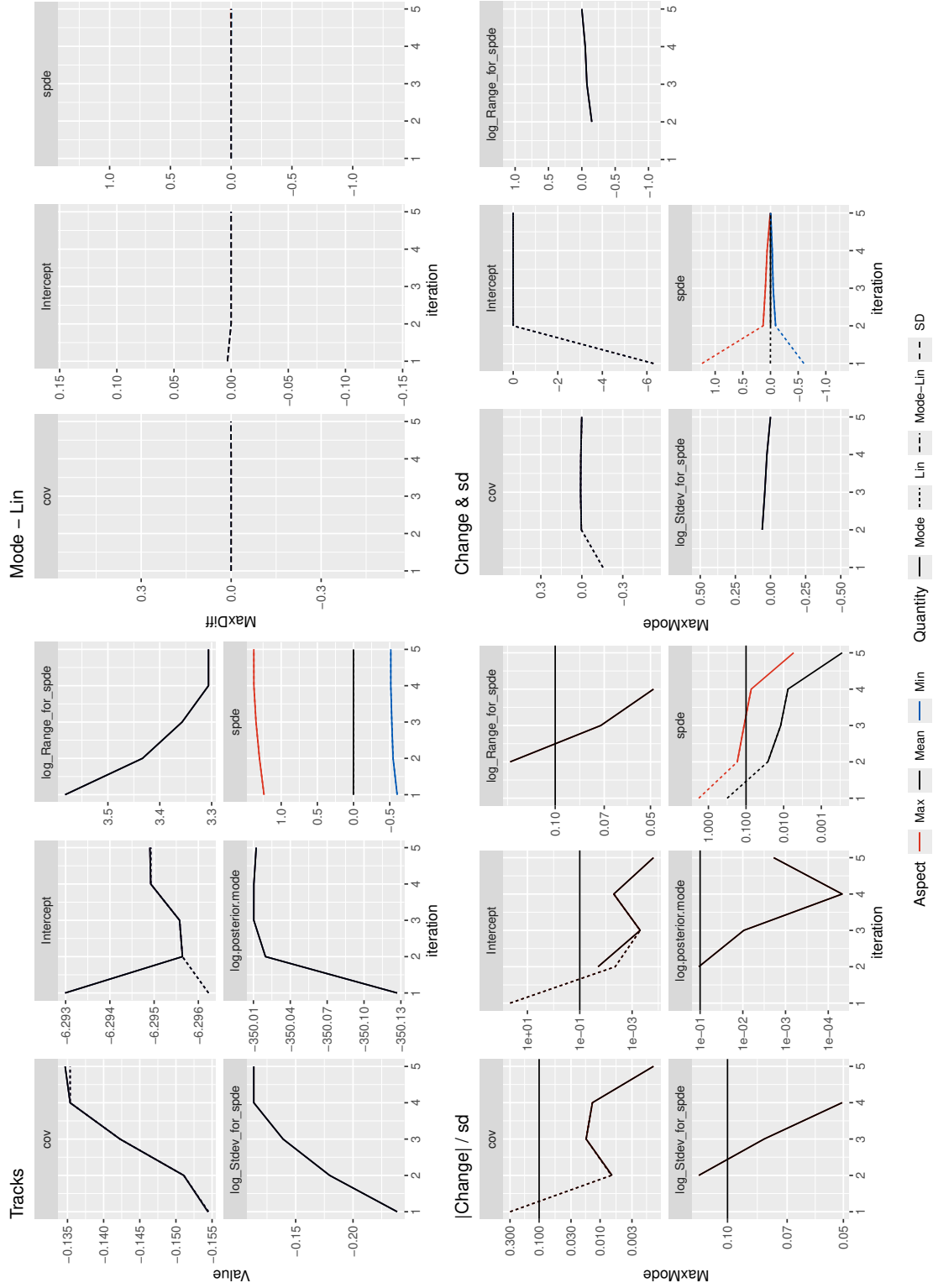


Aspect — Max — Mean — Min — Quantity — Mode — Lin — Mode-Lin — SD

Convergence plots for fit_icov2_nl_ap

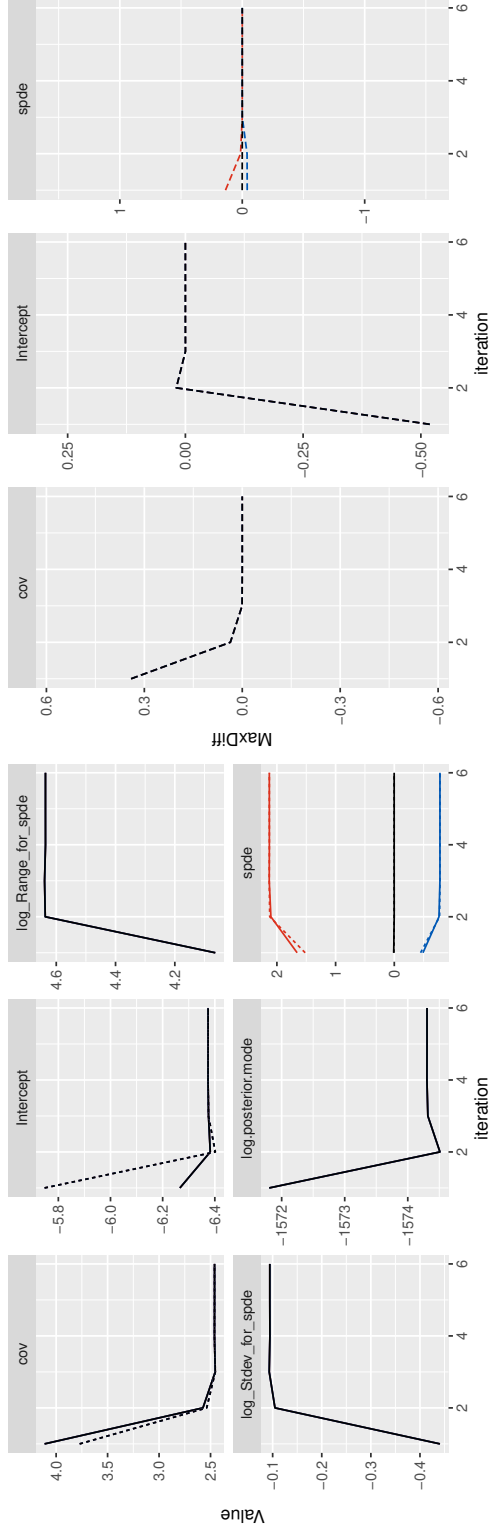


Convergence plots for fit_icov2_n1_sd01

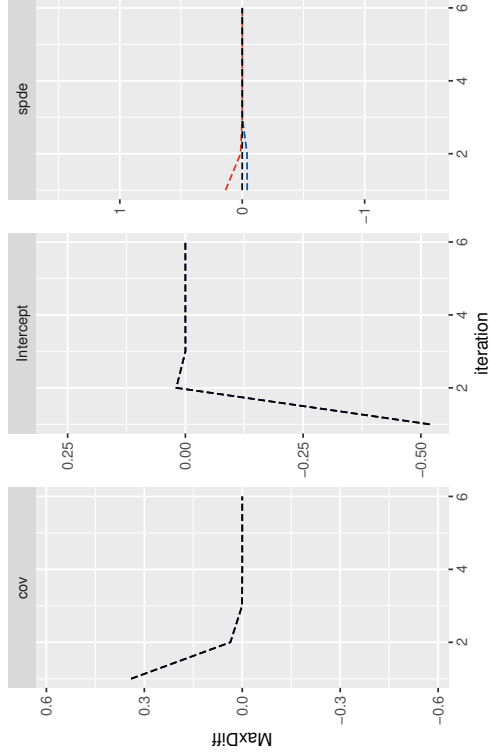


Convergence plots for fit_icov2_ap_pts

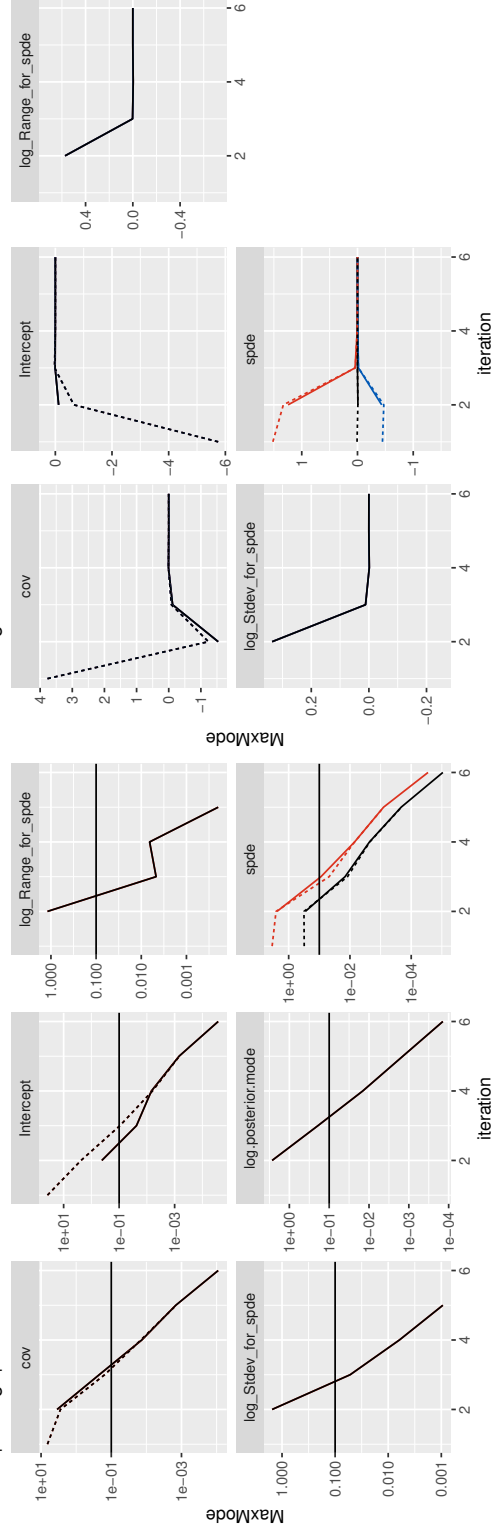
Tracks



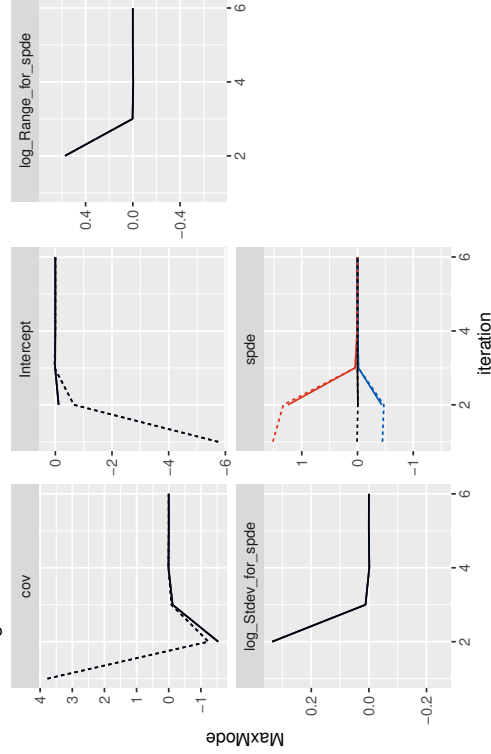
Mode - Lin



|Change| / sd

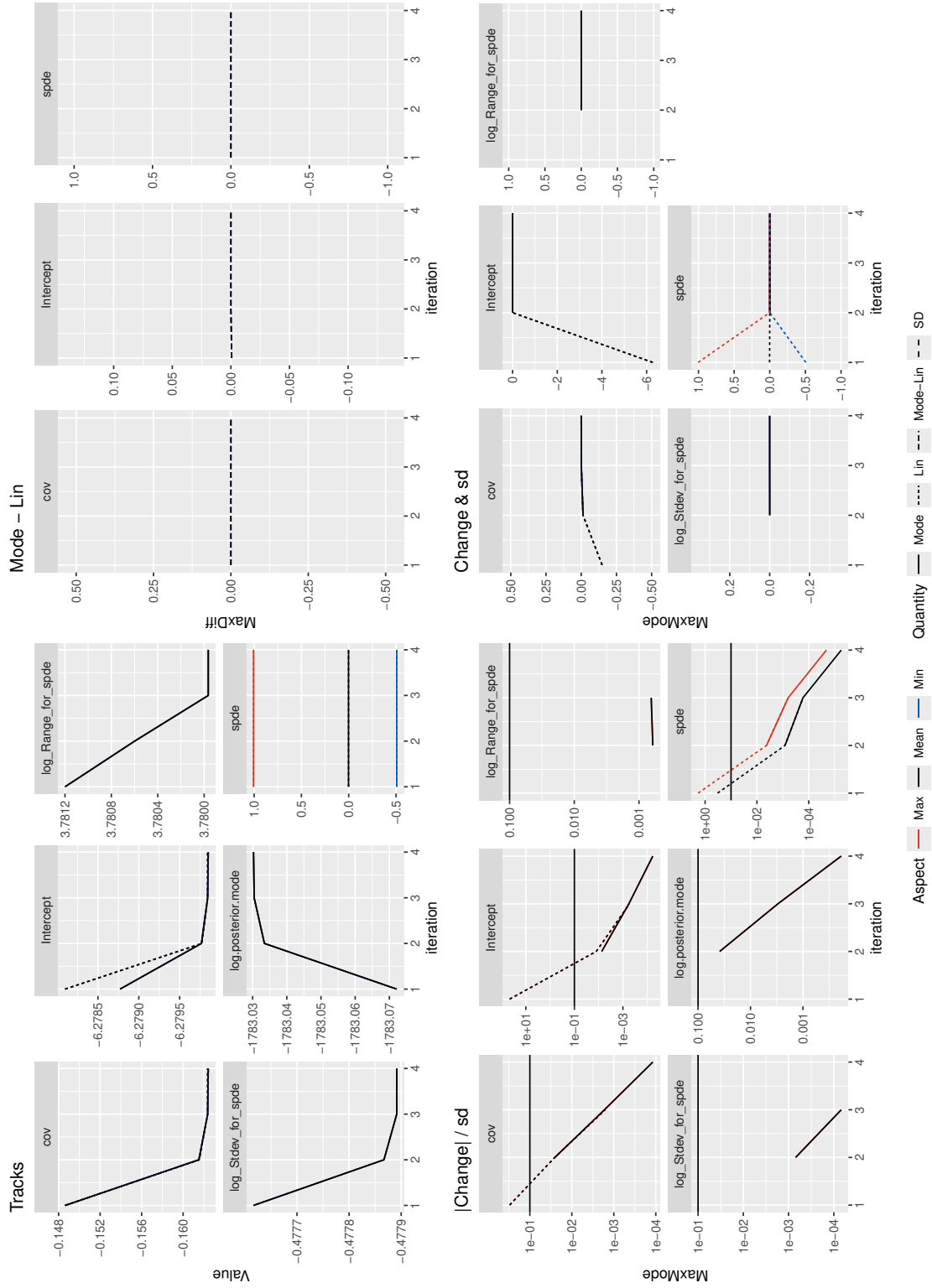


Change & sd



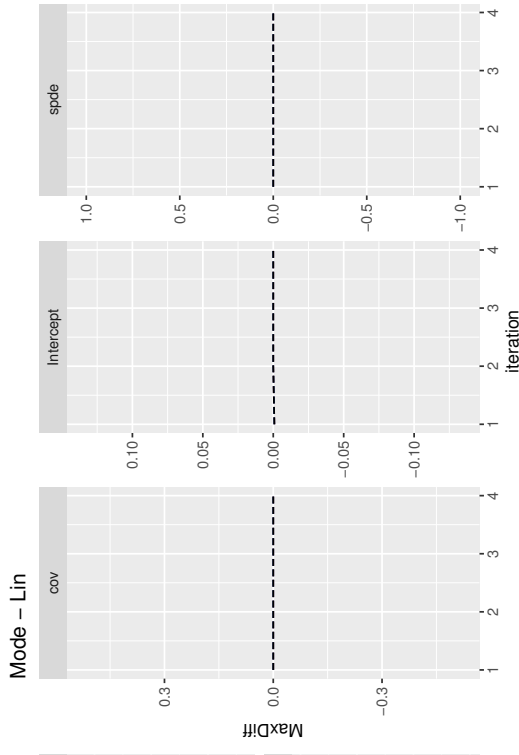
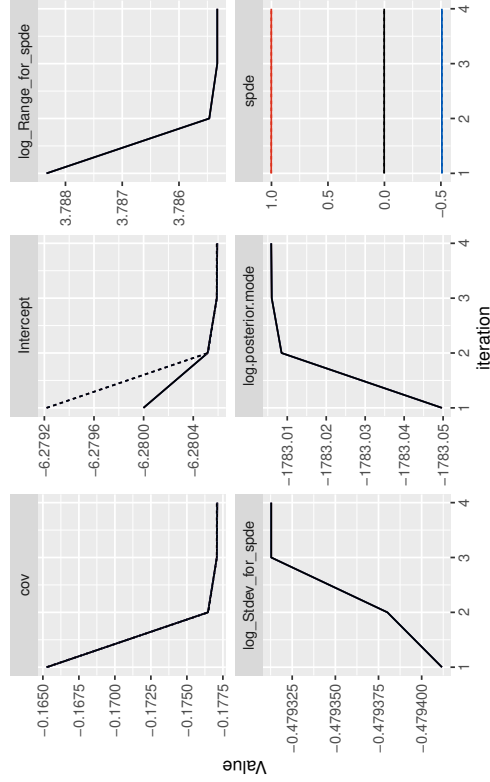
Aspect — Max — Mean — Min Quantity — Mode — Lin — Mode-Lin — SD

Convergence plots for fit_icov2_ap_pts_n1

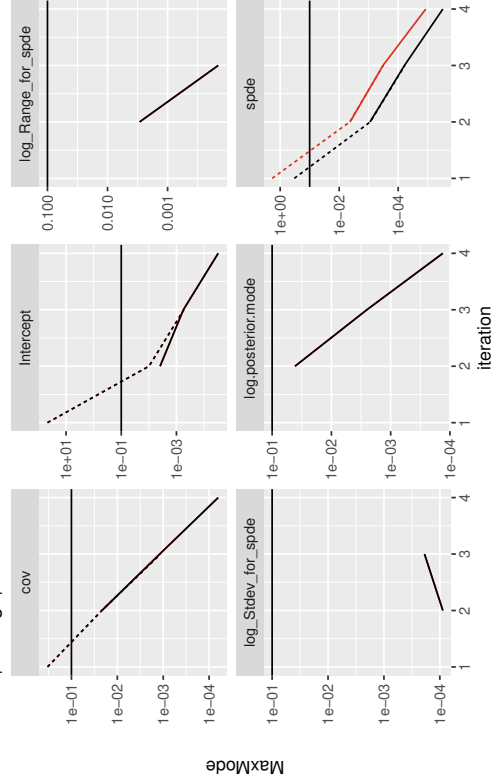


Convergence plots for fit_icov2_pts_nl_sd01

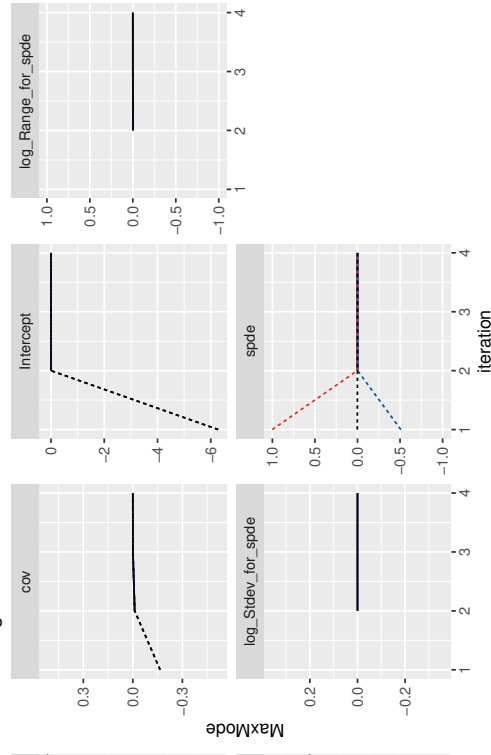
Tracks



|Change| / sd

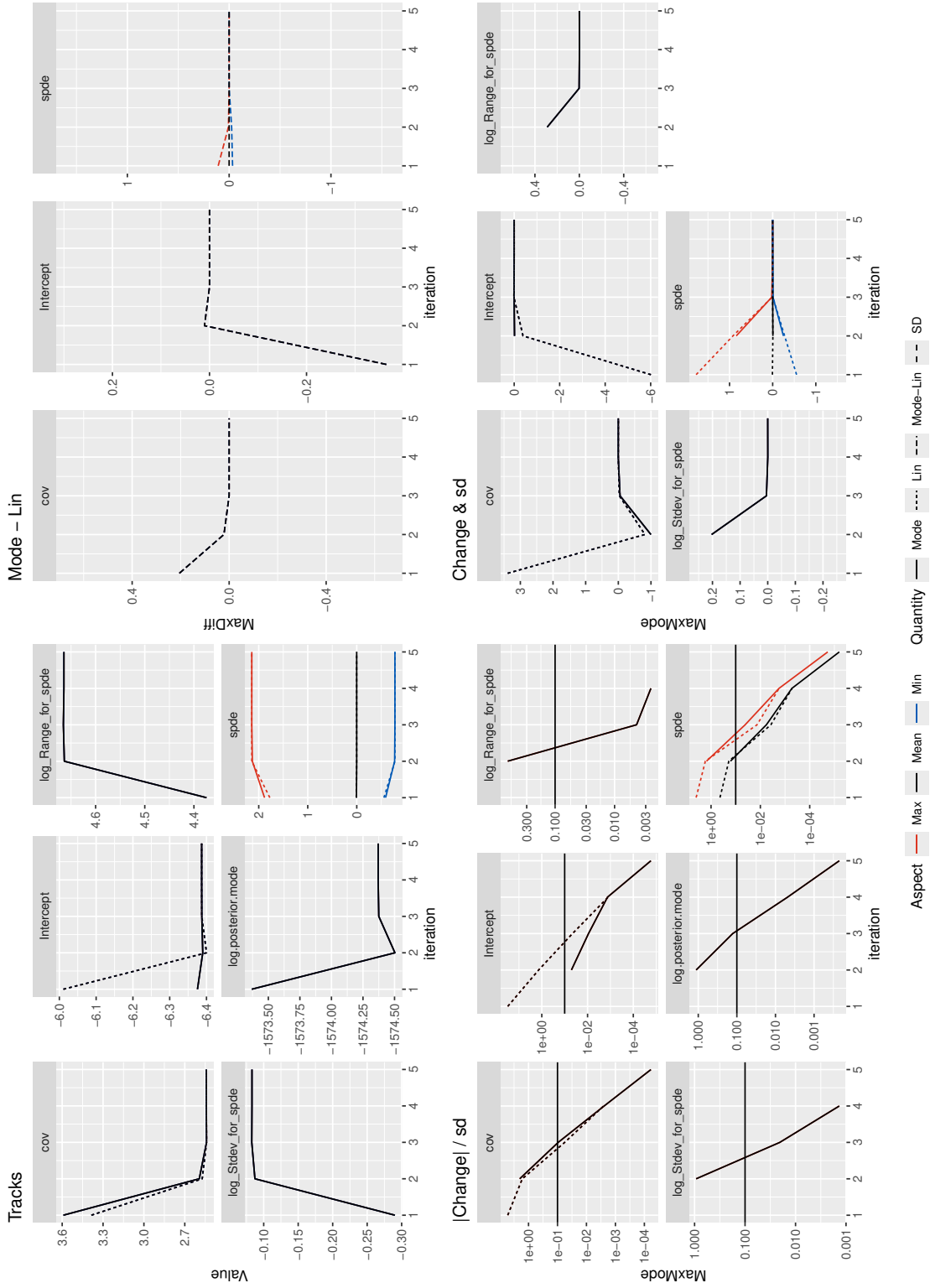


Change & sd



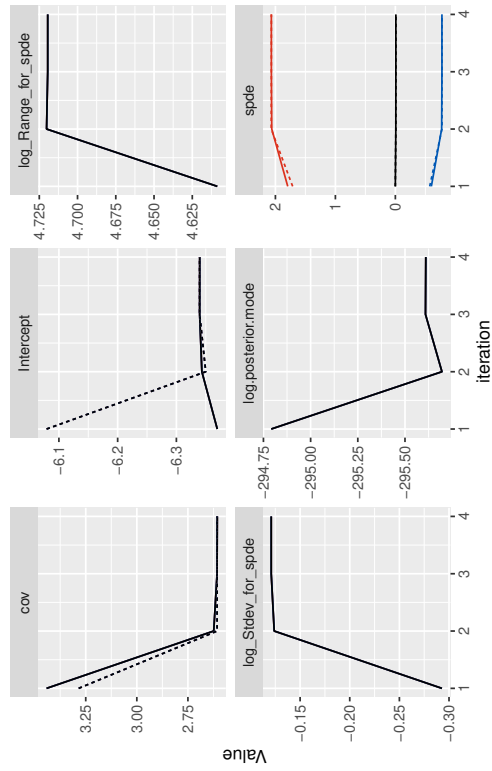
Aspect — Max — Mean — Min — Quantity — Mode — Lin — Mode-Lin — SD

Convergence plots for fit_icov2_pts_sd01

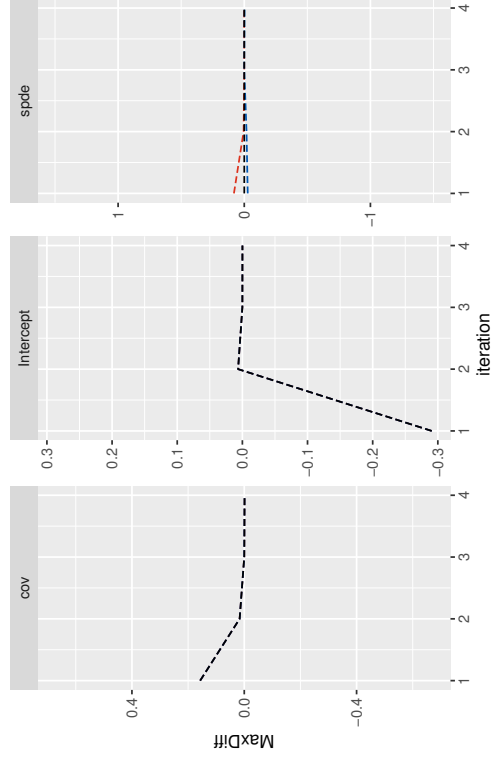


Convergence plots for fit_icov2_sd01

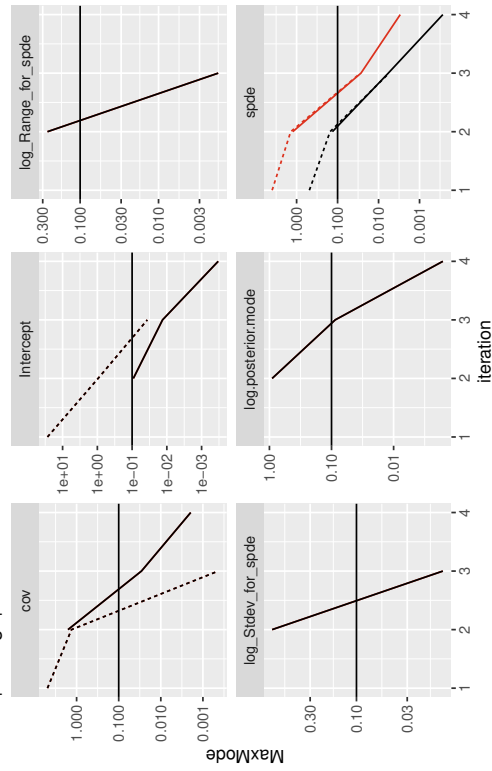
Tracks



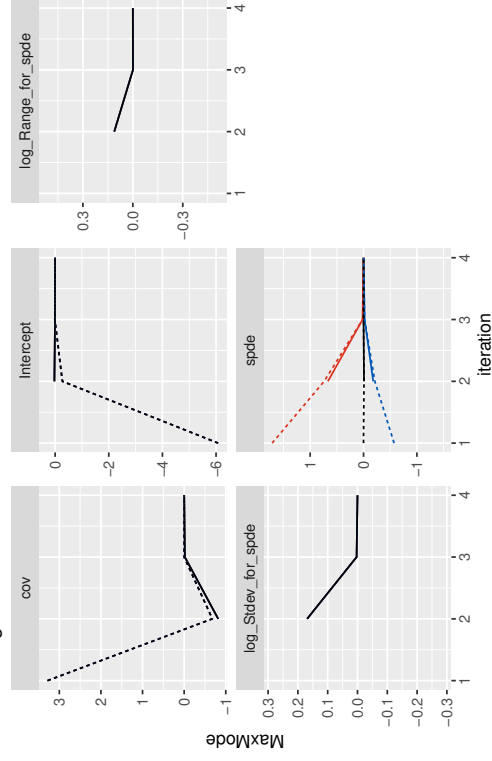
Mode - Lin



|Change| / sd

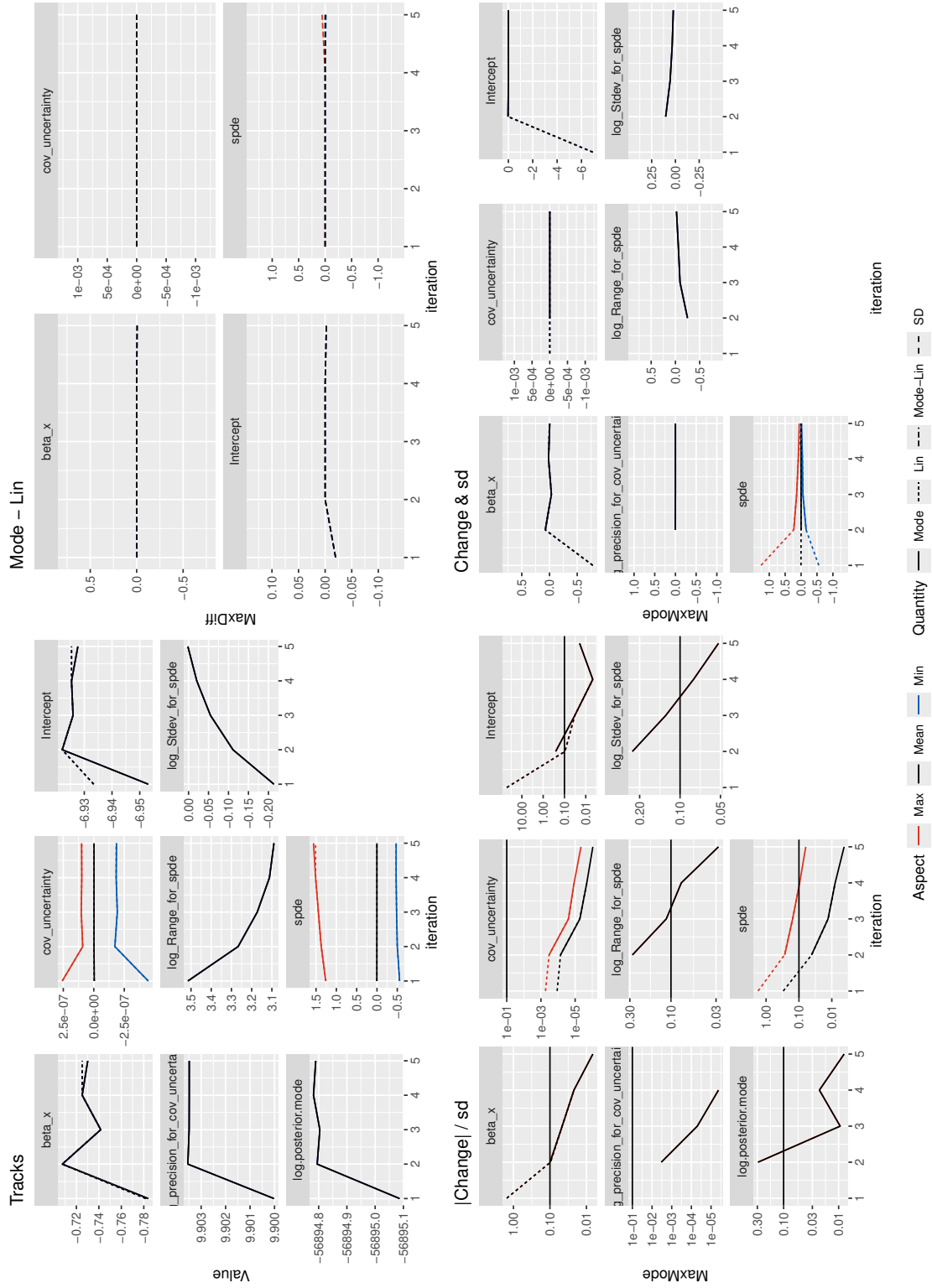


Change & sd



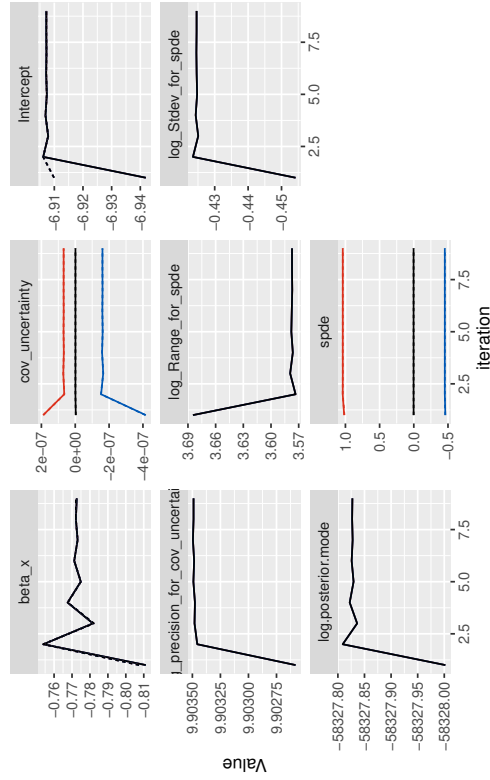
Aspect — Max — Mean — Min — Quantity — Mode — Lin — Mode-Lin — SD

Convergence plots for fit_icov3_nl_sd01

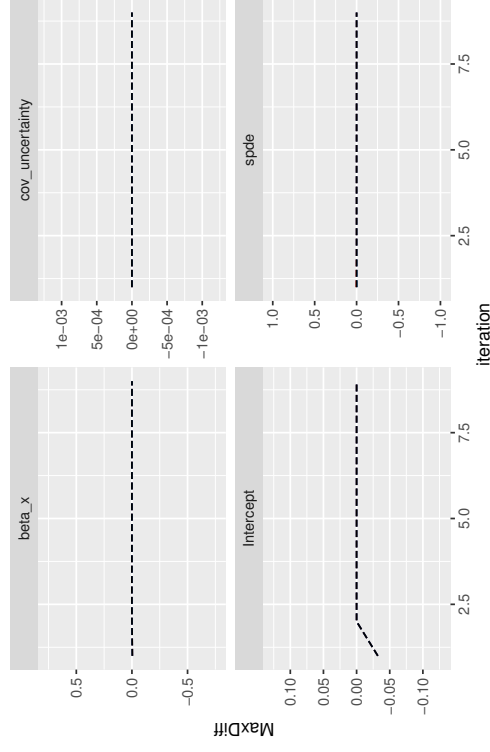


Convergence plots for fit_icov3_pts_n1_sd01

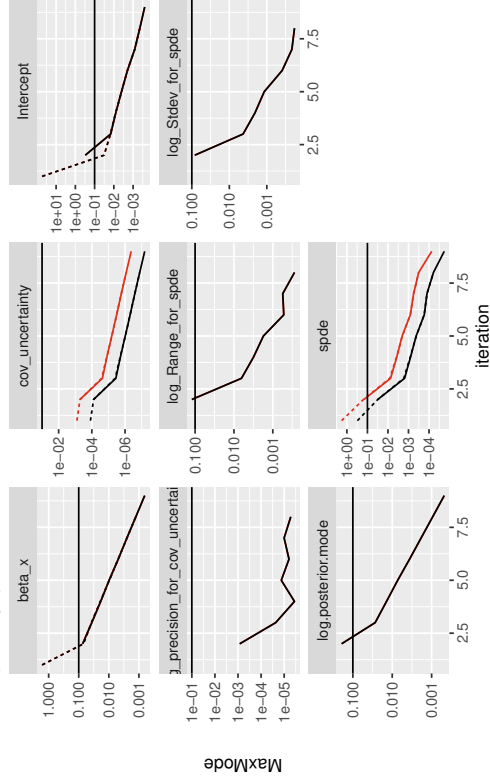
Tracks



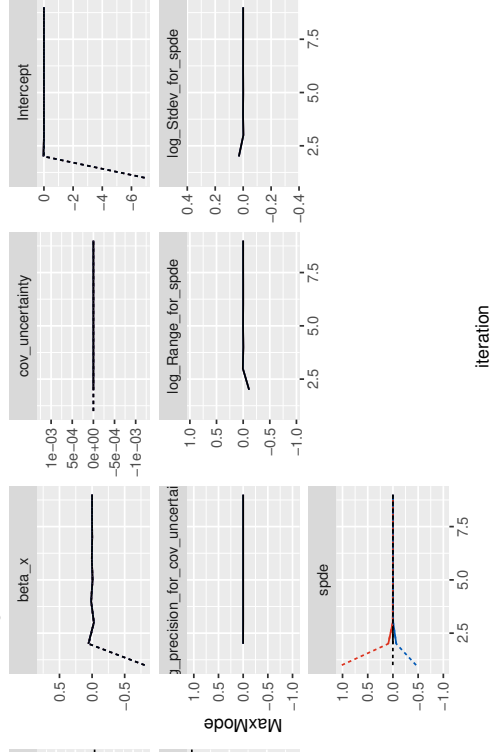
Mode - Lin



|Change| / sd



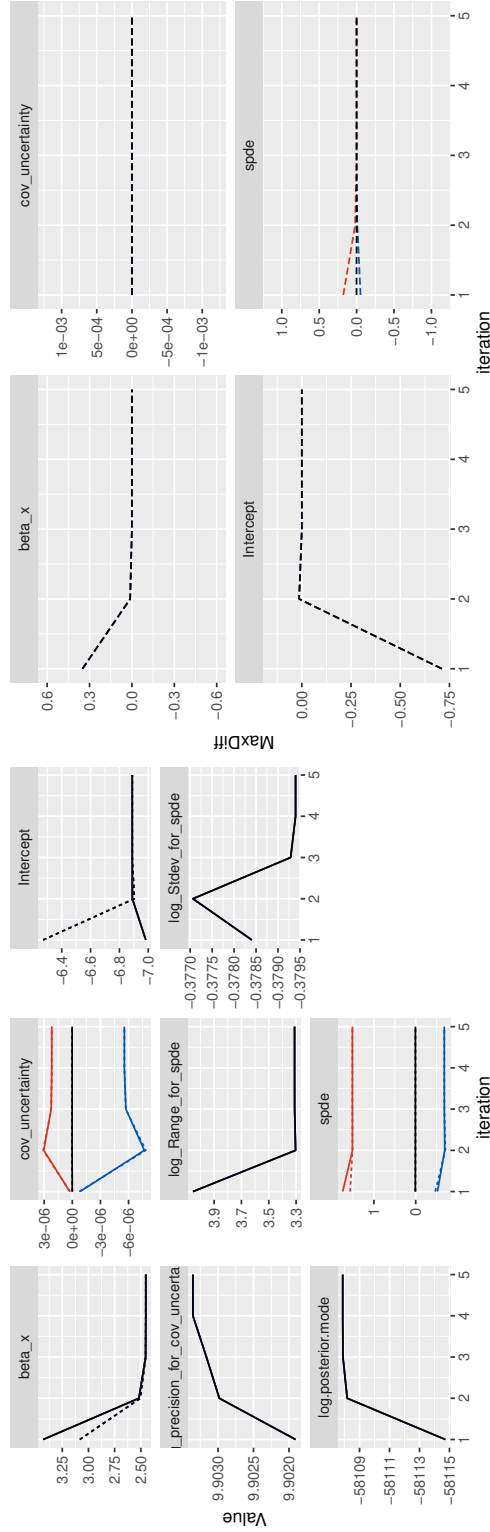
Change & sd



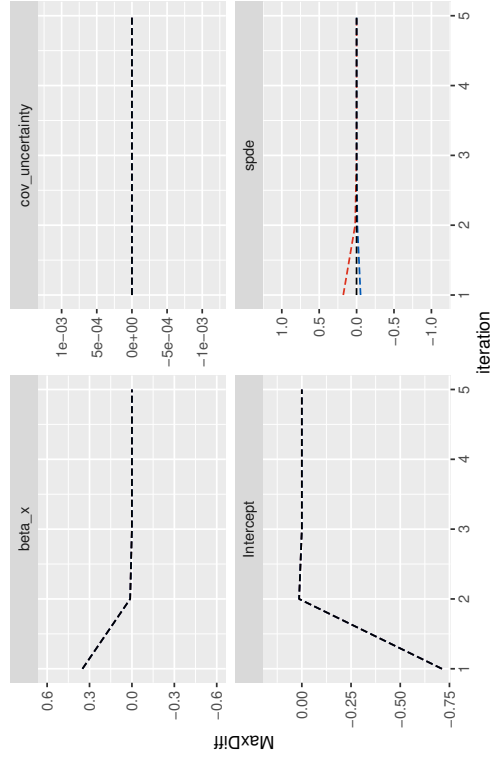
Aspect | Max | Mean | Min | Quantity | Mode | Lin | Mode-Lin | SD

Convergence plots for fit_icov3_pts_sd01

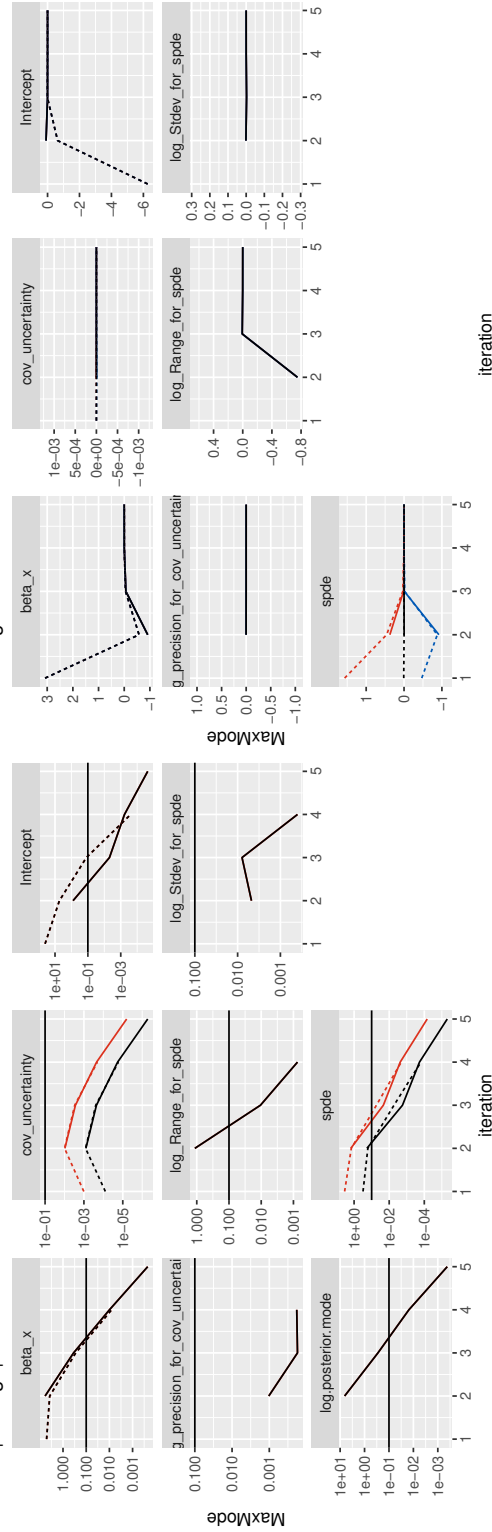
Tracks



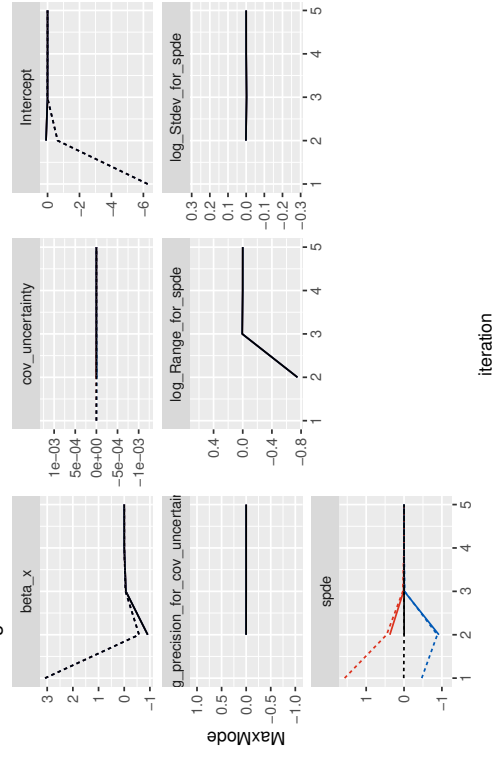
Mode - Lin



|Change| / sd

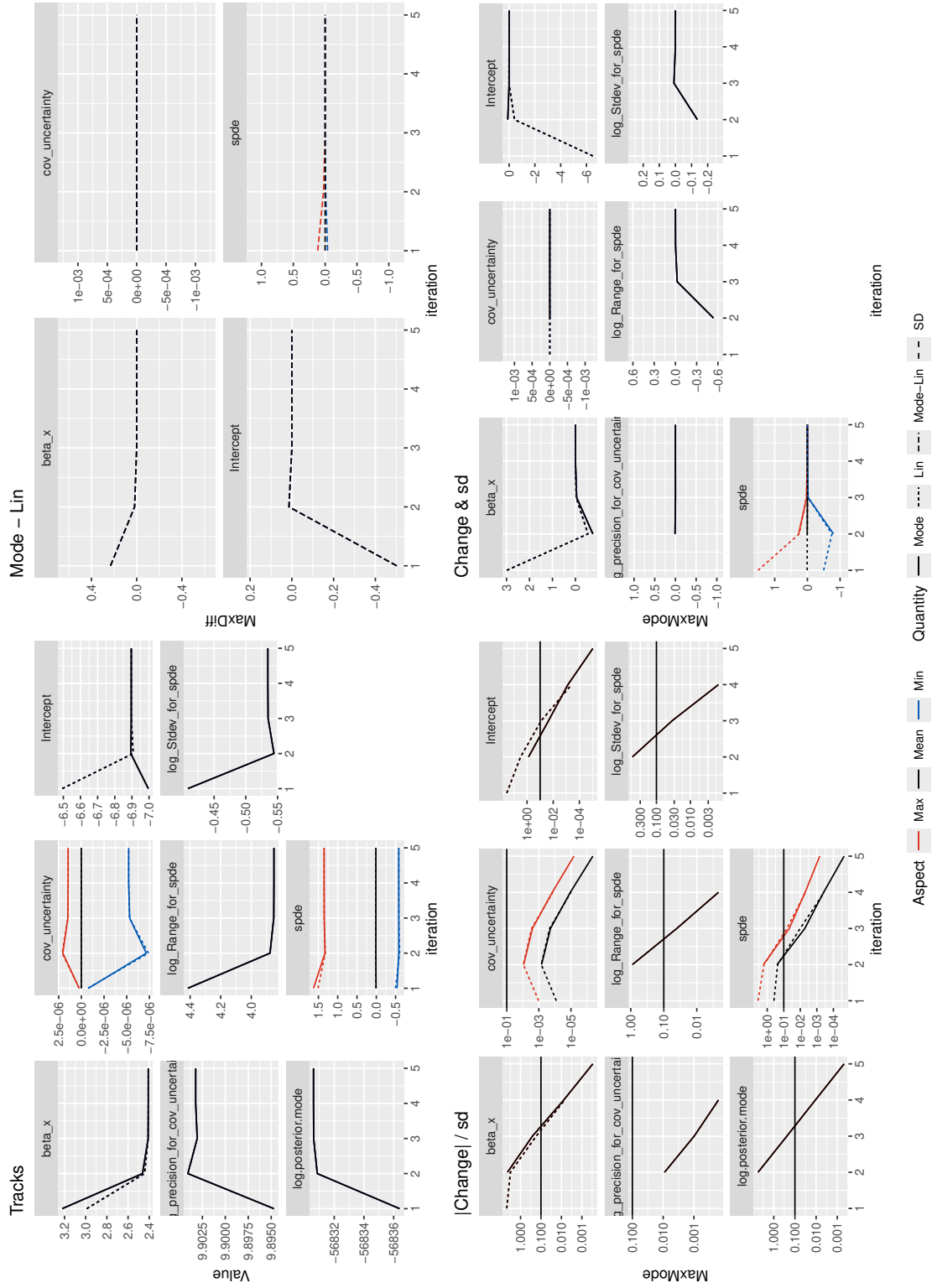


Change & sd



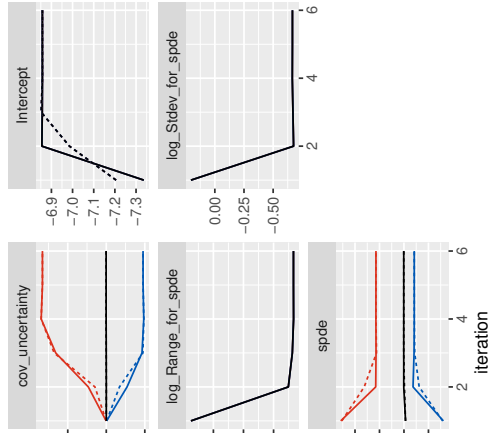
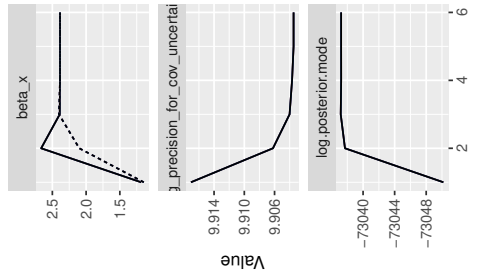
Aspect — Max — Mean — Min Quantity — Mode — Lin — Lin — Mode-Lin — SD

Convergence plots for fit_icov3_sd01

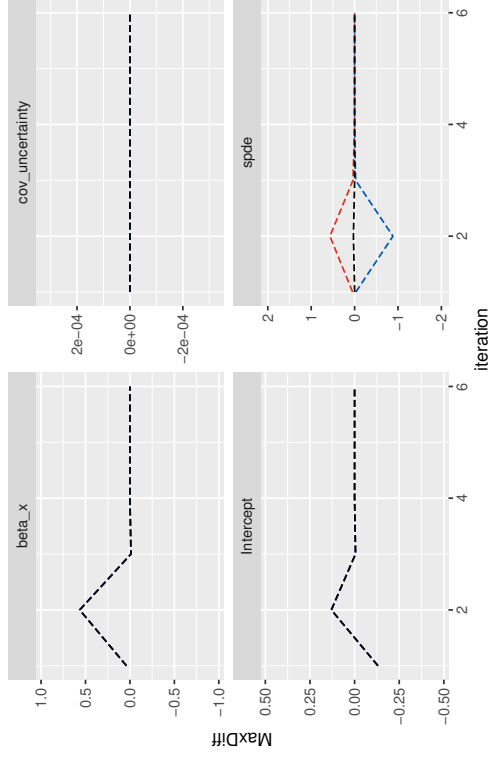


Convergence plots for fit_icovap

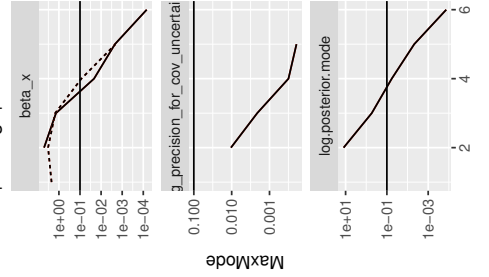
Tracks



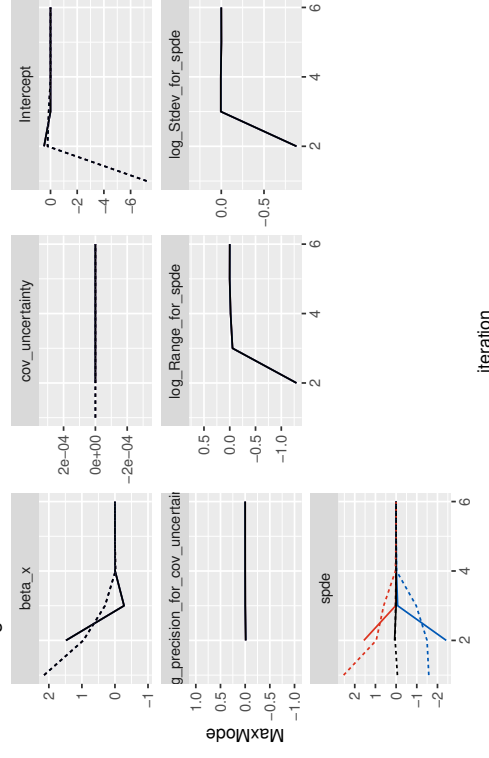
Mode - Lin



|Change| / sd



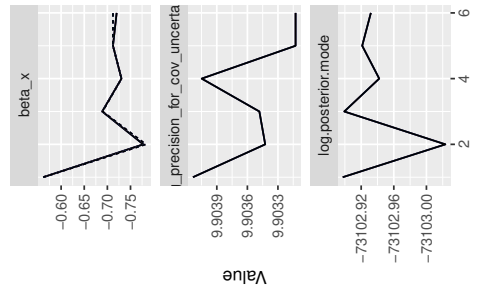
Change & sd



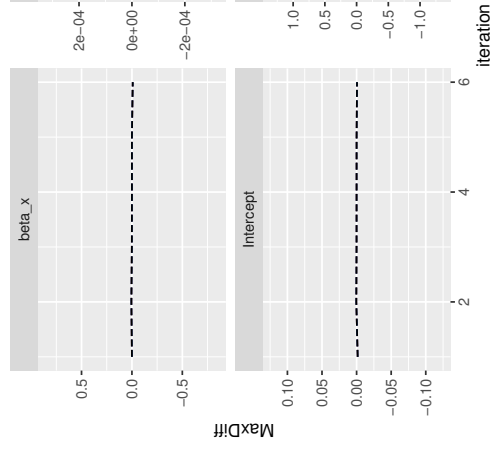
Aspect — Max — Mean — Min Quantity — Mode — Lin — — SD

Convergence plots for fit_icovap_n1

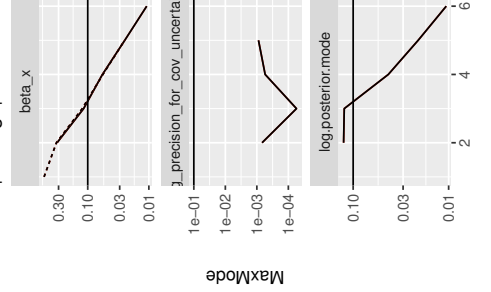
Tracks



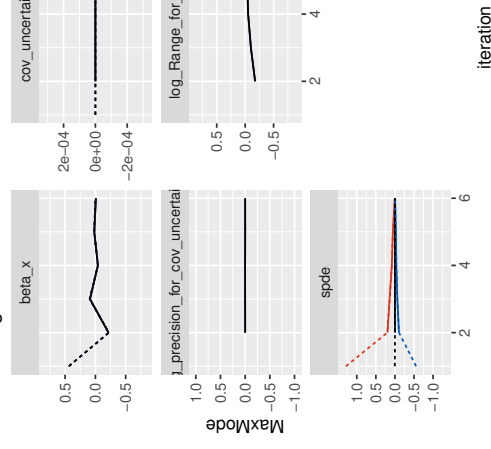
Mode - Lin



|Change| / sd



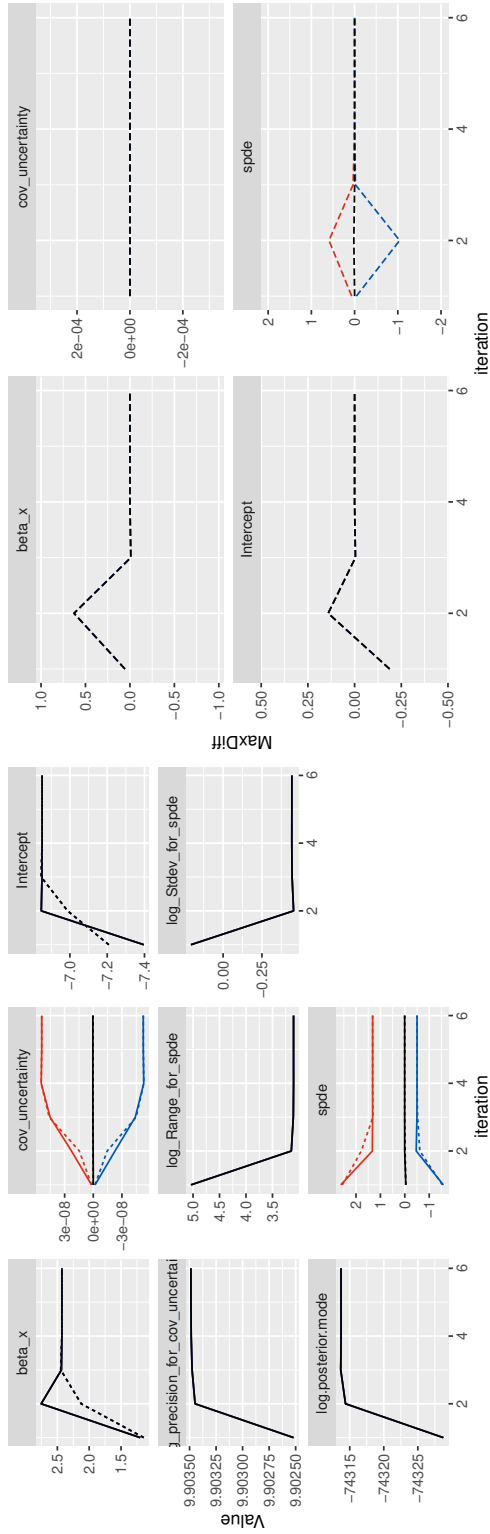
Change & sd



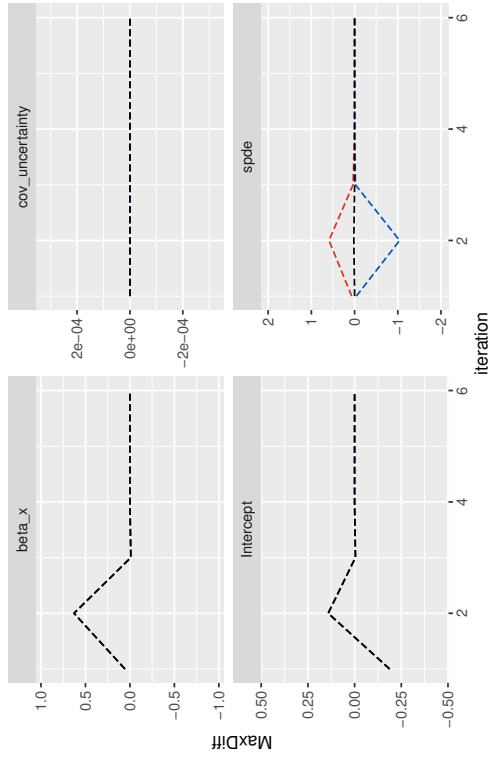
Aspect — Max — Mean — Min Quantity — Mode — Lin — Mode-Lin — SD

Convergence plots for fit_icovap_pts

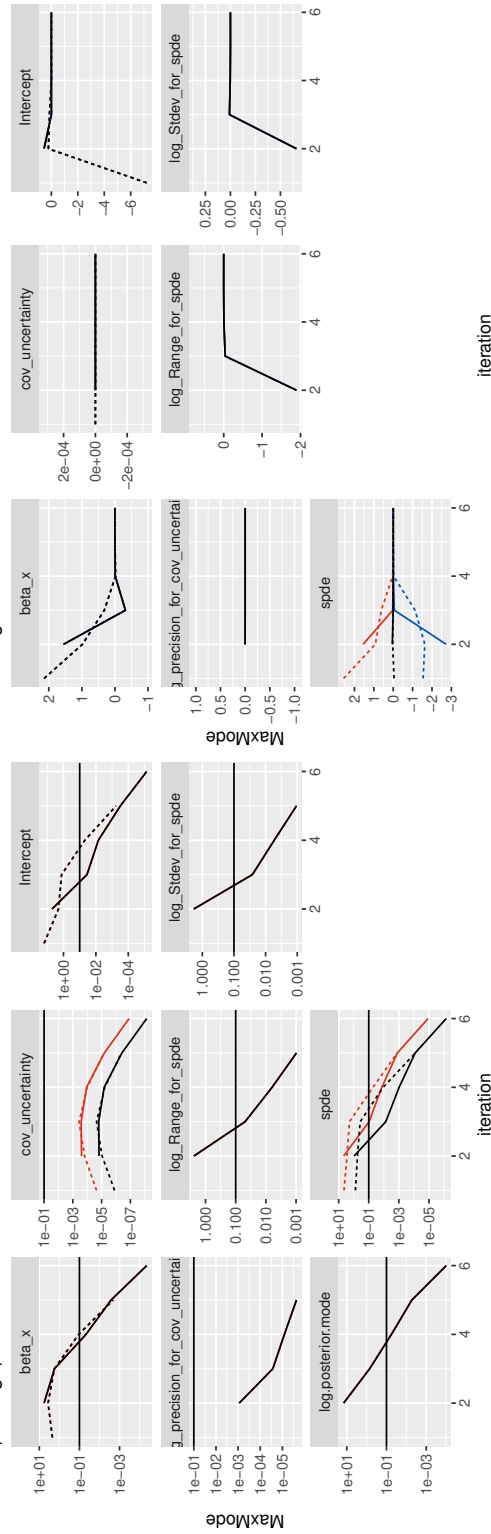
Tracks



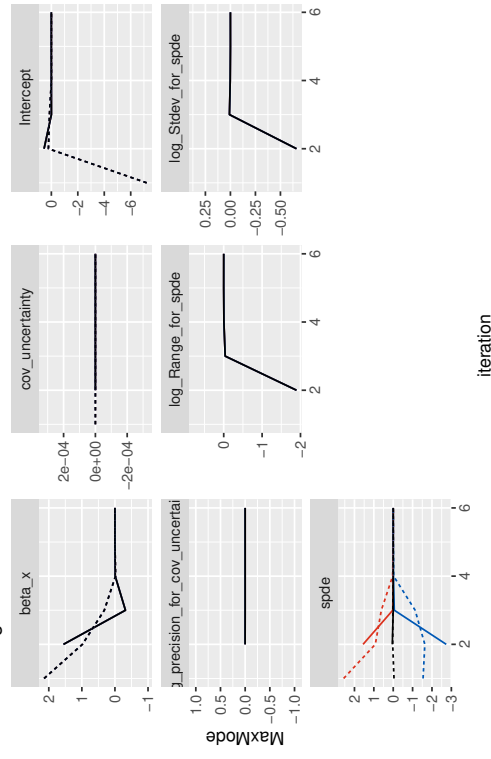
Mode - Lin



|Change| / sd

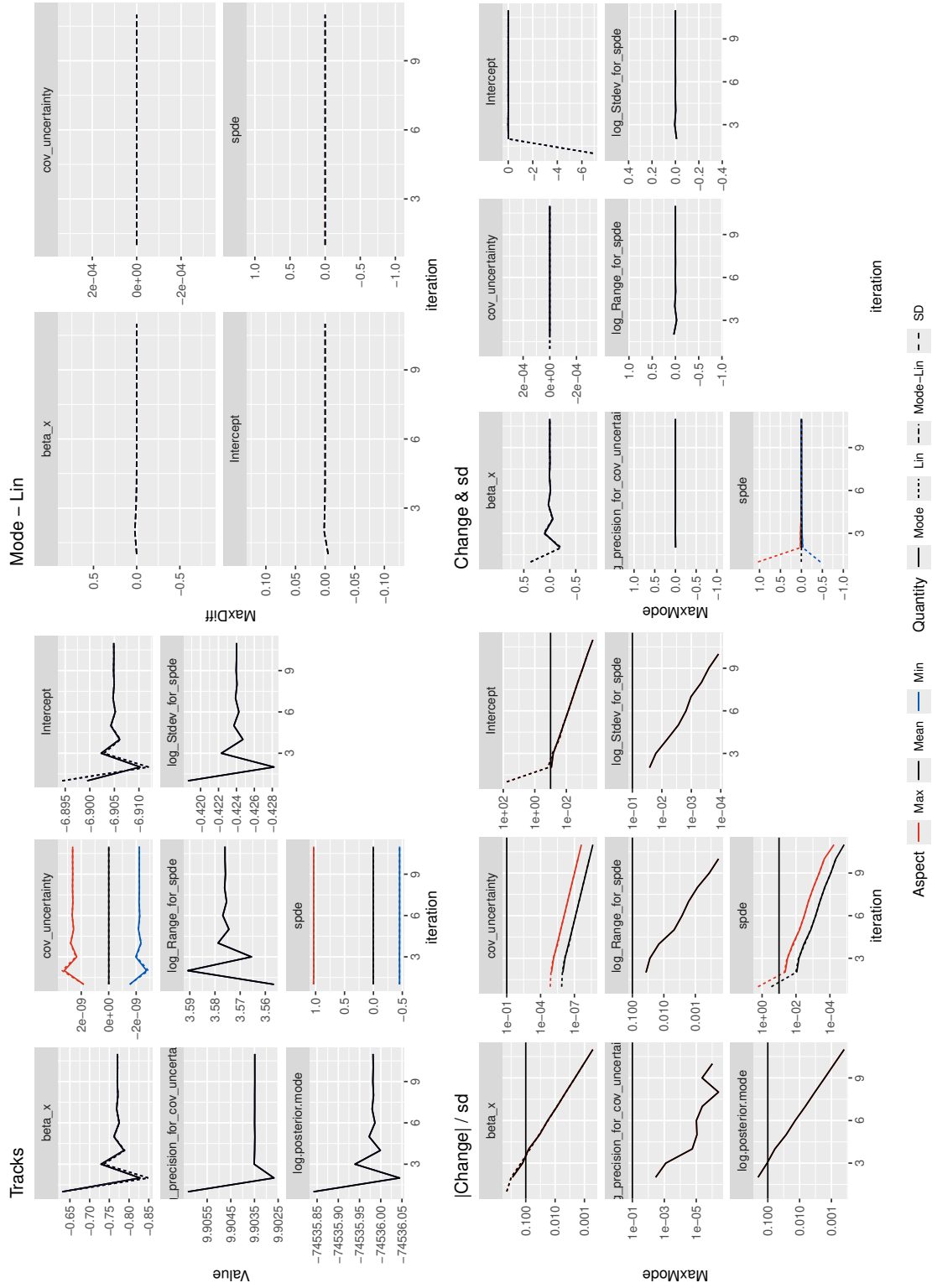


Change & sd



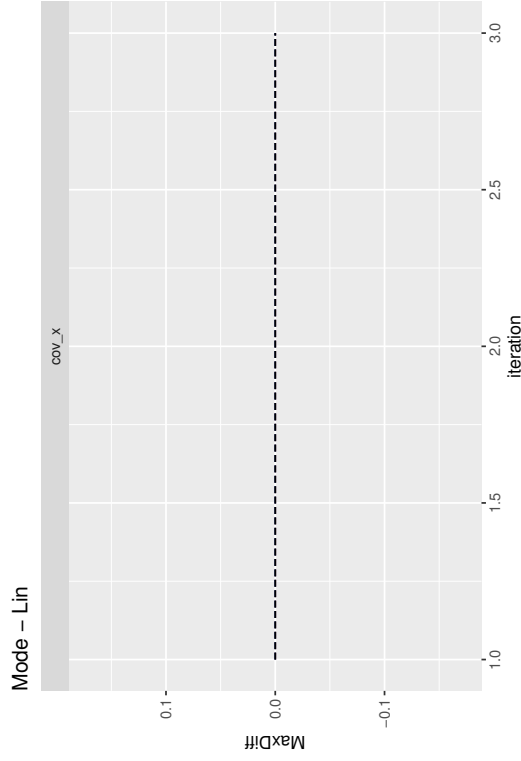
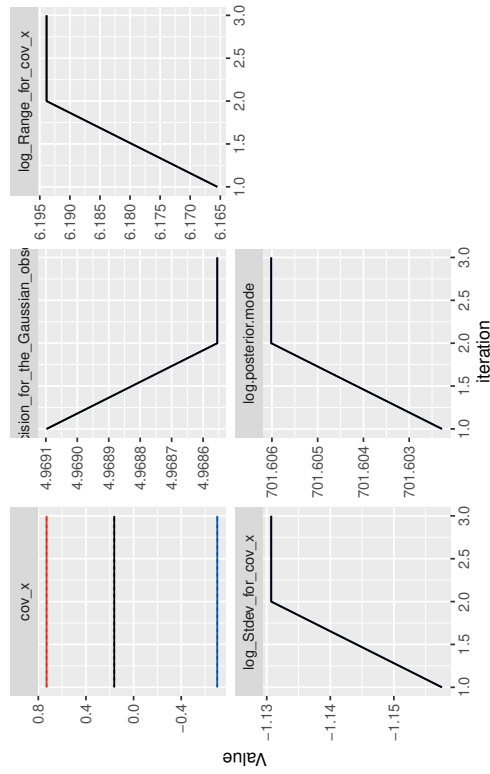
Aspect — Max — Mean — Min — Quantity — Mode — Lin — Mode-Lin — SD

Convergence plots for fit_icovap_pts_nl

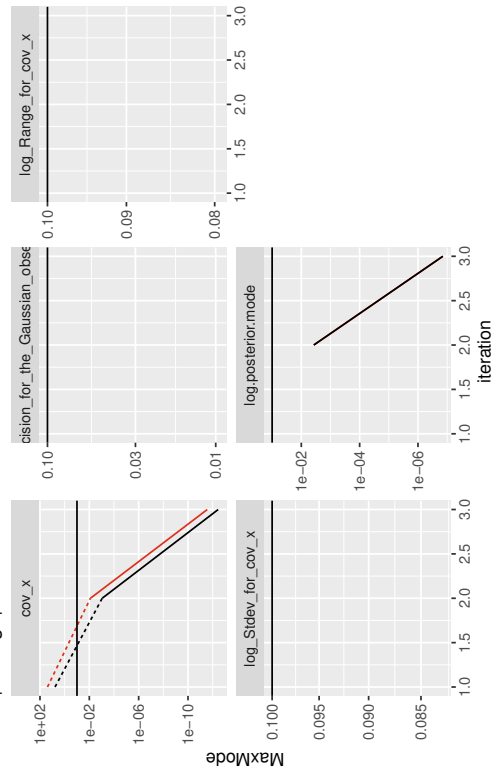


Convergence plots for fit_icov_sd01

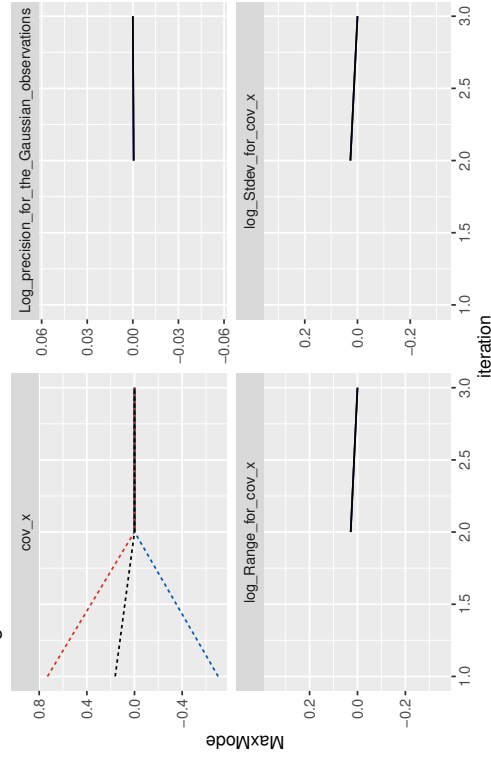
Tracks



|Change| / sd



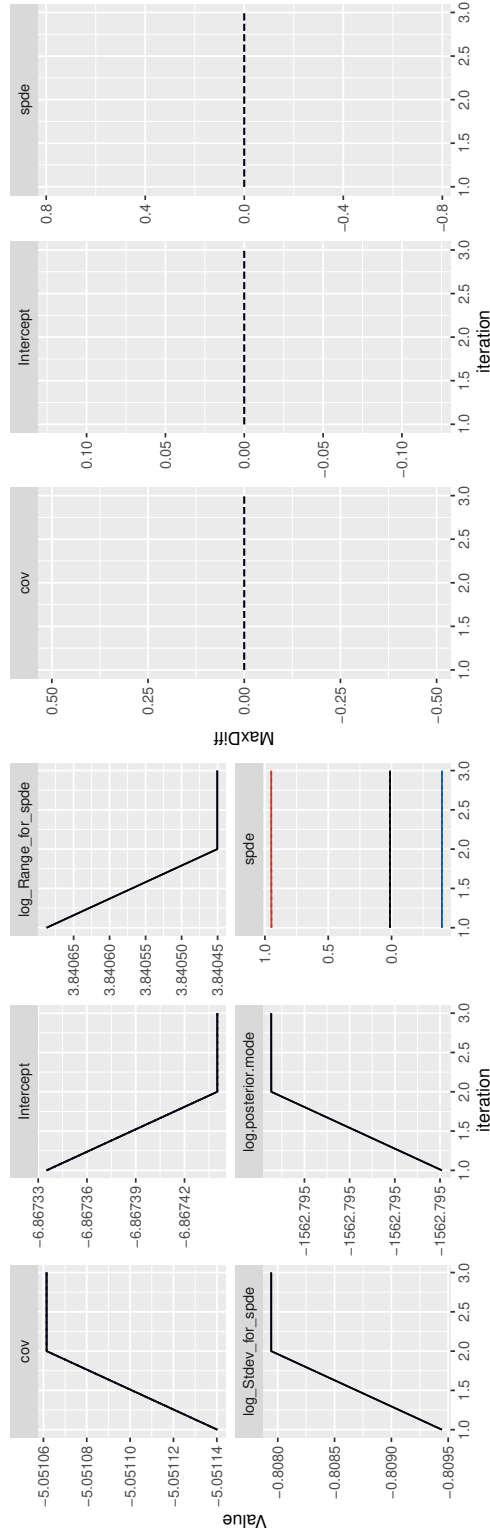
Change & sd



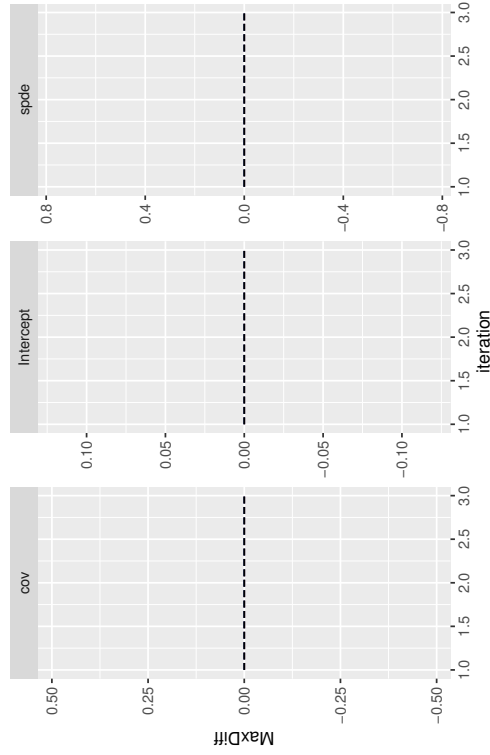
Aspect — Max — Mean — Min — Quantity — Mode — Lin — Mode-Lin — SD

Convergence plots for fit_pts

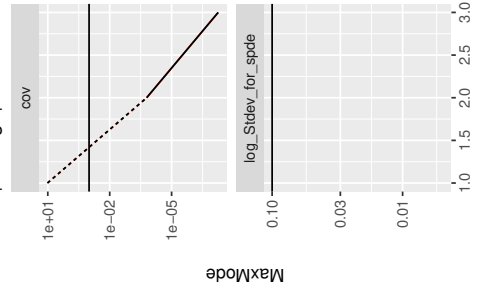
Tracks



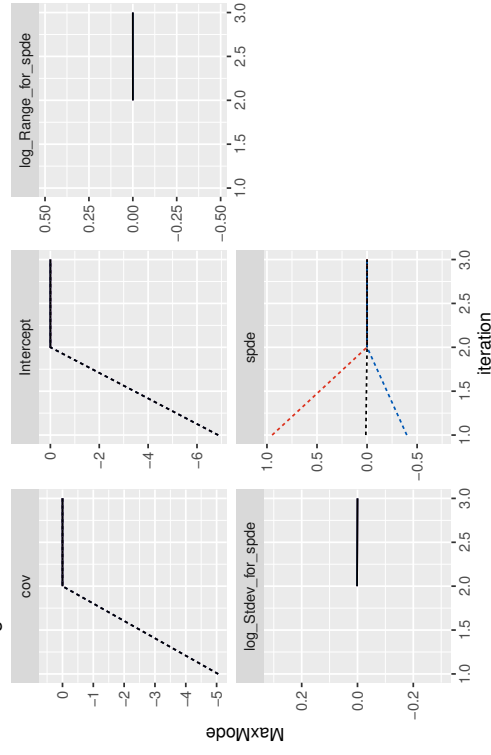
Mode - Lin



|Change| / sd



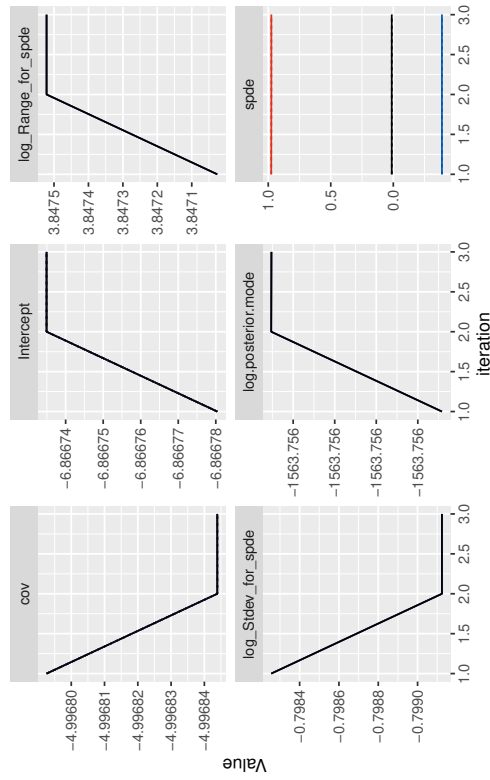
Change & sd



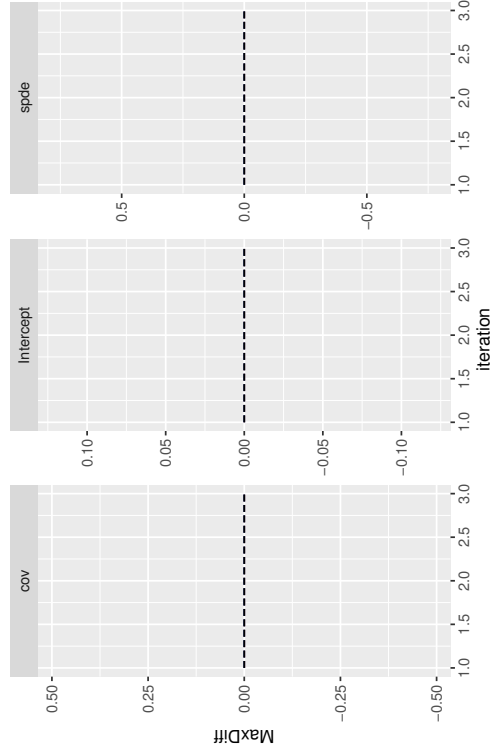
Aspect — Max — Mean — Min — Quantity — Mode --- Lin --- Mode-Lin --- SD

Convergence plots for fit_pts_agg

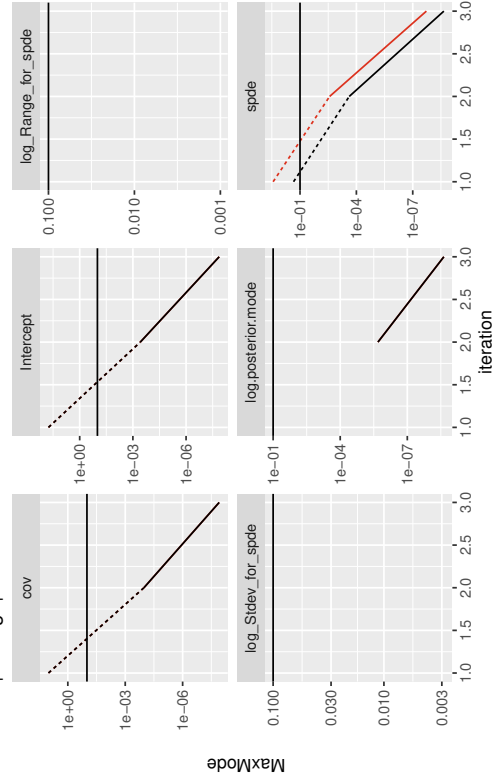
Tracks



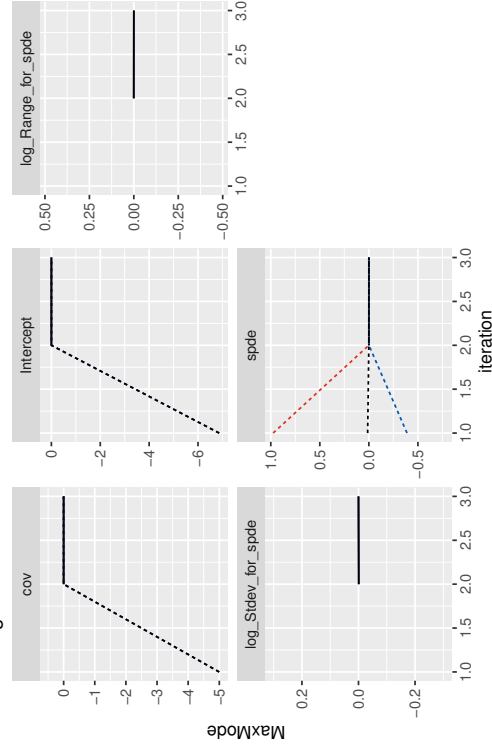
Mode - Lin



|Change| / sd



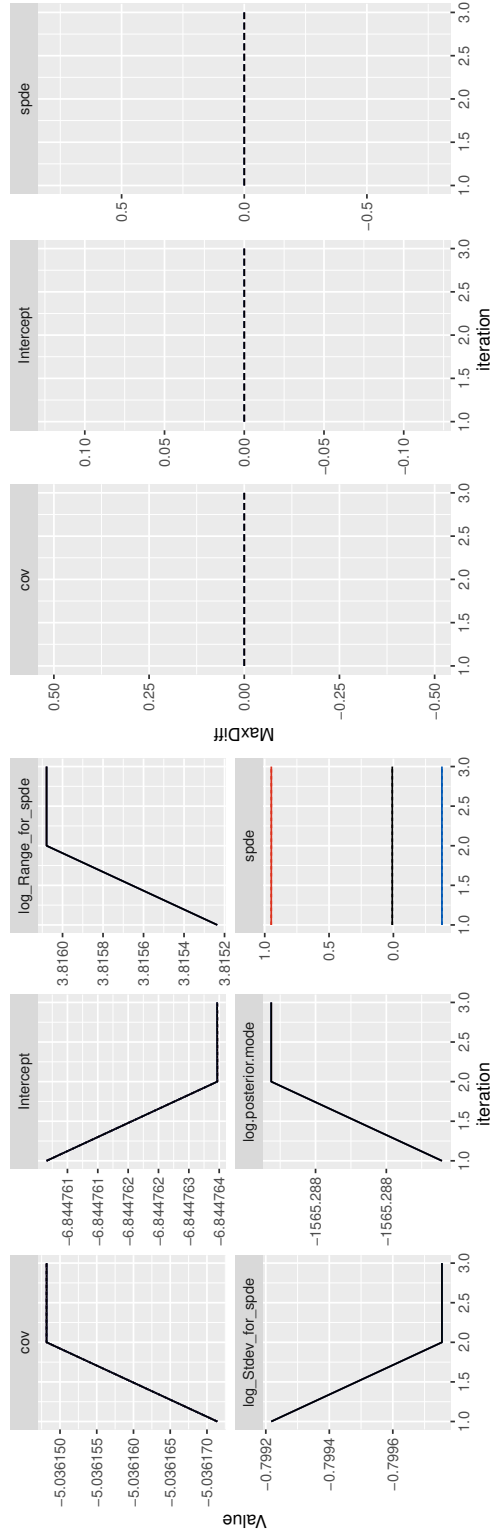
Change & sd



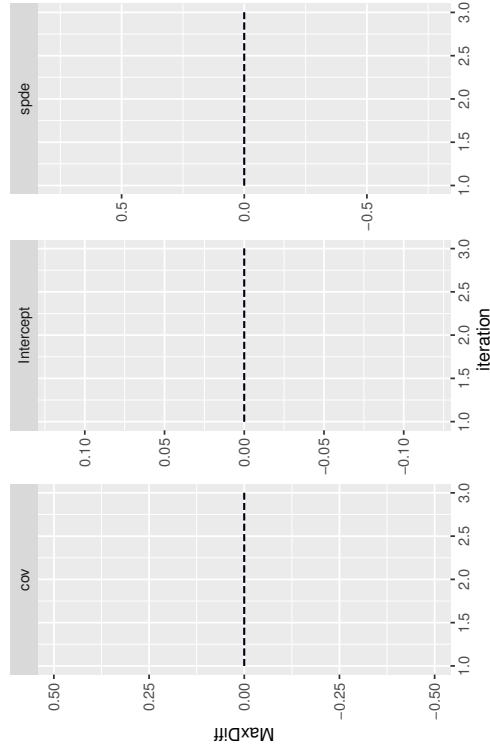
Aspect — Max — Mean — Min Quantity — Mode - - - Lin - - - - Mode-Lin - - - SD

Convergence plots for fit_pts_poly

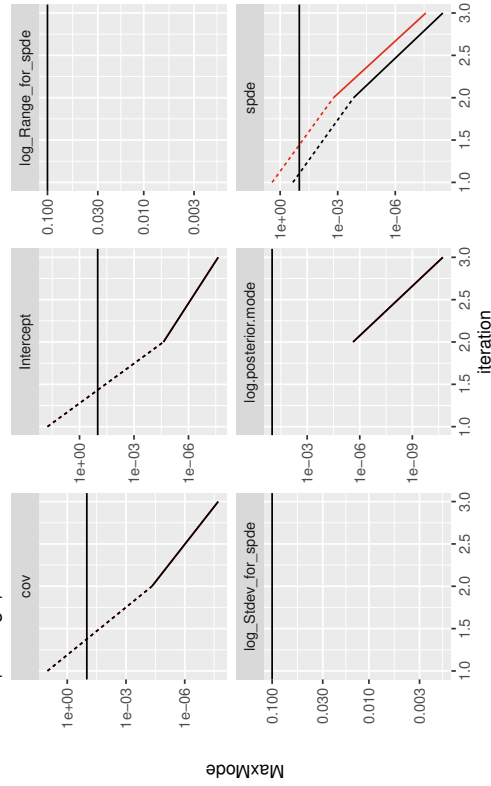
Tracks



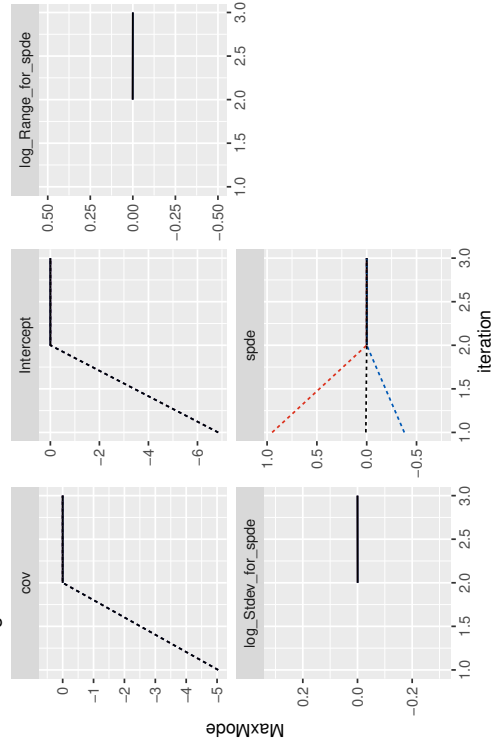
Mode - Lin



|Change| / sd



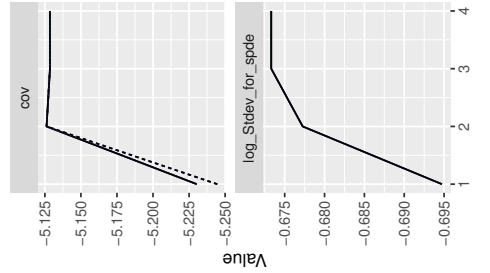
Change & sd



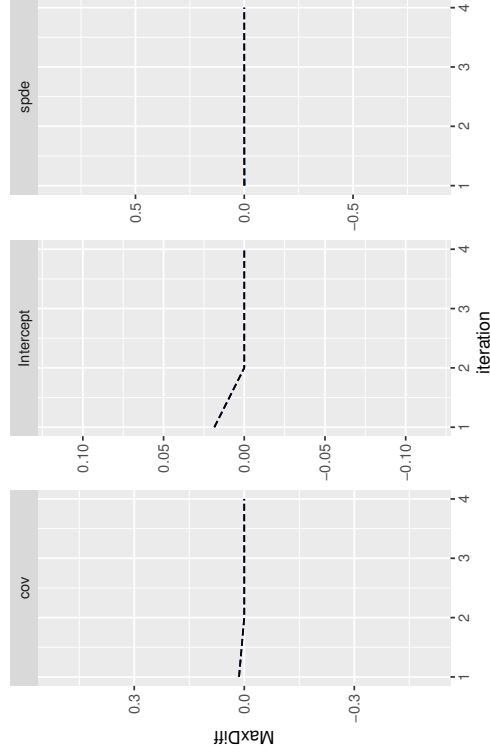
Aspect — Max — Mean — Min — Quantity — Mode — Lin — Mode-Lin — SD

Convergence plots for fitly

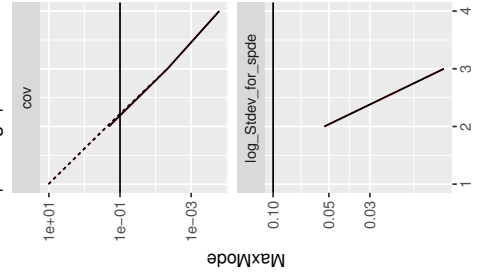
Tracks



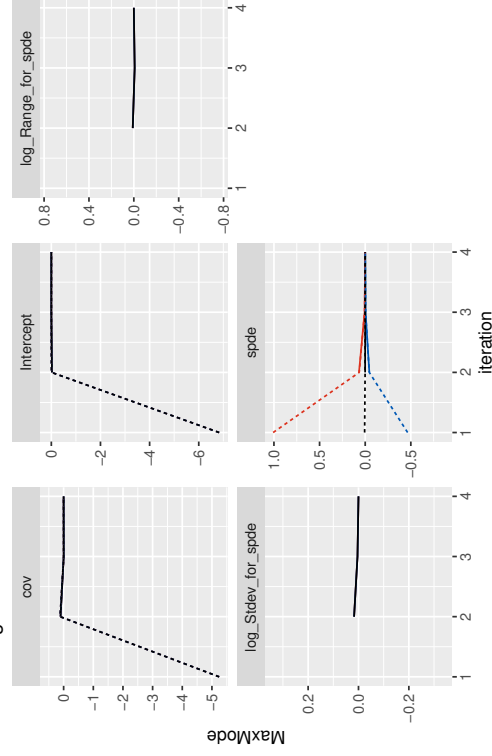
Mode - Lin



|Change| / sd



Change & sd



Aspect — Max — Mean — Min — Quantity — Mode — Lin — Mode-Lin — SD

E Reproducibility

The results were generated with INLA 25.01.23, inlabru 2.12.0.9005 and fmeshier 0.2.0. The shape file of Nepal's municipalities can be downloaded: <https://opendatanepal.com/dataset/nepal-municipalities-wise-geographic-data-shp-geojson-topojson-kml/resource/06b90abc-1380-46ed-b529-e455de6d794d>. The reproducible code for the simulation study can be found in the github repository: <https://github.com/enoch26/misalignedata>.